Dynamic response and stability of flexible hydrofoils in incompressible and viscous flow

by

Eun Jung Chae

A dissertation submitted in partial fulfillment
of the requirements for the degree of
Doctor of Philosophy
(Naval Architecture and Marine Engineering)
in the University of Michigan
2015

Doctoral Committee:

Associate Professor Yin Lu Young, Chair
Professor Luis P. Bernal
Professor Michael M. Bernitsas
Professor Carlos E. S. Cesnik
Assistant Professor Kevin J. Maki

ACKNOWLEDGEMENTS

I sincerely appreciate my advisor, Prof. Yin Lu Young, for her guidance, advice, encouragement, and support to finish a Ph.D. I would like to thank my committee members: Prof. Louis P. Bernal, Prof. Michael M. Bernitsas, Prof. Carlos E. S. Cesnik, and Prof. Kevin J. Maki for their support and helpful suggestions. Moreover, I would like to thank Dr. Deniz Tolga Akcabay and Dr. Antoine Ducoin for their tremendous help and support. Additional thanks to my collaborators at the French Naval Academy Research Institute (IRENav): Prof. Jacques André Astofi and Ms. Alexandra Lelong.

I gratefully acknowledge Dr. Ki-Han Kim and Ms. Kelly Cooper, program managers, and the Office of Naval Research (ONR), for their financial support through Grant Nos. N00104-13-1-0383 and N00014-11-1-0833, and also ONR Global and Dr. Woei-Min Lin (program manager) through Grant No. N62909-12-1-7076. This work was also supported in part by the National Research Foundation of Korea (NRF) grant funded by the Korean government (MEST) through the GCRC-SOP Grant no. 2012-0004783.

Finally, I really appreciate my family and friends, who give support and care and help me overcome difficult times and complete my Ph. D.

TABLE OF CONTENTS

LIST OF FIGURES

Figure

LIST OF TABLES

Table

LIST OF ABBREVIATIONS

2D Two-dimensional

2-DOF Two Degrees-of-freedom

AC Aerodynamic Center

CFD Computational Fluid Dynamics

CSD Computational Structural Dynamics

EA Elastic Axis

EOM Equation of Motion

FC Fully Coupled

FD Frequency Domain

FSI Fluid-structure Interaction

LE Leading-edge

LES Large Eddy Simulation

LEV Leading-edge Vortex

LHC Loose Hybrid Coupled

MAV Micro Air Vehicles

RHS Right Hand Side

RMS Root-mean-square

SST Shear Stress Transport

TD Time Domain

TE Trailing-edge

uRANS Unsteady Reynolds-averaged Navier-Stokes

Nomenclature

Dimensional Terms

c Chord length $[m]$

b Semi-chord length, $b = c/2$ $[m]$

s Span length $[m]$

τ Foil maximum thickness $[m]$

U Inflow velocity $[m/s]$

h Bending deformation, positive for upwards $[m]$

θ Twisting deformation, positive for counter-clockwise about the elastic axis (EA) $[^\circ]$

α_o Geometric angle of attack, positive for clockwise with respect to the incoming flow $[^\circ]$

α_{Lo} Angle of attack at which the lift force is zero, positive for clockwise about the elastic axis (EA) $[^\circ]$

α_{eff} Effective angle of attack, positive for clockwise about the elastic axis (EA), $\alpha_{\text{eff}} = \alpha_o - \theta$ $[^\circ]$

E_s Solid Young's modulus [Pa]

G_s Solid shear modulus [Pa]

ρ_s Solid density $[kg/m^3]$

ρ_f Fluid density $[kg/m^3]$

μ_{eff} Fluid effective dynamic viscosity $[kg/(m \cdot s)]$

ν_{eff} Fluid effective kinematic viscosity, $\nu_{\text{eff}} = \mu_{\text{eff}}/\rho_f$ $[m^2/s]$

ν_f Fluid kinematic viscosity $[m^2/s]$

q Dynamic pressure, $q = \rho_f U^2/2$ $[kg/m \cdot s^2]$

P Total pressure [Pa]

P_o Static pressure [Pa]

$\boldsymbol{\sigma}_f$ Total stress tensor for a Newtonian fluid [Pa]

$\mathbf{u}_f$ Local fluid velocity $[m/s]$

$\mathbf{r}$ Position vector from the EA to a point on the closed foil surface $[m]$

f_h The first in-vacuum natural bending frequency, $f_h = \omega_h/(2\pi)$ [Hz]

f_θ The first in-vacuum natural twisting frequency, $f_\theta = \omega_\theta/(2\pi)$ [Hz]

f_h^* The first in-water natural bending frequency, $f_h^* = \omega_h^*/(2\pi)$ [Hz]

f_θ^* The first in-water natural twisting frequency, $f_\theta^* = \omega_\theta^*/(2\pi)$ [Hz]

f Foil oscillation frequency, $f = \omega/(2\pi)$ [Hz]

f_{vs} Vortex shedding frequency [Hz]

T_h^* The first in-water natural bending period of flexible hydrofoil, $T_h^* = 1/f_h^*$ $[s]$

t Time $[s]$

Δt Time-step size $[s]$

m Solid mass per unit span $[kg/m]$

I_θ Solid mass moment of inertia per unit span $[kg \cdot m]$

S_θ Solid static imbalance per unit span $[kg]$

$C_{s,h}$ Solid bending damping values per unit span $[kg/s]$

$C_{s,\theta}$ Solid twisting damping values per unit span $[kg \cdot m/s]$

$K_{s,h}$ Solid bending stiffness values per unit span $[N/m]$

$K_{s,\theta}$ Solid twisting stiffness values per unit span $[N \cdot m/m]$

$\mathbf{u}_f$ Local fluid velocity $[m/s]$

$\widetilde{\mathbf{X}}$ Displacement vector, $[h/b,\, \theta]^T$

$\dot{\widetilde{\mathbf{X}}}$ Velocity vector, $[\dot{h}/b,\, \dot{\theta}]^T$

$\ddot{\widetilde{\mathbf{X}}}$ Acceleration vector, $[\ddot{h}/b,\, \ddot{\theta}]^T$

$\widetilde{\mathbf{M}}_s$ Solid inertial matrix

$\widetilde{\mathbf{C}}_s$ Solid damping matrix

$\widetilde{\mathbf{K}}_s$ Solid stiffness matrix

$\widetilde{\mathbf{M}}^T$ Inviscid fluid inertial matrix

$\widetilde{\mathbf{C}}^T$ Inviscid fluid damping matrix

$\widetilde{\mathbf{K}}^T$ Inviscid fluid stiffness matrix

Non-dimensional Terms

a Non-dimensional distance from mid-chord to elastic axis, positive for elastic axis after mid-chord [-]

e Non-dimensional distance from elastic axis to aerodynamic center (AC), positive for AC upstream of elastic axis ($e = a + 0.5$) [-]

d Non-dimensional distance from elastic axis to three quarter-chord ($3c/4$) ($d = a - 0.5$) [-]

x_θ Non-dimensional distance from elastic axis to center of gravity, positive for center of gravity aft of elastic axis, $x_\theta = S_\theta/(mb)$ [-]

r_θ Non-dimensional radius of gyration about the elastic axis, $r_\theta = \sqrt{I_\theta/(mb^2)}$ [-]

$\sqrt{\mu}$ Relative mass ratio: the ratio between solid inertial force and fluid inertial force for bending motion, $\sqrt{\mu} = \sqrt{m/(\pi\rho_f b^2)}$ [-]

$\overline{U}$ Reduced velocity: the ratio between fluid convection frequency and solid first in-vacuum natural twisting frequency, $\overline{U} = U/(\omega_\theta b)$ [-]

k Reduced frequency: the ratio between solid oscillation frequency and fluid convection frequency, $k = \omega b/U$ [-]

Ω Solid bending to twisting frequency ratio: the ratio between first in-vacuum natural bending and twisting frequencies, $\Omega = f_h/f_\theta$ [-]

Re Reynolds number: the ratio between fluid inertial force and fluid viscous force, $Re = Uc/\nu_f$ [-]

Re_{eff} Reynolds number: the ratio between fluid inertial force and fluid effective viscous force, $Re_{\text{eff}} = Uc/\nu_{\text{eff}}$ [-]

R_F Relative flexibility ratio: the ratio between fluid disturbing force and solid restoring force, $R_F = \overline{U}^2/(\mu r_\theta^2)$ [-]

St Strouhal number: the ratio between fluid convection frequency and solid oscillation frequency, $St = fc/U = k/\pi$ [-]

Eu Euler number: the ratio between static fluid pressure and fluid dynamic pressure, $Eu = 2P_o/(\rho_f U^2)$ [-]

AR Aspect ratio for rectangular foil, $AR = s/c$ [-]

$\overline{P}$ Non-dimensional total pressure, $\overline{P} = P/P_o$ [-]

ν_s Solid Poisson ratio [-]

$\overline{\boldsymbol{\sigma}}$ Non-dimensional total stress tensor [-]

$\overline{\mathbf{u}}_s$ Non-dimensional local solid velocity, $\overline{\mathbf{u}}_s = \mathbf{u}_s/(\omega_\theta b)$ [-]

$\overline{\mathbf{u}}_f$ Non-dimensional local fluid velocity, $\overline{\mathbf{u}}_f = \mathbf{u}_f/(\omega_\theta b)$ [-]

$\mathbf{n}$ Unit normal vector on the foil surface, positive pointing out of the foil surface [-]

$\mathbf{t}$ Unit tangential vector on the foil surface, positive for downstream [-]

$\bar{t}$ Non-dimensional time, $\bar{t} = t\omega_\theta$ [-]

$\overline{\omega}$ Non-dimensional frequency, $\overline{\omega} = \omega/\omega_\theta = f/f_\theta$ [-]

ϖ Non-dimensional vorticity, $\varpi = \omega b/U$ [-]

$C(k)$ Theodorsen's circulation function [-]

ζ_T Total damping coefficient [-]

η_T Total loss factor, two times the total damping coefficient, $\eta_T = 2\zeta_T$ [-]

η_s Solid loss factor, $\eta_s = 2\zeta_s$ [-]

η_f Fluid loss factor, $\eta_f = 2\zeta_f$ [-]

C_L Lift coefficient, positive for upwards [-]

C_D Drag coefficient, positive for downstream [-]

C_M Moment coefficient, positive for counter-clockwise about the elastic axis (EA) [-]

C_{L_α} The slope of the lift coefficient, positive for upwards, $C_{L_\alpha} = dC_L/d\alpha_{\text{eff}}$ [-]

$C_{Mo,AC}$ Moment coefficient about the aerodynamic center, positive for counter-clockwise about the elastic axis (EA) [-]

L_{FSI} Inviscid fluid lift force per unit span, positive for upwards

M_{FSI} Inviscid fluid moment force per unit span, positive for counter-clockwise about the elastic axis (EA)

L_{CFD} Viscous fluid lift force per unit span computed from CFD, positive for upwards

M_{CFD} Viscous fluid Moment force per unit span computed from CFD, positive for counter-clockwise about the elastic axis (EA)

ABSTRACT

Dynamic response and stability of flexible hydrofoils in incompressible and viscous flow

by

Eun Jung Chae

Chair: Yin Lu Young

It is important to understand and accurately predict the static and dynamic response and the stability boundary of flexible hydrofoils to ensure their structural safety, facilitate the design and optimization of new and existing concepts, and test the feasibility of using advanced materials and control concepts. In particular, with recent advancements in material and computational modeling and design, it is possible to take advantage of advanced materials and the fluid-structure interaction (FSI) response to improve the hydrodynamic and structural dynamic performance of flexible hydrofoils. As interest in maritime applications of lightweight, flexible hydrofoils increases, understanding the flow-induced vibration response and stability becomes more important to ensure structural safety and to optimize performance and control. Hence, the objectives of this dissertation are the following: 1) to derive and validate the FSI response and stability boundary of flexible hydrofoils in incompressible and viscous flow; 2) to investigate the influence of inflow velocity, angle of attack, and relative mass ratio on the flow-induced vibrations of flexible hydrofoils; and 3) to investigate the influence of the flow-induced bend-twist coupling of flexible hydrofoils.

A loose hybrid coupled (LHC) method is presented to predict the dynamic FSI response and stability of flexible hydrofoils in incompressible and viscous flow. The results indicate that both the flutter and divergence speeds decrease when the relative mass ratio (i.e, solid-to-fluid added mass ratio, $\sqrt{\mu}$) decreases, and that linear potential theory over-predicts the flutter speed at the low mass ratio regime ($\sqrt{\mu} < 3$). It should be noted that although the static divergence is insensitive to variations in solid mass, the divergence speed decreases with decreasing $\sqrt{\mu}$ because of increases in the fluid density, which increases the fluid disturbing force. The results indicate that static divergence governs for $\sqrt{\mu} < 1$, dynamic divergence governs for $1 \leq \sqrt{\mu} < 2$, and flutter governs for $\sqrt{\mu} \geq 2$. The in-water natural frequencies of flexible hydrofoils are much lower than in-air natural frequencies because of added mass effects. The in-water natural frequencies vary with inflow velocity, angle of attack, and relative mass ratio due to flow-induced bend-twist coupling and viscous effects on the system's stiffness and damping terms. The results also show that vortex shedding frequencies of flexible hydrofoils can be much lower than those of rigid hydrofoils, and that the wake patterns can differ greatly between rigid and flexible hydrofoils. In particular, when the vortex shedding frequencies snap into one of the natural frequencies of the flexible hydrofoil (i.e, a lock-in condition of flexible hydrofoils), the vibration and load fluctuation amplitudes are amplified. The results further show that the inviscid simulations tend to overestimate the total loss factors for cases with low mass ratios ($\sqrt{\mu} < 1$), because of viscous and flow-induced bend-twist coupling effects. Overestimation of total loss factors increases with higher inflow velocity and lower relative mass ratio, and can be dangerous, potentially leading to earlier onset of fatigue, louder noise and vibrations.

CHAPTER I

Introduction

1.1 Motivation

In the majority of research involving dynamic fluid-structure interaction (FSI) modeling, the focus has been on aerospace or wind energy structures, where the effects of fluid inertia and fluid damping are relatively small. In marine structures, however, the influence of fluid inertia and fluid damping can be much greater than that of solid inertia and material damping. Furthermore, the hydrodynamic loads can be complicated due to viscous effects, hydrodynamic cavitation, and free surface effects because they can significantly modify and interact with the dynamic response of marine structures.

Through recent advances in material and innovative passive and active control technologies, it is possible to take advantage of the FSI response of lightweight, flexible hydrofoils to improve hydrodynamic and structural performance. Designing lightweight, flexible hydrofoils for marine environments is rather complicated. This is because these bodies often operate in heavily loaded and off-design conditions, which may lead to accelerated fatigue, vibration, noise, and even hydroelastic instability such as divergence, flutter, resonance, and lock-in. To illustrate, comparison of the relative mass ratio (i.e., solid-to-fluid added mass ratio), $\mu = m/(\pi\rho_f b^2)$, and the relative flexibility ratio (the ratio between fluid disturbing force and solid restoring

force, which is also the square of the ratio of the inflow velocity to the divergence velocity), $R_F{=}K_{f,\theta}/K_{s,\theta}{=}(U/U_d)^2{=}\overline{U}^2/(\mu r_\theta^2)$, for airfoils and hydrofoils with the same geometry are shown in Fig. 1.1 for a wide range of common materials. m is the solid mass per unit span, ρ_f is the fluid density, b is the semi-chord, and r_θ is the radius of gyration. U and U_d are the inflow velocity and static divergence velocity, respectively. $\overline{U} = U/(\omega_\theta b)$ is the reduced velocity. ω_θ is the first in-air natural twisting frequency.

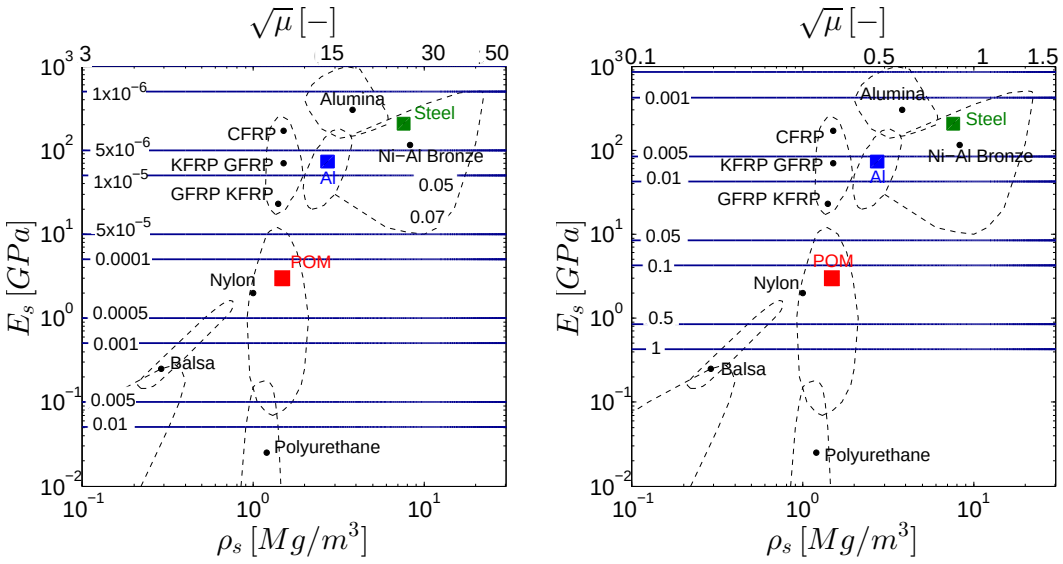

(a) Relative flexibility ratio of the airfoil (b) Relative flexibility ratio of the hydrofoil

Figure 1.1: Comparison of the relative mass ratio (μ), and relative flexibility ratio ($R_F = \overline{U}^2/(\mu r_\theta^2)$) for the rectangular cantilevered NACA0015 foils (a) in air and (b) in water with $c = 0.1\ m$, $s = 0.192\ m$, $\tau/c = 0.15$, $\nu_s = 0.35$, $r_\theta = 0.44$, and $U = 9\ m/s$. Notice that when $R_F \geq 1$, $U \geq U_d$, and the structure becomes unstable due to static divergence.

The airfoils and hydrofoils are assumed to be structurally homogeneous and materially isotropic, and they are assumed to be cantilevered at their root. These foils have a rectangular platform with NACA0015 cross-sections. The chord length is $c = 0.1$ m, the span length is $s = 0.192$ m, and the maximum thickness ratio is $\tau/c = 0.15$. For all the materials considered, the Poisson ratio is assumed to be fixed at $\nu_s = 0.35$, the radius of gyration fixed at $r_\theta = 0.44$, and the inflow velocity assumed to be $U = 9$

m/s. Notice that when $R_F \geq 1$, $U \geq U_d$, the structure becomes unstable due to static divergence. For the airfoil example shown in Fig. 1.1(a), all relevant materials yield relatively high mass ratios of $3 < \sqrt{\mu} < 30$. However, for the hydrofoil example shown in Fig. 1.1(b), all relevant materials in water yield much lower mass ratios of $\sqrt{\mu} < 1$. The results in Fig. 1.1 show that as the Young's modulus (E_s) increases, ω_θ increases: Thus, $\overline{U}$ decreases as E_s increases for a given operating field inflow velocity (i.e., $E_s \propto \omega_\theta^2 \propto 1/\overline{U}^2$). Notice that for a fixed $\overline{U}$, which would be the same for both the airfoil and hydrofoil if the geometry and material are identical, the hydrofoil is relatively more flexible than the airfoil, as indicated by the higher $R_F = \overline{U}^2/(\mu r_\theta^2)$ values (greater fluid disturbing force) due to the low μ for hydrofoil. Consequently, the hydrofoil is more susceptible to static divergence because of greater fluid disturbing force. In fact, for the hydrofoil shown in Fig. 1.1(b), static divergence will occur for cases with $E_s \leq 0.2$ GPa as $R_F = \overline{U}^2/(\mu r_\theta^2) \geq 1$. Hence, balsa wood and polyurethane would not be recommended for the hydrofoil if $U = 9$ m/s as they are too close to or exceed the static divergence boundary. The large differences in μ and R_F values between airfoils and hydrofoils and lead to very different physical and numerical stability characteristics, as will be illustrated later in this thesis.

1.2 Literature review

As mentioned above, fluid loads are significant for lightweight, flexible hydrofoils in dense fluids such as water. In addition, viscous effects associated with flow separations and vorticity influence the FSI responses as well as the hydroelastic stability boundaries. In this section, we will review previous work on the FSI responses and stability boundaries of lightweight, flexible hydrofoils with a focus on the in-water response.

1.2.1 Wake effects

The linear potential theory, based on *Theodorsen* (1935), *Sears* (1941), and *Garrick* (1946), provides the analytical expressions for the aerodynamic lift and moment of two-dimensional thin airfoils in uniform inflow with small amplitude, harmonic pitching and plunging oscillations. Particularly, *Theodorsen*'s approach assumed that: 1) the total lift force acts at the aerodynamic center (AC), a quarter-chord downstream from the thin foil's leading-edge (LE); and 2) the wake behind the foil consists of shed vortices from the foil's trailing-edge (TE). The shed vortices follow the foil oscillation frequency, and convect downstream in a direction parallel to the flow without any dissipation. However, *Anderson et al.* (1998) and *Munch et al.* (2010) showed that actual wake patterns are typically more complex than the idealized wake patterns assumed in *Theodorsen* (1935)'s model. We know that the actual wake patterns usually depend on the Strouhal number ($St = fc/U$) (or reduced frequency, $k = \omega b/U$), the Reynolds number ($Re = Uc/\nu$), and the effective angle of attack (α_{eff}). *Anderson et al.* (1998) experimentally studied the wake patterns of a two-dimensional (2D) pitching and plunging NACA0012 foil in a water tank for different St, where Re varied from 1.1×10^3 to 4.0×10^4 and α_{eff} varied from 7^o to 50^o. For $St < 0.2$ (i.e, $k < 0.6$), they observed a wavy wake without distinct vortices and with a very weak leading-edge vortex (LEV). Characteristically, this LEV appears between $0.1 < St < 0.2$ (i.e, $0.3 < k < 0.6$). *Anderson et al.* (1998) found that for $St > 0.2$ ($k > 0.6$), the wake consisted of a von Kármán vortex street with a LEV. In another study, *Munch et al.* (2010) conducted numerical and experimental studies of a NACA0009 hydrofoil pitching at various reduced frequencies (k). They varied k from 0.02 to 100 for numerical simulations, from 0.04 to 1.25 for experimental measurements, and Re from 0.5×10^6 to 1.5×10^6 with a 5° maximum angle of attack. For $k \leq 4$ (or $St \leq 1.27$), the wake pattern consisted of two undulating shear layers with opposite strengths. However, for $k \geq 12$ (or $St \geq 3.82$), the wake was observed

to be composed of distinct point vortices.

1.2.2 Viscous effects

Previous researchers have noted that linear potential flow theory (*Theodorsen*, 1935; *Sears*, 1941; *Garrick*, 1946) is inadequate for modeling FSI problems with strong viscous effects. Viscous forces have a greater influence on lightweight flexible hydrofoils in dense fluids such as water/blood/polymer solutions than on light fluids such as air. *Ducoin and Young* (2013) calculated the static divergence speed of a spanwise flexible cantilevered hydrofoil while considering viscous effects, and they showed that viscous effects helped to delay divergence. Furthermore, *Poirel et al.* (2008), *Poirel and Yuan* (2010), and *Ducoin and Young* (2013) have shown that pressure fluctuations, generated by the bursting of laminar separation bubbles and/or unsteady vortex shedding, can lead to hydrofoil vibrations, which can cause unwanted noise and vibration issues as well as potential catastrophic failure of the structure if flutter develops. Apart from studying foil geometries, *Connell and Yue* (2007) and *Akcabay and Young* (2012) also examined the dynamic response and stability of cantilever beams in viscous and axial flows. *Akcabay and Young* (2012) found that viscous effects affect the beams' tension, as well as delay flutter, reduce the vibration amplitudes, and modify the oscillation modes. *Akcabay and Young* (2012) also found that viscous effects are more significant for light beams in heavy fluids due to the increased relative contribution of the fluid forces.

1.2.3 Flow-induced vibration

Previous studies on flow-induced vibration of lightweight, flexible foils have focused mostly on aerospace or wind engineering structures, where the fluid density is much smaller than the effective solid density. The solid-to-fluid density ratio is typically between $1 - 10$ for marine structures; depending on the direction of motion,

the fluid inertial forces can be comparable to or even higher than the solid inertial forces for lightweight structures operating in a dense fluid such as water. In addition, the fluid damping and disturbing forces also depend on the relative velocity (*Theodorsen*, 1935; *Sears*, 1941), which suggests that the resulting in-water resonance frequencies will depend on the flow speed. However, these dependencies have been rarely considered by existing marine designs. While the relationship between velocity and structural oscillation frequency is intuitively apparent, it may also be expected to depend on the Reynolds number (Re) and the angle of attack. In their experimental studies, *Blake and Maga* (1975) and *Reese* (2010) showed that the resonance frequencies and total loss factors of flexible hydrofoils depend on the flow velocity. However, both of these former studies involved hydrofoils made of relatively heavy and stiff materials (i.e., stainless steel and aluminum) for a limited velocity range, and hence showed only a small dependence on the flow velocity.

As the fluid density increases, the relative contribution of viscous fluid-structure interaction (FSI) effects increases, particularly if flow separation and/or large deformations occur, and thus generate and modify the vorticity field. The vortex shedding frequency varies with the angle of attack, as shown by *Huang and Lin* (1995) and *Jung and Park* (2005) for low Reynolds number ($Re \leq 2.7 \times 10^4$) flows. The change of the vortex shedding frequency and wake pattern is even more obvious when compared to results at higher Reynolds number ($Re > 3 \times 10^5$) flows, as shown by *Reese* (2010) and *Ausoni* (2009). Nevertheless, very limited numerical and experimental studies are available for flexible hydrofoils in high Reynolds number flows. Since full-scale hydrofoils for maritime applications (propellers, turbines, rudders, control fins, etc) typically operate at $Re = 1 \times 10^5$ or higher, additional studies are needed to understand flow-induced vibrations, resonance frequencies, total loss factors at various velocities, and angles of attack for high Reynolds number flows.

1.2.4 Flow-induced bend-twist coupling

With recent advances in 3D printing technology and materials research, lightweight, flexible marine structures are becoming increasingly popular. Flexible marine structures may deliver superior performance in off-design operating conditions and in spatially and/or temporally varying flows (*Motley and Young*, 2011). If the location of the foil's center of pressure (CP) is away from the elastic axis (EA), the hydrodynamic load will induce a change in the angle of attack, and in turn affect the lift and bending deformations and hydrodynamic loads. The flow-induced bend-twist coupling exists even in the absence of geometric and material bend-twist coupling.

There are three approaches to the study of flow-induced bend-twist couplings: theoretical, experimental, and numerical. Most theoretical approaches assume inviscid, potential flow, which provides clear analytical expressions for the flow-induced bend-twist coupling. According to classical potential theory introduced by *Theodorsen* (1935), *Sears* (1941) and *Garrick* (1946), the flow-induced forces and moments are delineated to be a summation of three components: the fluid inertial, damping, and disturbing force terms, which are respectively in phase with acceleration, velocity, displacement. However, the theoretical approach does not consider viscous effects and it assumes small harmonic motion. Viscous effects may change the flow-induced bend-twist coupling response because of changes in pressure distribution on the foil surface due to flow separation, and nonlinear interactions with vortices in the wake and foil motion. Experimental (*Caporali and Brunelle*, 1964; *Blake and Maga*, 1975; *Reese*, 2010; *Chae et al.*, 2015a) and numerical (*Chae et al.*, 2015a) approaches determine the sum of all the FSI forces, and hence it is difficult to separate and delineate the values for each of the fluid inertial, damping, and stiffness coupling terms. These approaches show the full physics of flow-induced bend-twist coupling and viscous effects. For example, *Caporali and Brunelle* (1964) considered the flow-induced bend-twist coupling on flexible hydrofoils represented by the two-degrees of freedom (2-DOF)

model. They found that at the low mass ratio regime, accurate prediction of the off-diagonal terms (i.e., flow-induced bend-twist coupling terms) are required for the proper prediction of flutter. *Chae et al.* (2015a) examined the dynamic response of a flexible hydrofoil via combined numerical and experimental studies. They focused on the flow-induced vibrations of a lightweight, flexible hydrofoil, and showed that their viscous FSI predictions matched with experimental data obtained by the French Naval Academy Research Institute (IRENav). *Chae et al.* (2015a) found that the inviscid, linear theory equation provided in *Blake and Maga* (1975) tends to over-predict the total loss factor for cases with low mass ratio due to ignoring of the flow-induced bend-twist coupling terms. *Ausoni et al.* (2007), *Klamo* (2007), and *Schnipper et al.* (2009) also studied oscillating flexible hydrofoils in water. They observed that the vortex shedding frequencies may match with the natural frequencies of the oscillating flexible hydrofoils in water (i.e., lock-in), which lead to amplified vibrations and load fluctuations. However, their studies were limited to only either pitch or plunge oscillations, which failed to illustrate flow-induced bend-twist coupling effects. Since the flow-induced bend-twist coupling affects the dynamic response and stability of lightweight, flexible hydrofoils, it will be the focus of the study shown in chapter V of this thesis.

1.2.5 Physical instability modes

In this section, past works on the physical stability of flexible foils are reviewed. The common physical instability modes include divergence, flutter, resonance, lock-in, galloping, and buffeting. In this thesis, galloping and buffeting are excluded because they only occur in a limited range of very low or very high frequencies.

Specifically, galloping is a self-excited vibration driven by a time-averaged fluid force, and it develops in phase with the structure's motion. It leads to high amplitude vibrations because of a high energy content at a low frequency. Buffeting is caused

by unsteadiness in the flow around the structure, such as the airflow separation or shock wave oscillation, and is a high-frequency phenomenon, which could be occurred when the turbulence frequency approaches the structural natural frequency.

1.2.5.1 Divergence

There are two kinds of divergence: static divergence and dynamic divergence. Both are instability phenomena that will cause a system to fail due to excessive deformation and/or material failure. Static divergence is a linear static instability, where the deformations increase with time without oscillations. It is caused by the loss of the effective torsional stiffness, which occurs when the fluid disturbing moment exceeds the structural restoring moment. Dynamic divergence is similar to static divergence because the mean deformations also increase with time. However, dynamic divergence has an oscillation frequency, which decays with increasing deformation. Unlike static divergence, which depends only on the solid and fluid disturbing/restoring force terms, dynamic divergence also depends on the solid and fluid inertial and damping force terms, as shown by *Chae et al.* (2013). *Bendiksen* (1992, 2002) showed that dynamic divergence can lead to material failure, accelerated fatigue, vibration, noise issues, and even catastrophic structural failures. *Chae et al.* (2013) showed that dynamic divergence cannot be predicted with linear frequency domain methods because it is a nonlinear phenomenon where the oscillation frequency changes with time.

1.2.5.2 Flutter and lock-in

Flutter is a dynamic self-excited aeroelastic/hydroelastic instability, where the flow-induced deformations oscillate with a constant frequency. The critical flutter limit is defined as a point where the total damping is zero. Once this limit is exceeded, the oscillations will grow rapidly with time. For example, *Poirel et al.* (2008) and *Poirel and Yuan* (2010) showed that flutter can be caused by unsteady bursting

of laminar separation bubbles and/or unsteady vortex shedding. The flutter may also cause unwanted noise and vibration, which may likely lead to the catastrophic failure of a structure. *Leibowitz and Belz* (1962), *Cieslowski and Besch* (1970), *Song* (1972), *Brennen et al.* (1980), and *McCormick and Caracoglia* (2004) found that stall-induced flutter and cavitation-induced flutter may also cause large-scale vibrations and ultimately catastrophic structural failure. On the other hand, *Tang et al.* (2009) and *Akcabay and Young* (2012) indicated that flutter can be used to harvest energy from ambient flow.

In the past, hydrofoil flutter has rarely been studied because marine structures are typically made of heavy and stiff material; hence, flutter phenomenon was not a major issue. Further, the influence of fluid inertia and damping are difficult to quantify in water. Experimental studies of flutter in water pose a number of challenges such as higher fluid loads and lower maximum speeds due to limitations at water tunnels or towing tanks, as well as susceptibility to complications introduced by cavitations and free surface effects (e.g. *Woolston and Castile* (1951); *Abramson and Ransleben* (1965); *Cieslowski and Besch* (1970); *Besch and Liu* (1971)). However, today, some marine structures are made of lightweight and flexible materials to enhance their performances, where the relative fluid loads become more significant; therefore, the dynamic response and susceptibility to hydroelasticity of lightweight and flexible marine structures should be studied.

Specifically, a particular case of linear coupled-mode flutter is lock-in (*de Langre*, 2006). *de Langre* (2006) found that the coupled-mode flutter caused by coupling between displacement and wake may extend the range of lock-in. Lock-in is a non-linear phenomenon of vortex-induced vibrations that occurs when the vortex shedding frequency is close to the natural frequency of the system. Lock-in can bring about large vibration amplitudes and a sudden drop of the damping coefficient (*Blake et al.*, 1977; *Reese*, 2010; *Bernitsas et al.*, 2008). For example, *Ausoni et al.* (2007) showed

that vortex shedding frequencies are a function of the inflow velocity. They also showed that lock-in can be induced at certain inflow velocities. *Jung and Park* (2005) investigated the vortex shedding frequencies at different angles of attack. They found that lock-in did not occur at incidences of small angles of attack such as $\alpha_o < 4^\circ$, and at low Reynolds numbers ($Re = 2.7 \times 10^4$). However, lock-in did occur at incidences with large angles of attack, $\alpha_o > 10^o$, (*Reese*, 2010).

1.2.5.3 Resonance

Resonance is an externally-excited dynamic instability that occurs when the driving frequency is the same or nearly the same as the natural frequencies of the system. In physics, resonance accounts for abnormally large vibrations with large amplitudes. If resonance develops unexpectedly, the vibrations can prove catastrophic to structures with loud noise. Resonance could also accelerate fatigue and lead to detrimental failure (*Lian and Shyy*, 2007; *Visbal et al.*, 2009; *Olofsson*, 1966; *Young and Savander*, 2011). On the other hand, resonance can be also exploited to harvest energy (see *Bachynski et al.* (2012), for an example). Due to dependence on fluid loads, the resonance frequency in water is expected to be dependent on the submergence (*Lindholm et al.*, 1965), Reynolds Number (Re) (*Blake and Maga*, 1975; *Reese*, 2010), Strouhal Number (St) (*Blake and Maga*, 1975), relative velocity (*Reese*, 2010), and angle of attack.

1.3 Contributions

The objective of this dissertation is to improve the understanding and prediction capabilities of the fluid-structure interaction (FSI) response and the stability of flexible hydrofoils in incompressible and viscous flow. The contributions of this dissertation are summarized as follows:

1. New FSI coupling model development:

A cost efficient and stable FSI coupling model of the loose hybrid coupling (LHC) method was developed and validated for simulation of lightweight flexible bodies in incompressible and viscous flow, as shown in *Young et al.* (2012), *Chae et al.* (2013), and *Akcabay et al.* (2014). The LHC method subtracts the potential flow estimation of the FSI force from both the left hand side and right hand side of the equations of motion to accelerate the convergence and to avoid the numerical instability issues due to "virtual added mass" effect for lightweight bodies operating in dense, incompressible flow.

2. Stability boundary and governing instability mode determination:

   The governing instability mode and stability boundaries were determined for foils with a wide range of relative mass ratios. The governing instability mode was found to change from flutter for cases with high mass ratio ($\sqrt{\mu} \geq 2$), to dynamic divergence for cases with moderate mass ratio ($1 \leq \sqrt{\mu} < 2$), and to static divergence for case with low mass ratio ($\sqrt{\mu} < 1$). This was presented in *Chae et al.* (2013). The numerical simulations were validated with published experimental data in *Woolston and Castile* (1951) and *Besch and Liu* (1971).

3. Flow-induced vibrations examination:

   The influence of the inflow velocity, angle of attack, and relative mass ratio on flexible hydrofoils was investigated (to be published in *Chae et al.* (2015a) and in *Chae et al.* (2015b)). In particular, lightweight, flexible hydrofoils in cantilevered configuration subject to flow-induced spanwise bend-twist deformation were studied in water. The numerical predictions were validated with new experiments conducted by the French Naval Academy Research Institute (IRENav). The influence of viscous effects and relative mass ratio on the dynamic response and stability of flexible hydrofoils were identified for a wide range of operating conditions.

1.4 Outline

This dissertation presents the fluid-structure interaction (FSI) response and stability of lightweight, flexible hydrofoils with a focus on operation in incompressible and viscous flow. It is organized as follows: Chapter I discusses the motivation of this thesis and examines previous studies on these topics. Chapter II presents the non-dimensional equations for the solid and fluid models; the details of the derivations are shown in the Appendix. Chapter III determines the stability boundaries for a wide range of relative mass ratios ($\sqrt{\mu}$) and compares the results from published experimental, theoretical, and numerical studies. This chapter also investigates the time-histories of the deformations and hydrodynamic loads, vorticity contours, and total damping factors for the fluid-structure interaction (FSI) responses at or near the static divergence, dynamic divergence, and flutter boundaries. Chapter IV focuses on the influence of the inflow velocity and the angle of attack on flow-induced vibration characteristics of lightweight, flexible hydrofoils. This chapter determines the in-water natural frequencies and total loss factors by comparing predictions with new experimental measurements conducted by our collaborators at the French Naval Academy Research Institute (IRENav). Chapter V studies the influence of flow-induced bend-twist coupling effects on the dynamic response of lightweight, flexible hydrofoils. This chapter also examines viscous effects on flexible hydrofoils by comparing results of inviscid and viscous FSI simulations. Chapter VI presents the conclusion and discusses opportunities for future research.

CHAPTER II

Model description

2.1 Model setup

This thesis investigates the dynamic response and stability boundary of rectangular, cantilevered flexible foils in incompressible flow with and without consideration of viscous effects. The flexible hydrofoil is assumed to be chordwise rigid with only spanwise bending and twisting degrees of freedom (DOF), as shown in Fig. 2.1.

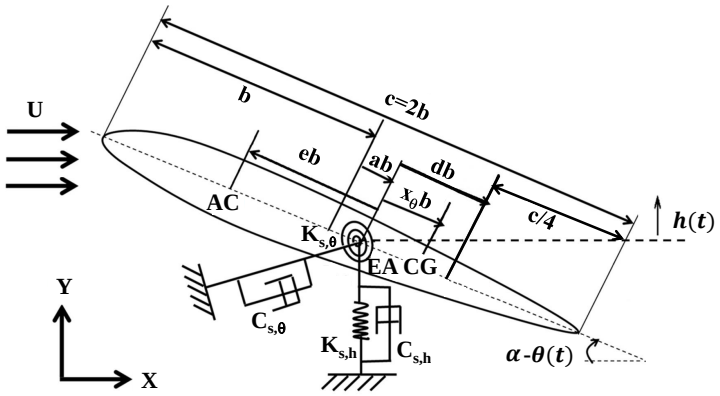

Figure 2.1: 2-DOF solid model of a cantilevered hydrofoil which spanwise bending and twisting degrees of freedom only

The bending deformation, h, and the twisting deformation, θ, are defined as positive upwards and counter-clockwise, respectively, with regard to the elastic axis (EA) of the flexible hydrofoil. The inflow velocity is defined as U, the geometric angle of

attack as α_o, and effective angle of attack as $\alpha_{\text{eff}} = \alpha_o - \theta$. EA is located at a distance ab in the downstream direction from the mid-chord, where $b = c/2$ is semi-chord length. The aerodynamic center (AC), at which the pitch moment coefficient does not vary with the lift coefficient, is located at a distance eb in the upstream direction from the EA. In inviscid flow models such as by the approach of *Theodorsen* (1935) and *Weissinger* (1947), the flow is assumed to be fully attached and the lift acts at the AC, i.e., the center of pressure (CP) is assumed to coincide with the AC. Hence e is assumed to take the value of $a + \frac{1}{2}$ (i.e., the AC is at quarter-chord from the symmetric thin foil's leading-edge). However, the actual center of pressure, where the real lift acts, changes with operating conditions, particularly for thick and rounded nose sections common to many maritime applications. The center of gravity (CG) is located at distance $x_\theta b$ in the downstream direction from the EA. In the derivation of *Theodorsen* (1935) and *Weissinger* (1947), the vortex shedding frequency is assumed to be the same as the foil oscillation frequency, and the vortices convect downstream without any dissipation. They also assume the induced downwash caused by the shed vortices in the wake to act at three quarter-chord ($3c/4$) from the foil's leading-edge, which is located at distance db in the downstream direction from the EA, where $d = a - \frac{1}{2}$. In reality, however, the vortex shedding frequency may differ from the foil oscillation frequency, may contain multiple frequencies, and the vortices may not convect downstream in the direction of flow. The vortices may also interact with the foil motions, viscous dissipation will occur, and the effective induced velocity by shed vortices may not necessarily act at $3c/4$ from the foil's leading-edge.

In Fig. 2.1, $C_{s,h}(= 2m\omega_h\zeta_{s,h})$ and $C_{s,\theta}(= 2I_\theta\omega_\theta\zeta_{s,\theta})$, $K_{s,h}(= m\omega_h^2)$ and $K_{s,\theta}(= I_\theta\omega_\theta^2)$ are, respectively, the solid damping values and solid restoring values per unit span for the foil spanwise bending and twisting motion, as indicated by the subscripts h and θ. m is the solid mass per unit span; b is the semi-chord; $I_\theta(= mr_\theta^2 b^2)$ is the solid mass moment of inertia per unit span about the EA; r_θ is the radius of gyration;

$\zeta_{s,h}$ and $\zeta_{s,\theta}$ are respectively the solid bending and twisting damping coefficients. $\omega_h = 2\pi f_h$ and $\omega_\theta = 2\pi f_\theta$ are, respectively, the first in-vacuum natural bending and twisting frequencies, which are taken be the same as the in-air natural frequencies because of the low density of air. The characteristic non-dimensional parameters governing the FSI response of a flexible hydrofoil are listed in Table 2.1, where S_θ is the static imbalance per unit span; ρ_f is the fluid density; ν_f is the fluid kinematic viscosity; and $\omega = 2\pi f$ is the foil oscillation frequency.

Table 2.1: Characteristic non-dimensional parameters of a flexible hydrofoil

Parameter	Symbol	Formula	Physical meaning
Elastic axis	a	-	Non-dimensional distance from mid-chord to foil elastic axis (EA), positive if EA is aft of the mid-chord
Aerodynamic center	e	-	Distance from EA to aerodynamic center (AC), positive if EA is aft of the AC
Three quarter chord	d	-	Distance from EA to three quarter-chord ($3c/4$), positive if $3c/4$ is aft of the EA
Center of gravity	x_θ	$S_\theta/(mb)$	Non-dimensional distance from the EA to the foil center of gravity (CG), positive for CG aft of the EA
Radius of gyration	r_θ	$\sqrt{I_\theta/(mb^2)}$	Non-dimensional radius of gyration about the EA
Solid damping coeff.	$\zeta_{s,h}$, $\zeta_{s,\theta}$	$C_{s,h}/(2m\omega_h)$, $C_{s,\theta}/(2I_\theta\omega_\theta^2)$	Solid bending and twisting damping coefficients
Relative mass ratio	μ	$m/(\pi\rho_f b^2)$	Ratio between solid inertial force and fluid inertial force for bending motion
Reduced velocity	$\overline{U}$	$U/(\omega_\theta b)$	Ratio between fluid convection frequency and solid first in-air natural twisting frequency
Reduced frequency	k	$\omega b/U$	Ratio between solid oscillation frequency and fluid convection frequency
Solid bending to twisting frequency ratio	Ω	ω_h/ω_θ	Ratio between first in-air natural bending and twisting frequency
Reynolds number	Re	$2Ub/\nu_f$	Ratio between fluid inertial force and fluid viscous force

2.1.1 Solid model

The non-dimensional two degree-of-freedom (2-DOF) solid equations of motion (EOM) can be written in condensed form as shown in Eq. (2.1). The EOM is non-dimensionalized by using b for length, $\pi\rho_f b^2$ for mass per unit span, and $1/\omega_\theta$ for time.

The twisting frequency is selected because for most flexible hydrofoils, the governing instability mechanism is static divergence, which is a loss of effective system torsional stiffness.

$$\mathbf{M}_{\mathrm{s}}\ddot{\mathbf{X}} + \mathbf{C}_{\mathrm{s}}\dot{\mathbf{X}} + \mathbf{K}_{\mathrm{s}}\mathbf{X} = \mathbf{F}_{\mathrm{static}}, \tag{2.1}$$

where $\mathbf{X} = [h/b, \theta]^T$, $\dot{\mathbf{X}}$, and $\ddot{\mathbf{X}}$ are the non-dimensional displacement, velocity, and acceleration vectors. $\mathbf{M}_{\mathrm{s}}$, $\mathbf{C}_{\mathrm{s}}$, and $\mathbf{K}_{\mathrm{s}}$ are, respectively, the non-dimensional solid inertial, damping, and stiffness matrices, which could be written as:

$$\mathbf{M}_{\mathrm{s}} = \mu \begin{bmatrix} 1 & x_\theta \\ x_\theta & r_\theta^2 \end{bmatrix}, \mathbf{C}_{\mathrm{s}} = \mu \begin{bmatrix} 2\Omega\zeta_{s,h} & 0 \\ 0 & 2r_\theta^2\zeta_{s,\theta} \end{bmatrix}, \mathbf{K}_{\mathrm{s}} = \mu \begin{bmatrix} \Omega^2 & 0 \\ 0 & r_\theta^2 \end{bmatrix}. \tag{2.2}$$

Note that the foil is assumed to be made of homogeneous, isotropic material, so there is no bend-twist coupling on $\mathbf{C}_{\mathrm{s}}$ and $\mathbf{K}_{\mathrm{s}}$. The non-dimensional static force vector, $\mathbf{F}_{\mathrm{static}}$ (shown in Eq. (2.3)) , the right hand side (RHS) of Eq. (2.1) corresponds to the steady-state lift and moment per unit span caused by initial angle of attack or camber effects, and are non-dimensionalized by $\pi\rho_f b^3\omega_\theta^2$ and $\pi\rho_f b^4\omega_\theta^2$, respectively.

$$\mathbf{F}_{\mathrm{static}} = \begin{bmatrix} L_{\mathrm{static}} \\ M_{\mathrm{static}} \end{bmatrix} = \overline{U}^2 \begin{bmatrix} 2(\alpha_o - \alpha_{Lo}) \\ 2C_{Mo,AC}/\pi - 2e(\alpha_o - \alpha_{Lo}) \end{bmatrix}, \tag{2.3}$$

where α_{Lo} is the angle of attack at which the lift force is zero. $C_{Mo,AC}$ is the steady-state moment coefficient at the aerodynamic center (AC). Note that for a symmetric flexible foil with no camber, α_{Lo} and $C_{Mo,AC}$ are both zero if $\alpha_o = 0$.

2.1.2 Fluid model

The FSI response of flexible foil is modeled using both an inviscid fluid model and a viscous fluid model, which are respectively defined by the inviscid fully coupled (FC)

method and the viscous loose hybrid coupled (LHC) method, the details of which are provided in *Young et al.* (2012), *Chae et al.* (2013), and *Akcabay et al.* (2014).

2.1.2.1 Inviscid fluid model

The inviscid fluid model uses the potential flow solution of *Theodorsen* (1935) (assuming an inviscid, irrotational, and incompressible fluid). The approach of *Theodorsen* (1935) is derived for a thin two-dimensional (2D) foil undergoing small harmonic pitching and plunging motion. It assumes the lift and moment to contain both circulatory and non-circulatory parts with a flat, zero thickness trailing wake sheet parallel to the inflow. Theodorsen also assumed the lift to act at $c/4$ from the foil's leading edge (i.e., $e = a + \frac{1}{2}$), the vortices to shed downstream parallel to the inflow without any dissipation, and the induced downwash to act at $3c/4$ from the foil leading edge (i.e., $d = a - \frac{1}{2}$). The non-dimensional inviscid fluid force vectors, $\mathbf{F}^T_{\text{FSI}}$, are expressed by *Theodorsen* (1935) in terms of the inviscid fluid lift (L^T_{FSI}) and moment (M^T_{FSI}) per unit span acting on the foil.

$$\mathbf{F}^T_{\text{FSI}} = \begin{bmatrix} L^T_{\text{FSI}} \\ \\ M^T_{\text{FSI}} \end{bmatrix} = -\mathbf{M}^T\ddot{\mathbf{X}} - \mathbf{C}^T\dot{\mathbf{X}} - \mathbf{K}^T\mathbf{X}. \tag{2.4}$$

In Eq. (2.4), $\mathbf{M}^T$, $\mathbf{C}^T$, and $\mathbf{K}^T$ are, respectively, the non-dimensional inviscid fluid inertial, damping, and stiffness matrices. $C(k)$ present Theodorsen's circulation function (*Theodorsen*, 1935), Eq.(2.5), which accounts for the circulatory load on the foil induced by the shed vortices in the wake in Eqs. (2.6) - (2.8). k is the reduced foil oscillation frequency.

$$C(k) = F(k) + iG(k) = \frac{H_1^2(k)}{H_1^2(k) + iH_0^2(k)}. \tag{2.5}$$

where $H_1^2(k)$ and $H_0^2(k)$ are Hänkel functions (i.e., 3^{rd} kind Bessel functions).

$$\mathbf{M}^T = \begin{bmatrix} \mathrm{M}_{11}^T & \mathrm{M}_{12}^T \\ \mathrm{M}_{21}^T & \mathrm{M}_{22}^T \end{bmatrix} = \begin{bmatrix} 1 & -a \\ -a & \frac{1}{8} + a^2 \end{bmatrix}, \tag{2.6}$$

$$\begin{aligned} \mathbf{C}^T &= \begin{bmatrix} \mathrm{C}_{11}^T & \mathrm{C}_{12}^T \\ \mathrm{C}_{21}^T & \mathrm{C}_{22}^T \end{bmatrix} = \overline{U} \begin{bmatrix} 2C(k) & 1 - 2C(k)d \\ -2C(k)e & d[2C(k)e - 1] \end{bmatrix} \\ &= \overline{U} \begin{bmatrix} 2C(k) & 1 + C(k)(1 - 2a) \\ -C(k)(2a+1) & \left(\frac{1}{2} - a\right)[1 - C(k)(2a+1)] \end{bmatrix}, \end{aligned} \tag{2.7}$$

$$\mathbf{K}^T = \begin{bmatrix} \mathrm{K}_{11}^T & \mathrm{K}_{12}^T \\ \mathrm{K}_{21}^T & \mathrm{K}_{22}^T \end{bmatrix} = \overline{U}^2 \begin{bmatrix} 0 & 2C(k) \\ 0 & -2C(k)e \end{bmatrix} = \overline{U}^2 \begin{bmatrix} 0 & 2C(k) \\ 0 & -C(k)(2a+1) \end{bmatrix} \tag{2.8}$$

Comparison of Eqs. (2.2) and (2.4) suggests that for lightweight foils in dense fluid such that $\sqrt{\mu} < 1$, the relative contribution of the fluid inertial and damping terms will be higher than that of the solid terms.

Note that *Theodorsen*'s solution assumes small, harmonic foil motion and fully attached flow on a thin foil. Theodorsen also assumed the 1) lift to act at $c/4$ from the foil's leading edge (i.e. $e = a + \frac{1}{2}$), 2) the vortices to shed downstream parallel to the inflow without any dissipation, and 3) the induced downwash to act at $3c/4$ from the foil leading edge (i.e. $d = a - \frac{1}{2}$). These assumptions are not necessarily valid, which will in turn affect the accuracy of the fluid damping and stiffness terms, $\mathbf{C}^T$ and $\mathbf{K}^T$, and hence the in-water natural frequencies and total loss factors. The fluid inertial term, $\mathbf{M}^T$, on the other hand, is mainly driven by pressure effect, and hence

is minimally impacted by viscous effects. The influence of viscous effects on $\mathbf{C}^T$ and $\mathbf{K}^T$, and the presence of flow-induced coupling (off-diagonal terms in $\mathbf{C}^T$ and $\mathbf{K}^T$) are responsible for the dependence of the in-water vibration frequencies with operating condition and the over-prediction of the loss factors by inviscid, uncoupled mode solution introduced in *Blake and Maga* (1975), both of which will be demonstrated later in chapter V.

2.1.2.2 Viscous Fluid Model

For the viscous fluid model, the current simulation solves the unsteady Reynolds-averaged Navier-Stokes (uRANS) equations with the $k-\omega$ shear stress transport ($k-\omega$ SST) turbulence model for an incompressible Newtonian fluid with negligible body forces, as shown in Eqs. (2.10)-(2.9).

$$\frac{\partial \overline{\mathbf{u}}_f}{\partial \overline{t}} + \overline{\mathbf{u}}_f \cdot \overline{\nabla}\overline{\mathbf{u}}_f = -\overline{\nabla}\,\overline{P}(\frac{Eu\,\overline{U}^2}{2}) + \overline{\nabla}\cdot\left(\frac{2\overline{U}}{Re_{\text{eff}}}\left(\overline{\nabla}\overline{\mathbf{u}}_f + \overline{\nabla}\overline{\mathbf{u}}_f^T\right)\right) \tag{2.9}$$

$$\overline{\nabla}\cdot\overline{\mathbf{u}}_f = 0 \tag{2.10}$$

Note that the uRANS equations shown in Eqs. (2.9) - (2.10) was non-dimensionalized by using b for length, P_o (the static pressure) for reference pressure, $1/\omega_\theta$ for time, and $\omega_\theta b$ for velocity. $\overline{\mathbf{u}}_f$ is the non-dimensional local fluid velocity, $\overline{t}$ is the non-dimensional time, $\overline{P}$ is the non-dimensional total pressure, $\overline{U}$ is the reduced velocity, $Eu = \frac{2P_o}{\rho_f U^2}$ is the Euler number, and $Re_{\text{eff}} = \frac{Uc}{\nu_{\text{eff}}}$ is the effective Reynolds number. P_o is the static pressure, and ν_{eff} is the fluid effective kinematic viscosity. The viscous simulation solves Eqs. (2.9)-(2.10) via the *ANSYS-CFX* (2011) commercial software.

The local velocity must be the same for the fluid and the solid at the common interface, and the interface traction acting on the fluid and the solid should be equal

and opposite in direction.

$$\overline{\mathbf{u}}_f = \overline{\mathbf{u}}_s, \tag{2.11}$$

$$\overline{\boldsymbol{\sigma}}_f \cdot \mathbf{n} + \overline{\boldsymbol{\sigma}}_s \cdot \mathbf{n} = 0, \tag{2.12}$$

$$\overline{\boldsymbol{\sigma}}_f \cdot \mathbf{t} + \overline{\boldsymbol{\sigma}}_s \cdot \mathbf{t} = 0, \tag{2.13}$$

$$\overline{\boldsymbol{\sigma}}_f = -\frac{Eu}{2}\overline{P}\mathbf{I} + \frac{2}{Re_{\text{eff}}\overline{U}}(\overline{\nabla}\overline{\mathbf{u}}_f + \overline{\nabla}\overline{\mathbf{u}}_f^T), \tag{2.14}$$

where the subscripts "s" and "f" denote the solid and fluid parameters, respectively. $\mathbf{n}$ and $\mathbf{t}$ are, respectively, a unit normal (positive out of the body) and tangential vector on the foil surface. $\overline{\boldsymbol{\sigma}}$ is the non-dimensional total stress tensor for a Newtonian fluid, and $\mathbf{I}$ is the identity matrix.

The non-dimensional viscous fluid lift and moment acting on the hydrofoil, $\mathbf{F}_{\text{CFD}}$, from *ANSYS-CFX* (2011), are computed as follows in Eq. (2.15).

$$\mathbf{F}_{\text{CFD}} = \begin{bmatrix} L_{\text{CFD}} \\ \\ M_{\text{CFD}} \end{bmatrix} = \begin{bmatrix} \oint_A (\mathbf{j} \cdot \overline{\boldsymbol{\sigma}}_f \mathbf{n}) \mathrm{d}A \\ \\ \oint_A (\mathbf{r} \times \overline{\boldsymbol{\sigma}}_f \mathbf{n}) \mathrm{d}A \end{bmatrix}, \tag{2.15}$$

where $\mathbf{j}$ is a unit vector along the Y direction as shown in Fig. 2.1, and $\mathbf{r}$ is a vector from the EA to a point on the closed foil surface (A).

Even though the large eddy simulation (LES) would be more accurate than uRANS, particularly for cases dominated by transient, large scale vortices, LES needs a very fine mesh and very small time step sizes to resolve the most energetic eddies. Particularly near the wall regions, where the attached boundary layers are important, LES will give poor predictions unless very fine grids are used. Hence, the uRANS is used in this thesis instead of LES as a compromise between accuracy and computational efficiency for transient high Reynolds number flows, as shown in this thesis. Convergence study with time step size and validation studies with multiple experi-

mental data are shown in Chapters III and IV, respectively. Nevertheless, high-fidelity FSI simulations with LES should be studied in the future to better capture unsteady interaction between flexible foil motions and vorticity field.

In this thesis, the $k-\omega$ SST turbulence model is used with the uRANS solver; it combines the advantages of the $k-\epsilon$ model away from the wall and the $k-\omega$ model near the wall. Therefore, the $k-\omega$ SST turbulence model has been shown to be able to accurately predict of the boundary layer separation and turbulence behaviors of flexible foils at high Reynolds numbers (*Ducoin and Young*, 2013).

2.1.3 FSI coupling model

Both inviscid and viscous FSI coupling models are presented in the subsections below. It should be noted that the inviscid FSI coupling model was iterated to get the initial oscillation reduced frequency (k), and the viscous FSI coupling model used the same initial k from the result of inviscid FSI coupling model.

2.1.3.1 Inviscid FSI Coupling Model

The inviscid FSI coupling model employs a time domain (TD) fully coupled (FC) method. The FC method is possible because the analytical representation of both the solid and the inviscid fluid forces are known, where the fluid forces are given by *Theodorsen* (1935). The discretized non-dimensional inviscid, fully coupled equation of motion (EOM) is shown in Eq. (2.16).

$$(\mathbf{M}_{\mathrm{s}}+\mathbf{M}^{T})\ddot{\mathbf{X}}_{n}+(\mathbf{C}_{\mathrm{s}}+\mathbf{C}^{T})\dot{\mathbf{X}}_{n}+(\mathbf{K}_{\mathrm{s}}+\mathbf{K}^{T})\mathbf{X}_{n}=\mathbf{F}_{\mathrm{static}}, \tag{2.16}$$

where the subscript n is the time-step index.

2.1.3.2 Viscous FSI Coupling Model

The viscous FSI coupling model employs a time domain (TD) loose hybrid coupled (LHC) method introduced in *Young et al.* (2012), *Chae et al.* (2013), and *Akcabay et al.* (2014) to couple the partitioned viscous computational fluid dynamics (CFD) and computational structural dynamics (CSD) solvers to model flexible structures in dense, incompressible flow. A partitioned FSI coupling method is used because of the conveniences associated with using modular CFD and CSD solvers. Classically, partitioned FSI methods couple the two different CFD and CSD solvers via either the loosely-coupled (LC) or tightly-coupled (TC) techniques. The LC technique uses the CFD solution at the previous time-step as an input to the CSD solution for the new time-step, while the TC technique iterates between the solutions of the CFD and CSD solvers per each new time-step. Previous works of *Chen and Wambsganss* (1972); *Paidoussis* (1973); *Belanger et al.* (1995); *Mok and Wall* (2001); *Causin et al.* (2005); *Forster et al.* (2007); *Young* (2007, 2008); *Xiao and Batra* (2012) have shown that traditional LC and TC methods are not suitable for problems involving lightweight solids in incompressible, heavy fluids due to numerical instability issues associated with artificial added mass effects, which are caused by time-lag in the exchange of surface tractions and deformations between the fluid and solid solvers. The discretized EOM of the non-dimensional viscous LHC method in a time domain is given in Eq.(2.17).

$$(\mathbf{M}_{\mathrm{s}} + \mathbf{M}^T)\ddot{\mathbf{X}}_{n+1} + (\mathbf{C}_{\mathrm{s}} + \mathbf{C}^T)\dot{\mathbf{X}}_{n+1} + (\mathbf{K}_{\mathrm{s}} + \mathbf{K}^T)\mathbf{X}_{n+1} = (\mathbf{F}_{\mathrm{CFD}})_n - (\mathbf{F}^T_{\mathrm{FSI}})_n, \quad (2.17)$$

$\mathbf{F}_{\mathrm{CFD}}$ is the non-dimensional viscous fluid force on the foil that is computed by the CFD solver, which includes both static and dynamic force components. The LHC method subtracts the potential flow estimate of the hydroelastic force that depends on the flow-induced deformations, $\mathbf{F}^T_{\mathrm{FSI}}$, from both the left and right sides of the

EOM. For a thin rectangular foil, the LHC method estimates $\mathbf{F}_{\text{FSI}}^{T}$ using Theodorsen's derivation, as given in Eqs.(2.6)-(2.8). Eq.(2.17) is solved using a semi-implicit Crank-Nicholson method, which is second-order accurate in time.

The flow chart for the LHC algorithm is given in Fig. 2.2. $\mathbf{X}_o = [h_o/b, \theta_o]^T$ are the non-dimensional initial prescribed displacements. $\mathbf{X}_o$, $\dot{\mathbf{X}}_o$ are respectively the non-dimensional initial deformations and velocity of deformations. In this study, the commercial *ANSYS-CFX* (2011) software is used as the CFD solver, but other commercial or in-house CFD solvers could be used as well with the LHC algorithm.

Notice that the LHC method does not require the sub-iterations between the solid and fluid solvers. A detailed study of the numerical convergence and accuracy of the LHC method can be found in *Akcabay et al.* (2015).

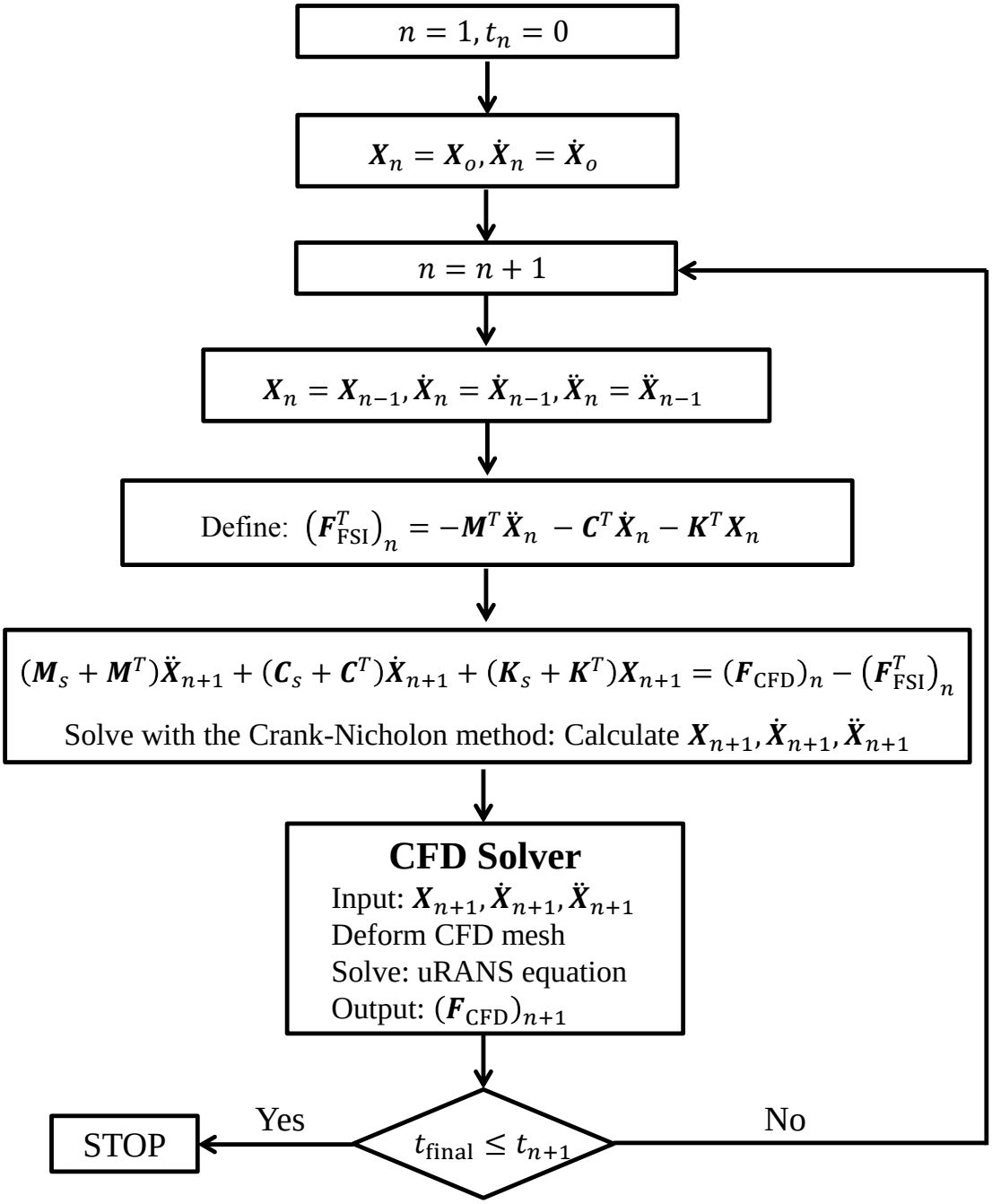

Figure 2.2: Loose hybrid coupled (LHC) algorithm flow chart

CHAPTER III

Stability boundary

In this chapter, the stability boundaries and fluid-structure interaction (FSI) responses of static divergence, dynamic divergence, and flutter are determined. Section 3.1 presents a model setup of numerical simulations and comparisons with published experiments for the stability boundaries and FSI responses of a NACA16-010 foil. Section 3.2 investigates the influence of relative mass ratio on the static and dynamic stability boundaries, as well as oscillation frequency. Inviscid and viscous FSI predictions are compared with published experimental data. Section 3.3 shows the FSI responses using the time-histories of the predicted bending and twisting deformations, as well as lift and moment coefficients at various mass ratios. Section 3.4 presents the total damping coefficients and vibration frequencies predicted using inviscid and viscous FSI solvers. Specifically, the critical flutter speed corresponds to the time at which the total damping coefficient becomes zero.

3.1 NACA16-010 model setup

The physical parameters for a NACA16-010 foil used in current numerical simulations and published experimental tests (*Woolston and Castile*, 1951; *Besch and Liu*, 1971) are listed in Table 3.1. Note that since the current simulations are conducted with a 2D fluid solver, the mass, damping, and stiffness values of the foils in Table

3.1 are given per unit span length. In all the simulations of NACA16-010 shown in this section, solid damping is ignored (i.e., $\zeta_{s,h} = 0$ and $\zeta_{s,\theta} = 0$).

Table 3.1: NACA16-010 physical parameters

Parameter	Current simulation	Woolston & Castile (1951)	Besch & Liu (1971)
Foil	NACA 16-010	NACA 16-010	NACA 16-012
Material	Epoxy & Lead powder Balsa wood	Balsa wood	Lead and Tin, Epoxy & Lead powder, Epoxy & Glass-microballoon
Fluid	Water Freon 21 & Air mixtures	Freon 21 & Air mixtures	Water
c $[m]$	0.305	0.305	0.152
s $[m]$	1.219	1.219	0.381
AR [-]	0.003	4	2.5
τ/c [-]	0.1	0.1	0.12
α_o [°]	0	0	0
a [-]	-0.218 and -0.5	-0.218	-0.5
x_θ [-]	0.068 and 0.524	0.068	0.523 – 0.524
r_θ [-]	0.403 and 0.709	0.403	0.709 – 0.713
E_s [GPa]	1.80 and 2.34	1.80	1.59 – 1.63
ν_s [-]	0.36	0.36	N/A
m $[kg/m]$	0.63 – 286.06	0.63	3.94 – 17.55
ρ_f $[kg/m^3]$	0.5 – 1000	0.08 – 3.18	1000
ν_f $[m^2/s]$	1.0×10^{-6} – 1.12×10^{-5}	2.85×10^{-6} – 1.19×10^{-4}	1.0×10^{-6}
Re [-]	0.35×10^{6} – 4.27×10^{6}	0.41×10^{6} – 1.84×10^{6}	1.94×10^{6} – 2.82×10^{6}
$\sqrt{\mu}$ [-]	0.3 – 4.18	1.65 – 10.52	0.45 – 0.98
f_h [Hz]	0.72 – 17.65	15.29	11.09 – 22.49
f_θ [Hz]	1.74 – 52.11	36.92	35.09 – 68.75

3.1.1 NACA16-010 mesh setup

The numerical NACA16-010 mesh for the CFD solver is shown in Fig. 3.1. The numerical mesh consists of unstructured triangular elements everywhere except at the boundary layer region near the foil, which is discretized with the structured mesh.

The smallest element near the foil surface satisfies $y^+ \approx 1$. The mesh is refined near the foil's leading and trailing edges, as well as in the wake region, in order to capture the flow details. The boundary conditions are uniform flow with 3% turbulence intensity at the inlet (i.e., left-end of the numerical domain shown in Fig. 3.1), symmetry conditions at the top and bottom of the fluid domain, solid-wall boundary conditions on the foil surface, and prescribed pressure boundary conditions at the outlet. The mesh elements are deformed according to the computed bending and twisting displacements of the hydrofoil at each time-step. The numerical simulations are initialized from the steady-state solution of the fluid flow around the foil with a $\theta_o = -2^\circ$ initial twist angle and $h_o = 0$.

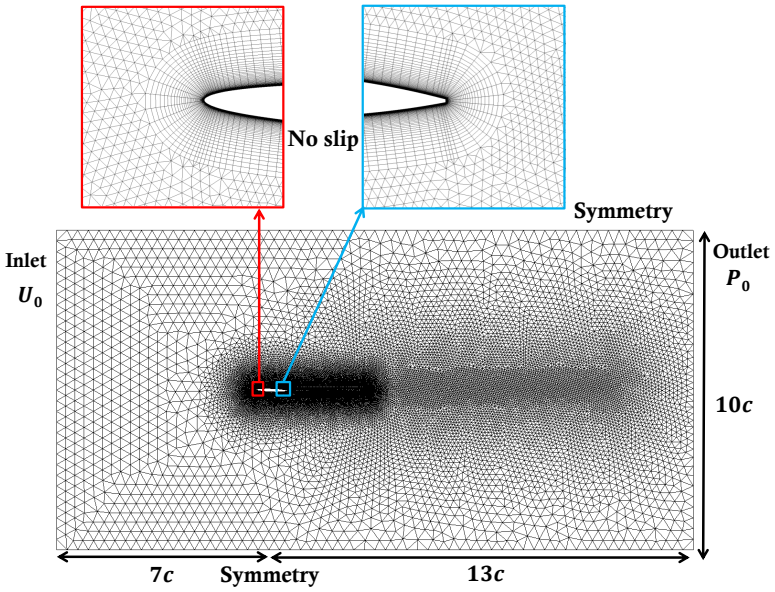

Figure 3.1: The 2D NACA16-010 mesh, which is discretized with approximately 76,000 elements and 48,000 nodes.

For the mesh deformation algorithm as shown in *ANSYS-CFX* (2011), the mesh elements are deformed to conform to the hydrofoil geometry according to the foil motions obtained by using the viscous loose hybrid coupled (LHC) method at each time-step. The numerical simulations of the flexible hydrofoil are initialized from the steady-state solution of flow around a stationary hydrofoil. All the CFD simulations

assume the flow to be fully turbulent and are performed at $Re = 3.5\times10^5 \sim 4.27\times10^6$ and $\overline{U} = 0.16 \sim 1.9$ with geometric angles of attack (α_o) of 0° with zero initial bending deformation and -2° initial twisting deformation.

3.1.2 Numerical convergence studies for NACA16-010

Mesh and time convergence studies were conducted for the case corresponding to a rectangular, cantilevered NACA16-010 balsa wood foil with an $AR = 4$ in a Freon 21-air mixture with $Re = 1.24\times10^6$, $\sqrt{\mu} = 2.79$, and $\overline{U} = 1.3$; the relevant experimental description is available at *Woolston and Castile* (1951), and the key parameters are listed in Table 3.1. In all the convergence results shown in this subsection, the time-history plots are non-dimensionalized by the first in-air natural twisting frequency, $\omega_\theta = 232$ rad/s.

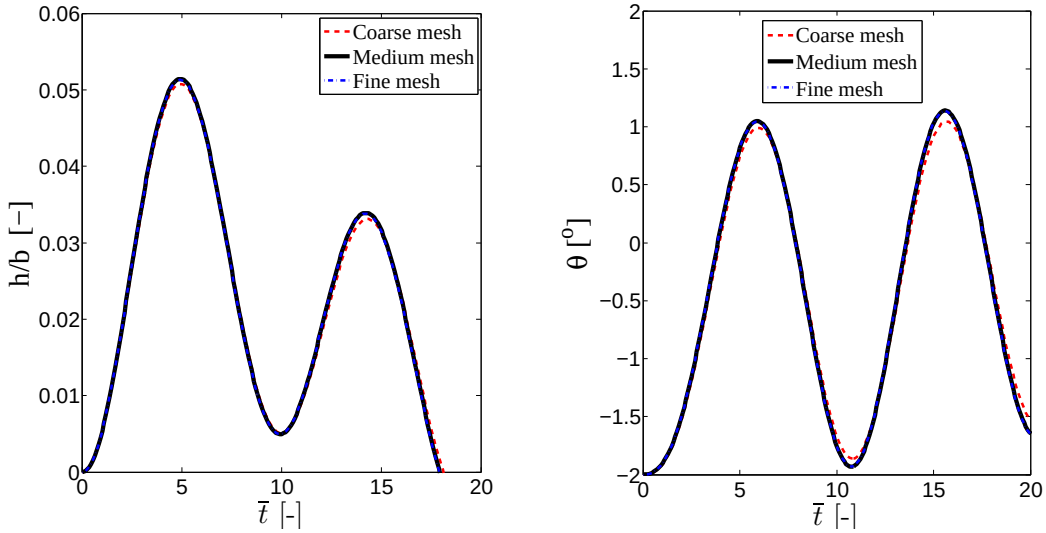

(a) Bending deformations (h/b)

(b) Twisting deformations (θ)

Figure 3.2: Mesh convergence study of (a) bending deformations and (b) twisting deformations for the flexible NACA16-010 foil at $\Delta t = 0.0004s$ with $\alpha_o = 0^o$, $\sqrt{\mu} = 2.79$, $\overline{U} = 1.3$, and $Re = 1.24\times10^6$. Note that "coarse mesh" has 3.4×10^4 nodes and 5.2×10^4 elements, "medium mesh" has 4.8×10^4 nodes and 7.6×10^4 elements, and "fine mesh" has 10.7×10^4 nodes and 18.4×10^4 elements. $\bar{t} = t\omega_\theta$ is the non-dimensional time.

For the mesh convergence study, three different meshes are used with $\Delta\bar{t} = \Delta t\omega_\theta \approx$

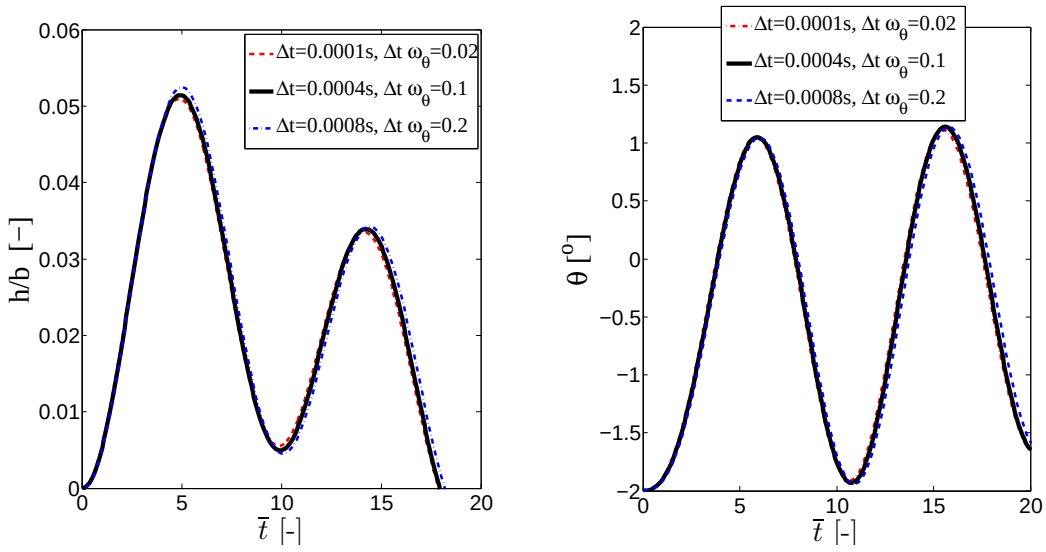

(a) Bending deformations (h/b) (b) Twisting deformations (θ)

Figure 3.3: Time convergence study of (a) bending deformations and (b) twisting deformations for the flexible NACA16-010 foil on the "medium mesh" (4.8×10^4 nodes and 7.6×10^4 elements) with $\alpha_o = 0^o$, $\sqrt{\mu} = 2.79$, $\overline{U} = 1.3$, and $Re = 1.24 \times 10^6$. Note that $\bar{t} = t\omega_\theta$ is the non-dimensional time.

0.1 (i.e., $\Delta t = 4 \times 10^{-4}$ s). The coarse mesh approximately contains 34,000 nodes and 52,000 elements; the medium mesh approximately contains 48,000 nodes and 76,000 elements; and the fine mesh approximately contains 107,000 nodes and 184,000 elements. Fig. 3.2 shows that the predicted time-histories of the bending and twisting deformations with the medium mesh are sufficiently close with the predictions evaluated with the fine mesh. Hence, from here on, the medium mesh is used to calculate the viscous FSI responses.

For the time convergence study, the predicted time-histories of the bending and twisting deformations using three different time-step sizes ($\Delta\bar{t} = \Delta t\omega_\theta \approx 0.02$, 0.1, and 0.2) on the "medium mesh" are compared in Fig. 3.3. Note in Fig. 3.3 that the predictions obtained using the two smallest time-steps are close. Hence, in the simulations shown from here on, a time-step size of $\Delta t = 0.0004$s corresponding to $\Delta\bar{t} \leq 0.1$ will be used. This corresponds to a Courant-Friedrichs-Lewy ($CFL = U\Delta t/\Delta x$) number between 0.07 to 6.70 for the various cases shown in this chapter.

In addition to these convergence studies, the simulations are validated through comparison with various experimental data, which will be shown in section 3.2.

3.1.3 Prediction of flutter, static divergence, and dynamic divergence

In all the simulations, the flutter boundary is determined by seeking the minimum critical inflow velocity at which the total damping of the vibrating system, ζ_T, is zero. Note that the total damping is the sum of the solid and fluid damping (i.e., $\zeta_T = \zeta_s + \zeta_f$). The logarithmic decrement method for calculating ζ_T is used in this section, and it is demonstrated through Fig. 3.4, and in Eqs.(3.1) and (3.2).

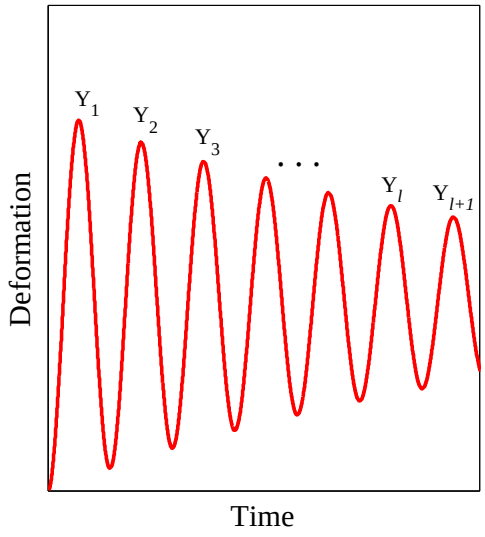

Figure 3.4: Sample time-history of the deformation used to determine the total damping coefficient, ζ_T, via the logarithmic decrement method.

$$\delta = \frac{1}{l} ln \left(\frac{Y_1}{Y_{l+1}} \right), \tag{3.1}$$

$$\zeta_T = \frac{\delta}{\sqrt{4\pi^2 + \delta^2}}. \tag{3.2}$$

where l is the number of the peak points between Y_1 and Y_{l+1} (i.e., the maximum amplitude of the deformation at the each number of the peak points). δ is the

logarithmic decrement. Fig. 3.4 is a sample time-history of deformation. The flutter boundary is determined through interpolating the critical $\overline{U}$ for which ζ_T is zero.

The static divergence velocity, U_d, is the critical speed at which the effective torsional stiffness (i.e., sum of both solid stiffness and fluid stiffness) of the foil becomes zero. From the balance between the flow-induced disturbing moment and the solid elastic restoring moment, the linear theory estimates U_d as:

$$U_d = \sqrt{\frac{k_\theta}{\rho_f e b^2 \frac{\partial C_L}{\partial \alpha}}}, \tag{3.3}$$

where the linear theory takes $e = a + \frac{1}{2}$ and $\frac{\partial C_L}{\partial \alpha} = 2\pi$. Note that for a given solid, the dimensional value of U_d decreases with increasing ρ_f according to Eq.(3.3), but U_d does not vary with ρ_s as long as K_θ remains the same.

In a time domain viscous LHC method solution, the static divergence velocity is determined as the speed at which the deformations monotonically increase without an obvious oscillation frequency, and the dynamic divergence velocity is determined as the speed for when the mean deformations grow with a decaying oscillation frequency. It should be mentioned here that dynamic divergence is a nonlinear phenomenon according to *Kousen and Bendiksen* (1988); *Bendiksen* (1992, 2002), and it is only predicted in this work using the LHC viscous FSI solver through a time domain solution method.

3.2 Static and dynamic stability boundaries

The current time domain (TD) solutions obtained using the inviscid FC and viscous LHC method are compared with frequency domain (FD) solutions of the linear potential theory predictions, and with experimental measurements of the critical divergence velocities, flutter velocities and frequencies given in *Woolston and Castile* (1951) and *Besch and Liu* (1971) for cases with different relative mass ratios ($\sqrt{\mu}$),

as shown in Table 3.1.

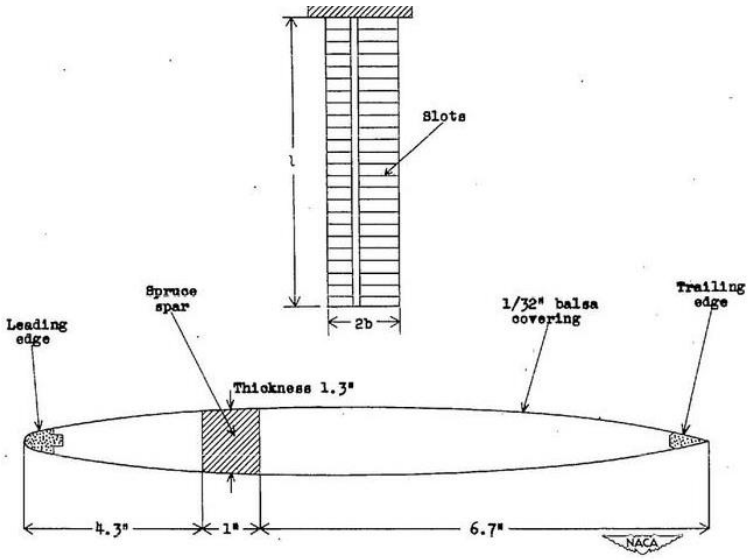

Figure 3.5: *Woolston and Castile* (1951)'s experimental model of a cantilevered NACA16-010 foil in Freon 21 and air mixtures.

Woolston and Castile (1951)'s experiments cover a $\sqrt{\mu}$ range ($1.65 \leq \sqrt{\mu} \leq 10.52$) that correspond to the typical operating conditions of light airfoils and Micro Air Vehicles (MAV). The flutter velocities and frequencies those studies were measured for a rectangular cantilevered balsa wood NACA 16-010 foil in Freon 21 and air mixtures with different fluid densities. The cantilevered NACA16-010 foil has a chord length (c) of 0.305 m and a span length (s) of 1.219 m, as shown in Fig. 3.5. These experiments were performed in a wind tunnel, which had a circular cross section of 1.37 m in diameter. The Re was between 4.1×10^5 and 1.84×10^6. The flutter velocities were determined as the speeds for when the total system damping was projected to be zero.

Besch and Liu (1971)'s experiments were conducted in a depressurized 36 in (=0.9 m) water tunnel at the Naval Ship Research and Development Center (NSRDC), where the maximum attainable speed was 25.72 m/s. The geometry corresponds to a rectangular NACA16-012 foil with c=0.152 m , s=0.381 m, and it is cantilevered

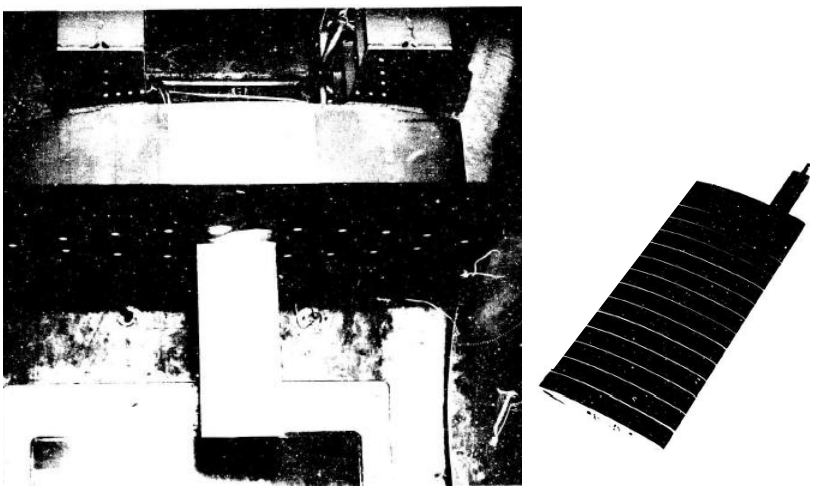

Figure 3.6: *Besch and Liu* (1971)'s experimental model of a cantilevered NACA16-012 foil inside a depressurized 36 in (=0.9 m) re-circulating water tunnel.

at the root with a quarter chord pitching point, as shown in Fig. 3.6. The Re was between 1.94×10^6 and 2.82×10^6. The relative mass ratios ($0.45 \leq \sqrt{\mu} \leq 0.98$) were controlled by using different materials (i.e., lead and tin, epoxy and lead powder, epoxy and glass micro balloons in water) to construct the NACA 16-012 hydrofoils. Again, the flutter inception speeds were determined by projecting the speed at which the total damping coefficient was zero.

As shown in Figs. 3.7 and 3.9, the linear theory and experimental results obtained by *Woolston and Castile* (1951) are in good agreement with each other for $\sqrt{\mu} > 3$. It is important to note that *Woolston and Castile*'s results shown in Figs. 3.7 and 3.9 are limited to $\sqrt{\mu} > 1.5$, due to the use of balsa wood for the foil, and the limited range of fluid densities that can be achieved by using a Freon 21 and air mixture in a wind tunnel. On the other hand, *Besch and Liu* (1971)'s experimental results given in Fig. 3.8 contain data for $\sqrt{\mu} \leq 1$ only, since they used water as the experimental test fluid. It should be noted that *Woolston and Castile* (1951)'s linear theory results used the frequency domain solution technique, while the current inviscid FC and viscous LHC simulations used the time domain solution technique.

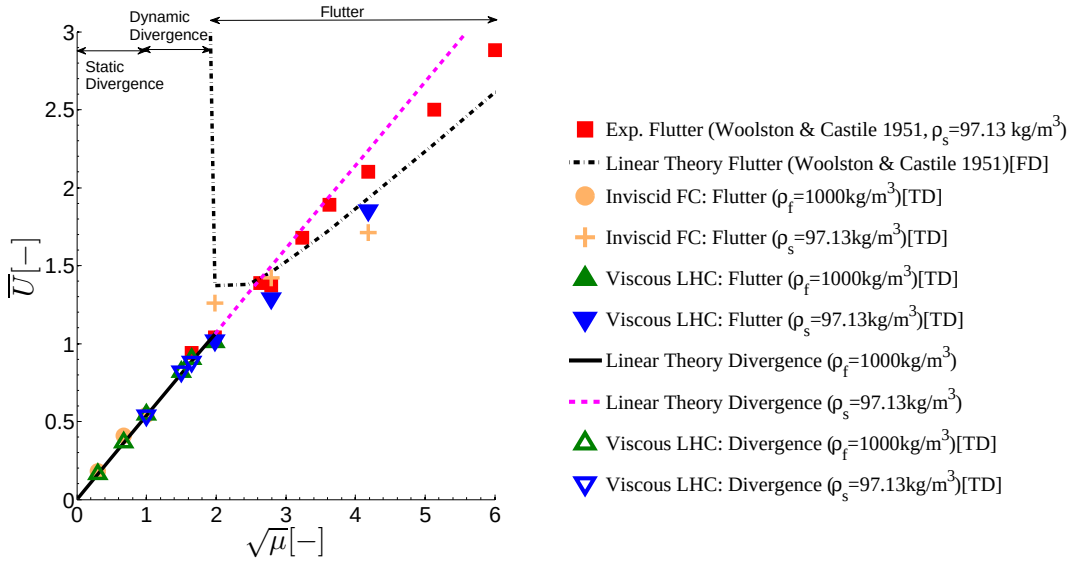

Figure 3.7: Static/dynamic divergence and flutter velocity boundaries as a function of the relative mass ratio ($\sqrt{\mu}$) based on *Woolston and Castile* (1951)'s data for NACA 16-010 foil in Freon 21 and air mixtures with predicted results by fixed ρ_f or ρ_s.The linear theory divergence velocities are calculated by Eq.(3.3). Note that the closed symbols represent flutter and open symbols represent divergence. The triangle symbols represent cases where $\sqrt{\mu}$ is varied by changing ρ_s and fixing $\rho_f = 1000kg/m^3$, and the inverted triangle symbols represent cases where $\sqrt{\mu}$ is varied by changing ρ_f and fixing $\rho_s = 97.13kg/m^3$ in the viscous FSI simulations. ($a = -0.218$, $x_\theta = 0.068$, and $r_\theta = 0.403$).

Figures 3.7 and 3.8 suggest that with decreasing $\sqrt{\mu}$, the reduced flutter velocity ($\overline{U}_f$) and the reduced divergence velocity ($\overline{U}_d$) will both decrease. According to Eq. (3.3) for a given foil with a fixed material, the dimensional values of U_d will only decrease as the ρ_f increases (the dimensional U_d is not a function of ρ_s). However, the reduced divergence velocity ($\overline{U}_d$) decreases with reductions in ρ_s because ω_θ increases as ρ_s decreases.

Figures 3.7 - 3.9 show that the predicted flutter and divergence boundaries using the current viscous LHC simulations are in good agreement with the experimental results of *Woolston and Castile* (1951) and *Besch and Liu* (1971). However, as shown in Fig. 3.7, the frequency domain linear theory solution predicts higher flutter velocity than measured for $\sqrt{\mu} < 3$, which is dangerous because that means the actual system

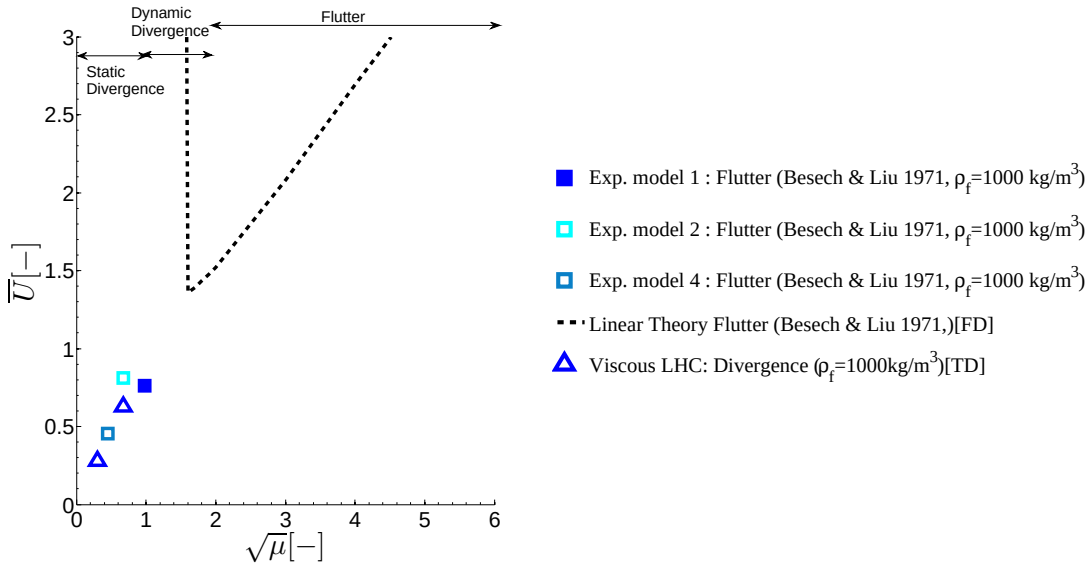

Figure 3.8: Static/dynamic divergence and flutter velocity boundaries as a function of the relative mass ratio ($\sqrt{\mu}$) based on *Besch and Liu* (1971)'s data for NACA 16-012 foil in water and with numerical predictions obtained by varying ρ_s but fixed ρ_f. The linear theory for divergence velocity shown in Eq.(3.3); predicted $U_d = \infty$ for *Besch and Liu*'s case shown in Fig. 3.8 due to the coincidence of EA and AC, and hence is not shown in Fig. 3.8. Note that the closed symbols represent flutter and open symbols represent divergence. The triangle symbols represent cases where $\sqrt{\mu}$ is varied by changing ρ_s and fixing $\rho_f = 1000 kg/m^3$ in the viscous FSI simulations. ($a = -0.5$, $x_\theta = 0.524$, and $r_\theta = 0.709$)

will flutter earlier than the linear theory prediction. This discrepancy is because the linear potential theory of flutter assumes small harmonic deformations, which are not necessarily valid for cases with low relative mass ratios. Note that as fluid inertial and damping effects increase with increasing ρ_f, the foil motion will no longer be harmonic because the oscillations will be damped out quickly and viscous effects become relatively more important as $\sqrt{\mu}$ decreases. Hence, the inviscid frequency domain linear theory is not suitable for flutter predictions of light foils in a dense fluid, such as most hydrofoils. For $1 \leq \sqrt{\mu} < 2$ (in the range of very heavy hydrofoils or very light airfoils), the dynamic divergence and flutter boundaries are very close. It is worth it to point out that while the flutter velocities were reported by *Woolston*

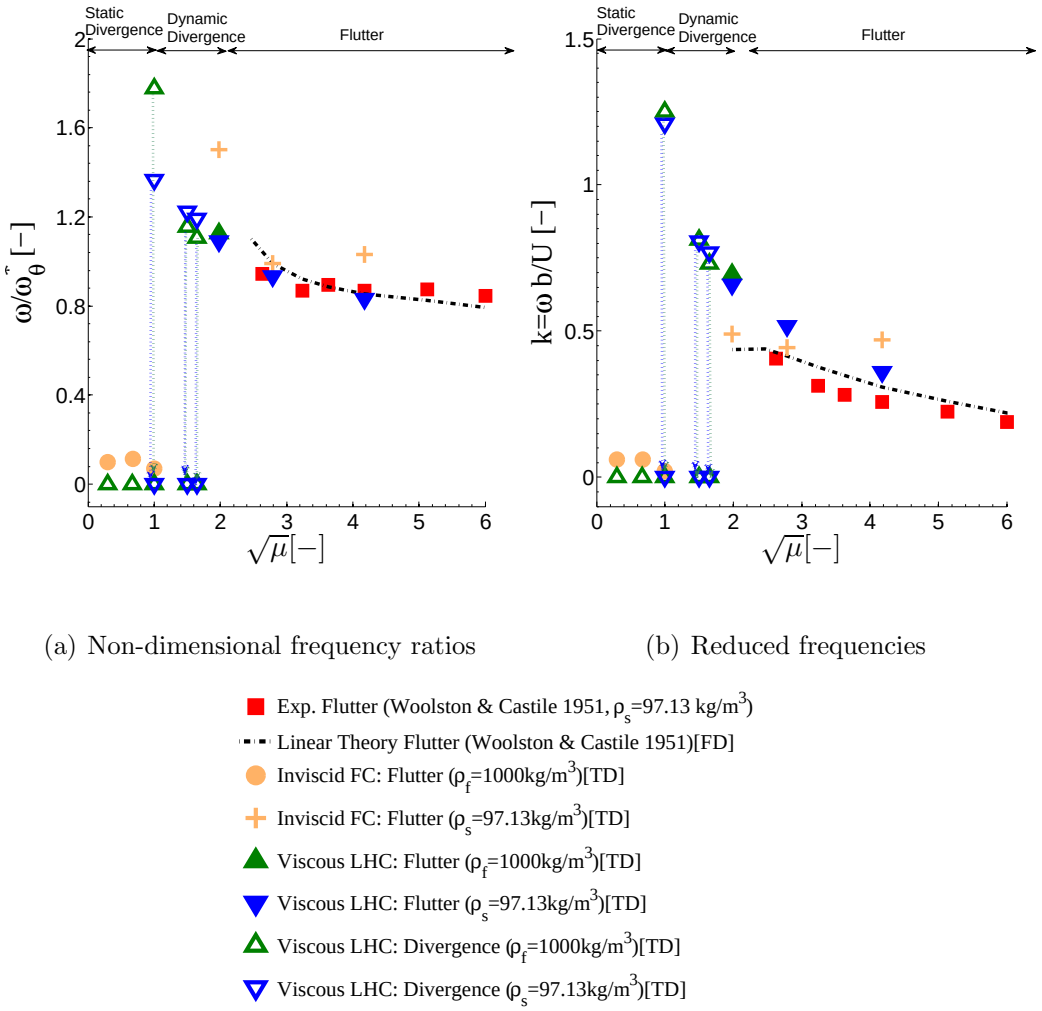

(a) Non-dimensional frequency ratios (b) Reduced frequencies

Figure 3.9: Static/dynamic divergence and flutter in (a) non-dimensional frequency ratios and (b) reduced frequencies as a function of relative mass ratio ($\sqrt{\mu}$) based on *Woolston and Castile* (1951)'s data for NACA 16-010 foil in Freon 21 and air mixtures with predicted results by fixed ρ_f or ρ_s. Note that the closed symbols represent flutter and open symbols represent divergence. The triangle symbols represent cases where $\sqrt{\mu}$ is varied by changing ρ_s and fixing $\rho_f = 1000kg/m^3$, and the inverted triangle symbols represent cases where $\sqrt{\mu}$ is varied by changing ρ_f and fixing $\rho_s = 97.13kg/m^3$ in the viscous FSI simulations. ($a = -0.218$, $x_\theta = 0.068$, and $r_\theta = 0.403$). In the dynamic divergence regions ($1 \leq \sqrt{\mu} < 2$), the decaying frequencies are expressed as the dotted arrow line.

and Castile (1951) at $\sqrt{\mu} = 1.65$ & 1.98, they did not report the flutter frequencies, as shown in Figs. 3.7 - 3.9, which may be because the system was actually in the dynamic divergence regime where the vibration frequency decay with time as the deformations increase. The results in Figs. 3.7 and 3.9 suggest that the viscous LHC

method can accurately capture the flutter onset condition for the range of relative mass ratios considered. The time domain inviscid FC method (in contrast to the linear theory results from *Woolston and Castile* (1951) obtained using a frequency domain solution method) also yielded good estimates, because it does not assume harmonic condition. It is important to note here that the time domain inviscid FC solver is able to provide a good approximation at a much lower computational cost compared to the viscous LHC method.

Figure 3.9(a) shows the nondimensional frequency ratios, ω/ω_θ^*, which is the foil vibration frequency divided by the twisting natural frequency in fluid. Fig. 3.9(b) shows the reduced frequency, k, at the flutter boundary. For almost all the cases shown in Figure 3.9, $k < 1$, the simulations show that the wake patterns consist of thin, undulating shear layers with opposite signs, as will be shown later in Figs. 3.16–3.17. Note that the system vibration frequency is zero in the static divergence range ($\sqrt{\mu} < 1$), but there are still vibrations at the dynamic divergence range ($1 \leq \sqrt{\mu} < 2$) where the mean deformations grow in time and the vibration frequency decreases toward zero as the deformation increases. The results show that in the flutter region ($\sqrt{\mu} \geq 2$), ω/ω_θ^* and k both decrease with increasing $\sqrt{\mu}$, and the flutter frequency is slightly less than the in-water natural twisting frequency, as indicated in Fig. 3.9(a).

The results in Figs. 3.7, 3.8, and 3.9 suggest that the flutter velocity and frequencies, as well as the divergence velocity predicted using the viscous LHC, are in good agreement with the measured data. The trends in Figs. 3.7 and 3.8 show that when $\sqrt{\mu} < 2$, static or dynamic divergence will occur earlier than flutter because the oscillations will be quickly damped out with higher fluid inertial and damping effects. In addition, for some cases such as those shown in Fig. 3.8, static divergence may occur at lower speeds than that predicted by linear potential theory because of viscous and nonlinear effects. Examples of such cases were reported in experimental studies in *Besch and Liu* (1971) and *Abramson and Ransleben* (1965), and shown

in Fig. 3.8, where the theoretical divergence velocity was infinite because the EA coincided with the theoretical AC (i.e., $e = 0$ in Eq.(3.3)); the predicted divergence velocity using the viscous FSI solver was finite, and agreed well with measured values, because viscous effects and flow separation modified the center of pressure (CP) from the theoretically assumed location. Nevertheless, it should be noted that the current viscous FSI solver assumes linear elastic material behavior, and does not consider the strain and/or stress limit where material failures may occur.

The results in Figs. 3.7 - 3.9 show that the governing instability mode transitions from flutter for $\sqrt{\mu} \geq 2$ to dynamic divergence for $1 \leq \sqrt{\mu} < 2$ to static divergence for $\sqrt{\mu} < 1$. Change in instability mode can be explained as follows: as the relative mass ratio decreases, the in-water natural frequencies reduce with increased fluid density; this will prolong the structural dynamic response time and increase not only the fluid inertial and damping forces, but also the fluid disturbing force, which acts to lower the effective system stiffness. Note that static divergence is a static failure which occurs when the effective system stiffness is zero, i.e. when the fluid disturbing moment is equal or higher than the solid restoring moment. On the other hand, dynamic divergence is a nonlinear dynamic instability with oscillation. As the relative mass ratio approaches zero ($\sqrt{\mu} \to 0$), the oscillation frequencies move toward zero ($\omega \to 0$) due to increasing fluid damping and fluid inertial effects coupled with decreasing system stiffness, which explains the transitions from flutter to dynamic divergence to static divergence. This also explains why the linear frequency domain (FD) method will fail in the low mass ration regime ($\sqrt{\mu} < 3$) as the motion will no longer be harmonic. Note that the results of *Woolston and Castile* (1951) for $1 \leq \sqrt{\mu} < 2$ can potentially be dynamic divergence rather than flutter because the oscillation frequencies are not shown in Fig. 3.9. Since *Woolston and Castile* (1951) measured flutter points by an oscillograph record of the model frequencies, the oscillation frequency might decay out in those regions ($1 \leq \sqrt{\mu} < 2$).

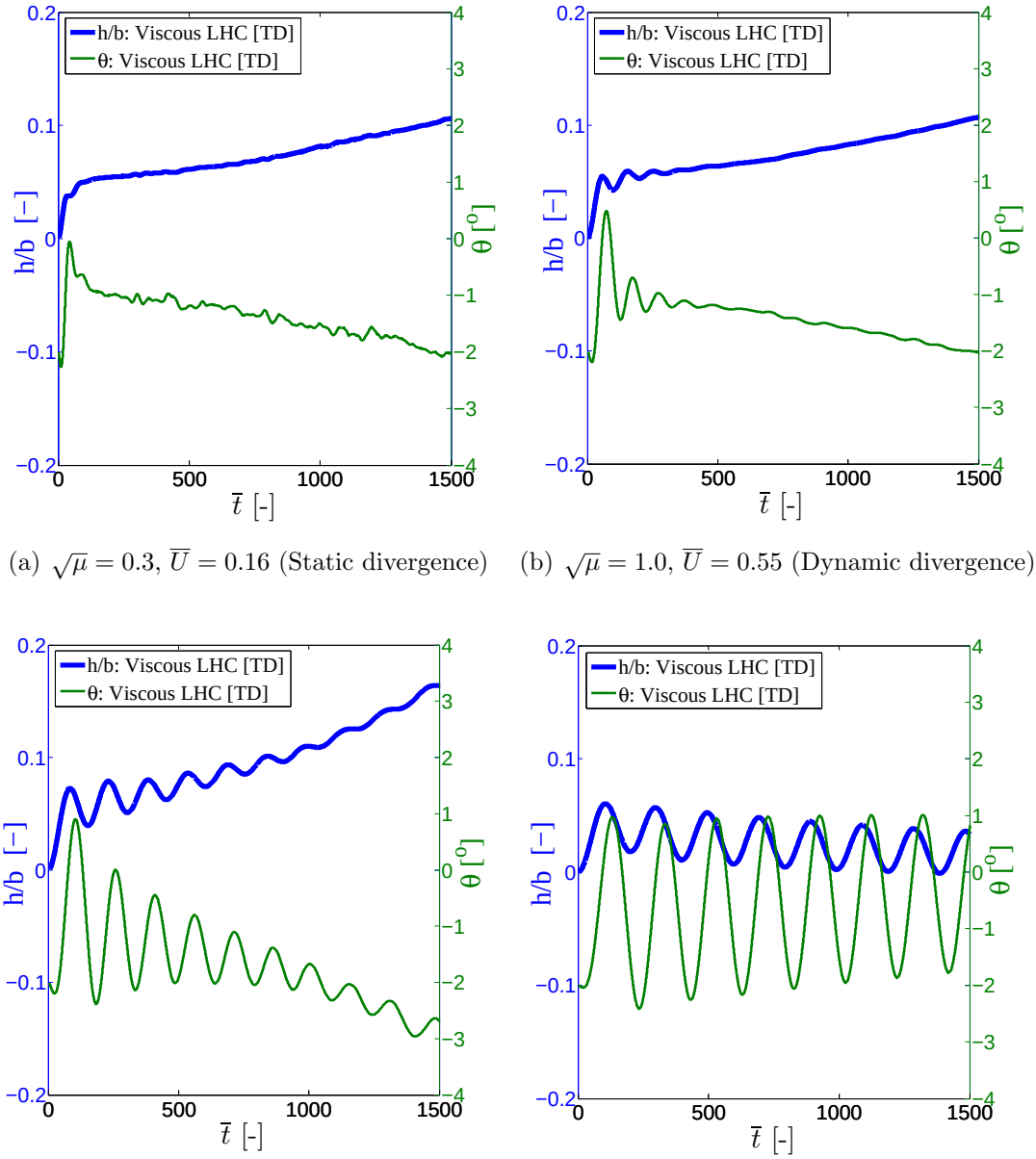

(a) $\sqrt{\mu} = 0.3$, $\overline{U} = 0.16$ (Static divergence) (b) $\sqrt{\mu} = 1.0$, $\overline{U} = 0.55$ (Dynamic divergence)

(c) $\sqrt{\mu} = 1.5$, $\overline{U} = 0.82$ (Dynamic divergence) (d) $\sqrt{\mu} = 1.98$, $\overline{U} = 1.0$ (Flutter)

Figure 3.10: Time histories of bending and twisting deformation of viscous LHC for NACA 16-010 foil at (a) $\sqrt{\mu}$=0.3, $\overline{U} = 0.16$ (Static divergence) (b) $\sqrt{\mu}$=1.0, $\overline{U} = 0.55$ (Dynamic divergence) (c) $\sqrt{\mu}$=1.5, $\overline{U} = 0.82$ (Dynamic divergence), (d) $\sqrt{\mu}$=1.98, $\overline{U} = 1.0$ (Flutter). $\overline{t} = t\omega_\theta$ is the non-dimensional time. Note that the $\sqrt{\mu}$ is varied by fixing $\rho_f = 1000kg/m^3$ corresponding to the water and varying ρ_s.

Figure 3.10 shows the predicted sample time histories for static divergence (Fig. 3.10(a)), dynamic divergence (Figs. 3.10(b),(c)), and flutter (Fig. 3.10(d)). The

results are obtained using the viscous LHC method, and by changing $\sqrt{\mu}$ by fixing ρ_f corresponding to water and varying ρ_s. As shown in Figs. 3.7, 3.8, and 3.9, linear potential theory cannot predict the proper switch-off point between divergence and flutter because there is a dynamic divergence region between flutter and static divergence for $1 \leq \sqrt{\mu} < 2$, where the mean deformation increases monotonically, and the oscillation frequency decreases as deformation increases. Note that dynamic divergence was captured by the nonlinear viscous FSI solver. Again, it should be emphasized that dynamic divergence is a nonlinear phenomenon, and cannot be predicted with linear methods that assumes small harmonic motion. Unlike static divergence, dynamic divergence depends on both solid and fluid inertia and damping force terms, in addition to the solid restoring force and fluid disturbing force terms.

Table 3.2: The influence of varying ρ_s vs. ρ_f (to change the relative mass ratio, $\sqrt{\mu}$) on the reduced static/dynamic divergence and flutter velocities. The results are predicted by the viscous LHC model.

		Varying ρ_s ($\rho_f = 1000kg/m^3$)			Varying ρ_f ($\rho_s = 97.13kg/m^3$)		
Status	$\sqrt{\mu}$	$\overline{U}$	ω/ω_θ^*	k	$\overline{U}$	ω/ω_θ^*	k
Static divergence	0.3	0.16	0.0	0.0			
	0.67	0.37	0.0	0.0			
Dynamic divergence	1.0	0.55	$1.78 \rightarrow 0.0$	$1.25 \rightarrow 0.0$	0.54	$1.37 \rightarrow 0.0$	$1.21 \rightarrow 0.0$
	1.5	0.82	$1.16 \rightarrow 0.0$	$0.81 \rightarrow 0.0$	0.82	$1.22 \rightarrow 0.0$	$0.81 \rightarrow 0.0$
	1.65	0.90	$1.11 \rightarrow 0.0$	$0.73 \rightarrow 0.0$	0.88	$1.19 \rightarrow 0.0$	$0.77 \rightarrow 0.0$
Flutter	1.98	1.00	1.13	0.70	1.02	1.09	0.66
					1.29	0.93	0.52
					1.85	0.89	0.36

Using the viscous LHC method, the influences of varying ρ_s vs. ρ_f, on the reduced static/dynamic divergence and flutter velocities are shown in Table 3.2. The static divergence (i.e., deformation $\rightarrow \infty$ and $k = 0$), dynamic divergence (i.e., mean deformation $\rightarrow \infty$ and $k \rightarrow 0$), and flutter (i.e., total damping=0 and k =constant) boundaries are distinguished for different relative mass ratios. The results in Table

3.2 show that the predicted reduced velocity ($\overline{U}$), non-dimensional frequency ratio (ω/ω_θ^*), and reduced frequency (k) are similar for cases with varying ρ_s or ρ_f.

3.3 FSI response

This section explains the detailed FSI response of the flexible foil under stable, critical, and unstable conditions at the test points shown in Fig. 3.11.

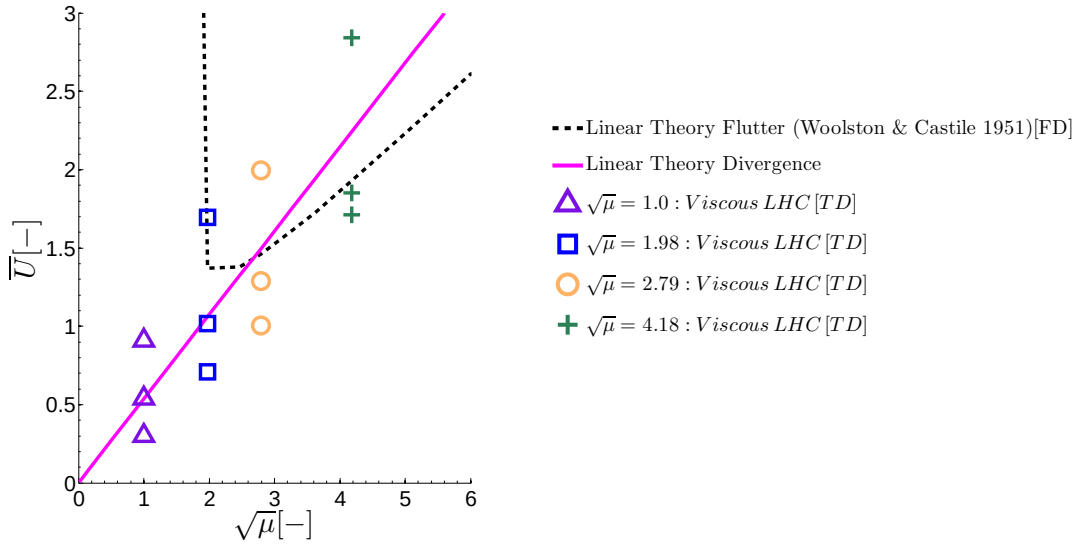

Figure 3.11: The test points used to demonstrate the detailed FSI response of flexible foils in light and dense flow conditions. Also shown are the linear theory flutter (via frequency domain solution method) and static divergence velocity boundaries. The problem set-up is similar to the experiments by *Woolston and Castile* (1951) for NACA 16-010 foil in Freon 21 and air mixtures with fixed $\rho_s = 97.13 kg/m^3$.

The predicted time-histories of the bending and twisting deformations at the test points (shown in Fig. 3.11) using the time domain (TD) inviscid FC and viscous LHC method formulation are shown in Figs. 3.12 and 3.13; the flutter velocity, U_f, shown in the labels therein corresponds to that computed by the viscous LHC method. As can be seen from Fig. 3.7, the predicted flutter velocities are somewhat different for the viscous LHC computations and the inviscid FC computations due to viscous and nonlinear FSI effects. When the inflow velocity is less than the flutter velocity

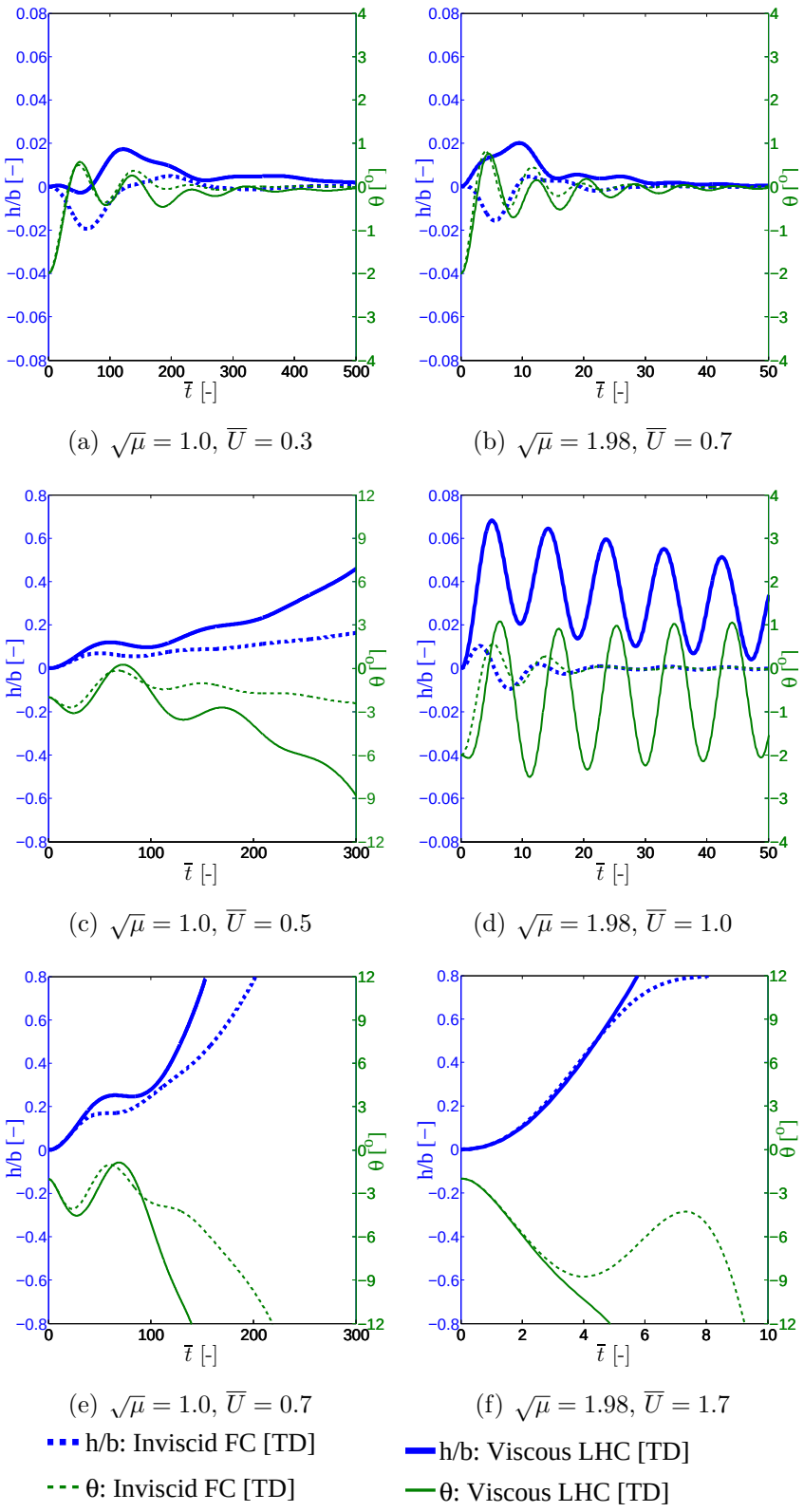

Figure 3.12: Time-histories of bending and twisting deformations for NACA16-010 foil at $\sqrt{\mu} = 1.0$ and $\sqrt{\mu} = 1.98$. $\overline{t} = t\omega_\theta$ is the non-dimensional time, $\sqrt{\mu}$ is varied by fixing $\rho_s = 97.13 kg/m^3$ corresponding to the balsa wood NACA16-010 foil used by *Woolston and Castile* (1951), but varying ρ_f.

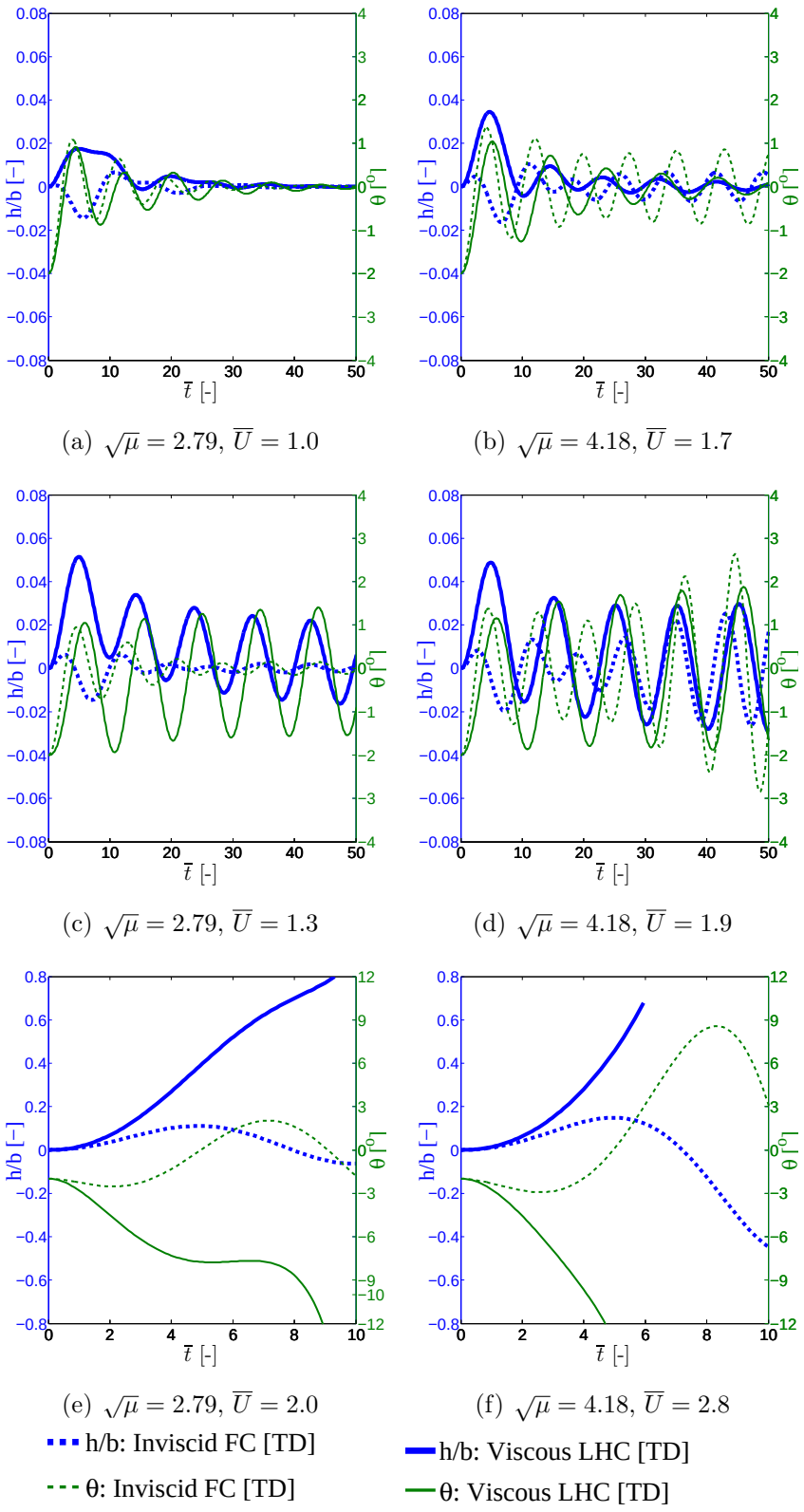

Figure 3.13: Time-histories of bending and twisting deformations for NACA16-010 foil at $\sqrt{\mu} = 2.79$ and $\sqrt{\mu} = 4.18$. $\bar{t} = t\omega_\theta$ is the non-dimensional time, $\sqrt{\mu}$ is varied by fixing $\rho_s = 97.13 kg/m^3$ corresponding to the balsa wood NACA16-010 foil used by *Woolston and Castile* (1951), but varying ρ_f.

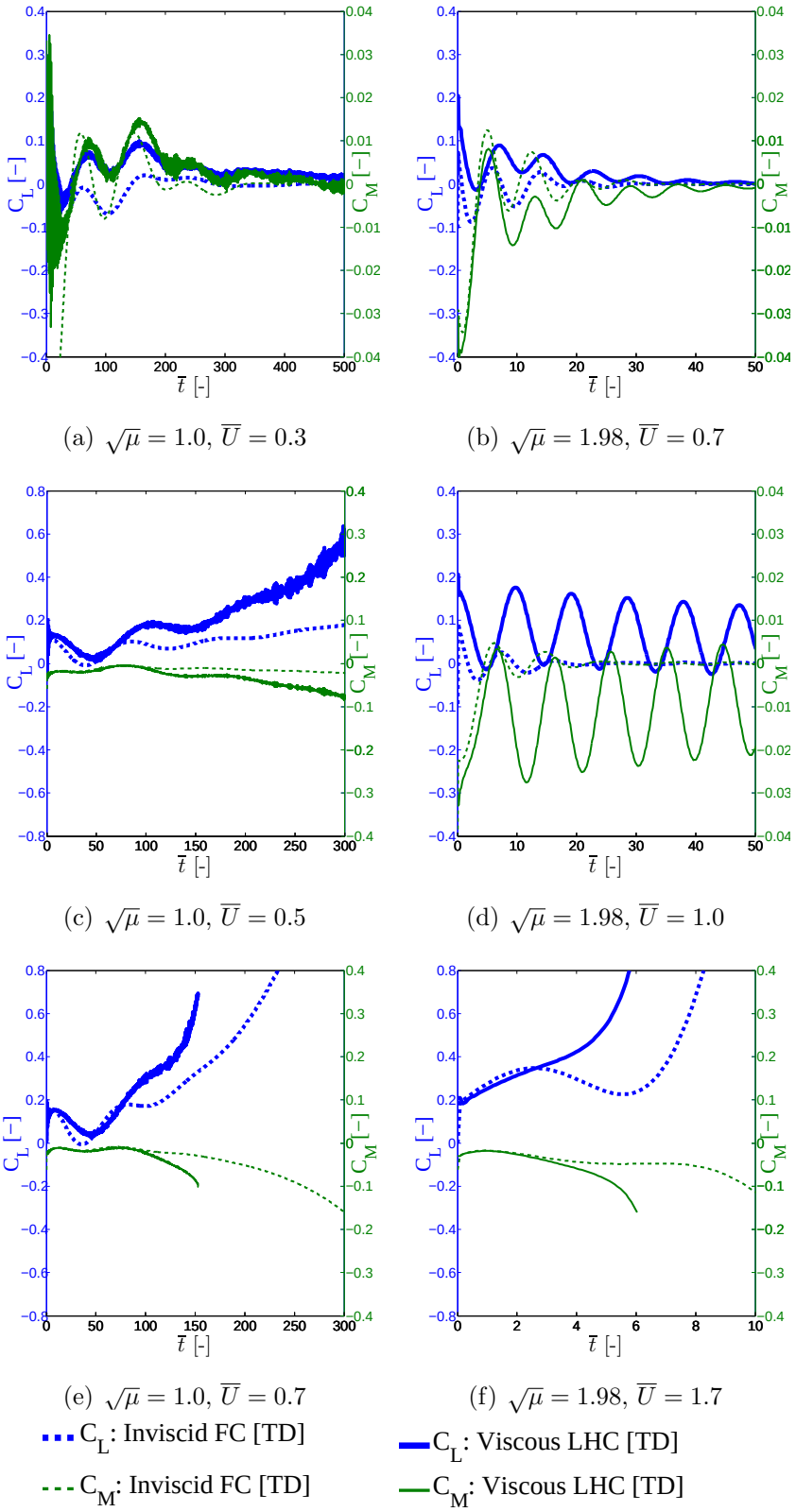

Figure 3.14: Time-histories of lift and moment coefficients for NACA16-010 foil at $\sqrt{\mu} = 1.0$ and $\sqrt{\mu} = 1.98$. $\bar{t} = t\omega_\theta$ is the non-dimensional time, $\sqrt{\mu}$ is varied by fixing $\rho_s = 97.13 kg/m^3$ corresponding to the balsa wood NACA16-010 foil used by *Woolston and Castile* (1951), but varying ρ_f.

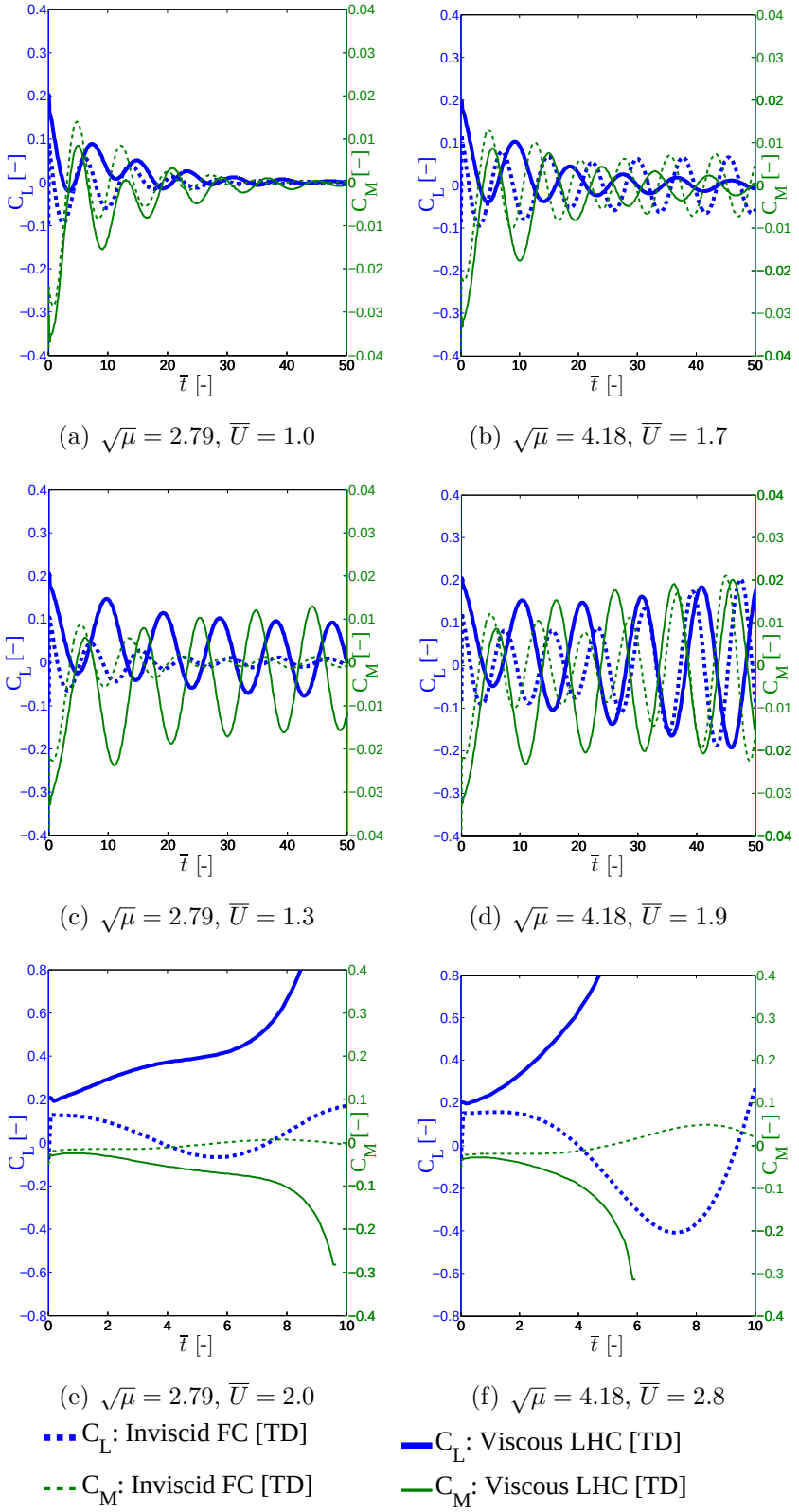

Figure 3.15: Time-histories of lift and moment coefficients for NACA16-010 foil at $\sqrt{\mu} = 2.79$ and $\sqrt{\mu} = 4.18$. $\bar{t} = t\omega_\theta$ is the non-dimensional time, $\sqrt{\mu}$ is varied by fixing $\rho_s = 97.13 kg/m^3$ corresponding to the balsa wood NACA16-010 foil used by *Woolston and Castile* (1951), but varying ρ_f.

($U < U_f$) (as in Figs. 3.12(a), (b) and 3.13(a), (b)), the foil is predicted to be stable by both the inviscid and viscous simulations, where the amplitudes of the bending and twisting vibrations decrease with time and eventually approach zero because of a net positive total damping.

When the inflow velocity is equal to the flutter velocity ($U = U_f$), the amplitudes of the bending and twisting vibrations remain the same in time due to net zero total damping; this is close to the cases shown in Figs. 3.12(d) and 3.13(c),(d) for the viscous LHC simulations. When the inflow velocity is much greater than the flutter velocity ($U > U_f$), as shown in Figs. 3.12(c), (e), (f) and 3.13(e), (f), the system becomes unstable and gets into dynamic divergence; the amplitudes of the bending and twisting vibrations increase with time because the total damping becomes negative. In addition, as shown in Fig. 3.11, the points shown in Figs. 3.12(e), (f) and 3.13(e), (f) are not only above the flutter boundary, but also the static divergence boundary, and hence are labeled as dynamic divergence since obvious fluctuations could be observed. The mean deformation increases with time, and the oscillation frequency goes toward zero as deformation increases.

As shown in Fig. 3.7, for $\sqrt{\mu} < 1$, the foil will encounter static divergence before flutter. Divergence is possible when the EA of the hydrofoil is downstream of the center of pressure (CP), and when the fluid disturbing force is equal to or exceeds the solid restoring moment. As is evident via Eq.(3.3), the critical divergence velocity decreases with increasing ρ_f and e. However, even for the case of $e = 0$, where the EA coincides with the aerodynamic center (AC), divergence may still occur, as shown in *Besch and Liu* (1971) and our viscous FSI prediction shown in Fig. 3.8, because viscous effects and flow separation cause the CP to move from the AC. Also note that for $\sqrt{\mu} < 3$, where the viscous forces are relatively more important, the results shown in Figs. 3.12 and 3.13 suggest that viscous effects may not delay flutter. In this regime, as shown in Figs. 3.12 and 3.13(a), (c), and (e), the magnitudes of the

bending and twisting deformations obtained using the viscous LHC simulations are greater and have a slower rate of decay than the inviscid FC simulations, due to the nonlinear viscous FSI effect caused by the higher fluid density. Consequently, the predicted flutter velocity using the viscous LHC simulations is lower than the inviscid FC simulations, as will be shown later in Fig. 3.18. However, for $\sqrt{\mu} > 3$, the results in Fig. 3.7 show that viscous effects help to delay flutter. For instance, the inviscid FC simulations predict a lower flutter velocity than the viscous LHC simulations, which is evident by the increasing deformation amplitudes with time predicted by the inviscid FC method in Fig. 3.13(d), i.e. $U > U_f$, while the viscous LHC method shows approximately constant displacement amplitude in time.

The time-histories of the lift coefficient (C_L) and moment coefficient (C_M) for various relative mass ratios for the system under stable, critical, and unstable conditions are shown in Figs. 3.14 and 3.15. Note that the lift coefficients follow the same trend with the bending deformations; similarly, the moment coefficients (defined as positive counterclockwise about the EA) follow the same trend with the twisting deformations. It should be noted in Fig. 3.14 that for all the cases except Fig. 3.14(a), the results are obtained using $\Delta t = 4 \times 10^{-4}$ s. For case shown in Fig. 3.14 (a) $\Delta t = 8 \times 10^{-4}$ s is used in order to avoid numerical noises due to the relatively large period. For $\sqrt{\mu} \leq 1$, the C_L and C_M predictions obtained using the viscous LHC simulations show high frequency noise introduced by the very small time-step size compared to the large natural period. The large natural period is a result of the higher added mass with higher ρ_f. To avoid this artificial noise due to numerical errors, the simulation shown in Fig. 3.14(a) for the lift and moment coefficients with $\overline{U} = 0.3$ and $\sqrt{\mu} = 1.0$ was obtained using $\Delta t = 8 \times 10^{-4}$ s.

Figure 3.16 illustrates the predicted time-history of the bending and twisting deformations along with selected snapshots of the predicted streamlines and vorticity contours obtained from the viscous LHC simulations for a hydrofoil at its critical

flutter velocity of $\overline{U} = 1.0$ for $\sqrt{\mu} = 1.98$, for the balsa wood NACA16-010 foil used by *Woolston and Castile* (1951). The heavy black horizontal lines on the vorticity contour plot indicate the undeformed vertical position of the hydrofoil trailing edge (TE). The deformations are relatively small because of the relatively high stiffness of the model-scale foil. Nevertheless, the foil is observed to undergo near constant amplitude oscillations in plunge and pitch at the flutter velocity, as illustrated in Fig. 3.16.

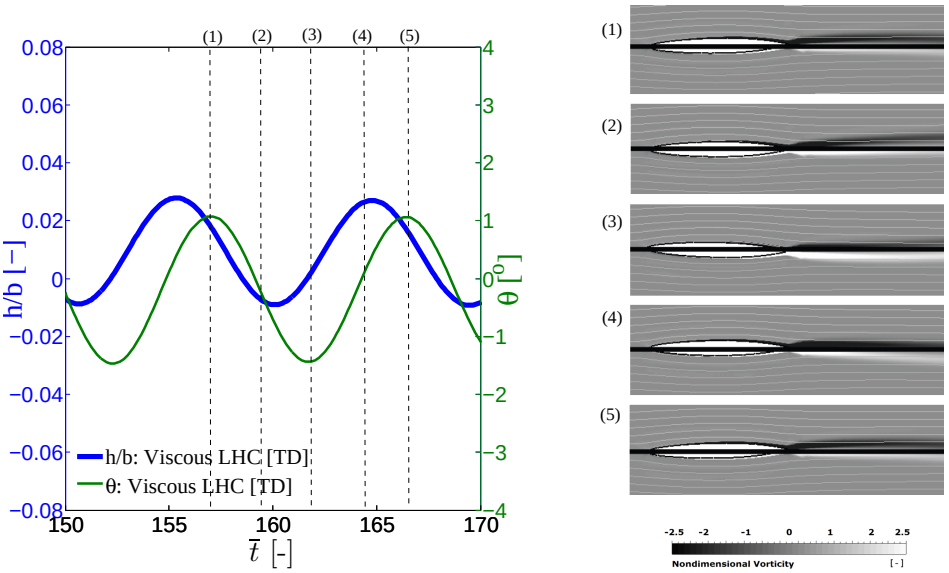

Figure 3.16: (Left) Time-histories of the bending and twisting deformation and (Right) the predicted vorticity contour with sample streamlines, for the balsa wood NACA16-010 foil used by *Woolston and Castile* (1951) at its flutter velocity ($\overline{U} = 1.0$) with $\sqrt{\mu} = 1.98$ ($\rho_f = 2.21 kg/m^3$ and $\rho_s = 97.13 kg/m^3$) and Re=1.94×10^6. $\bar{t} = t\omega_\theta$ is the non-dimensional time. The heavy black horizontal lines on the non-dimensional vorticity ($\varpi = \omega b/U$) contour plot indicate the initial vertical position of the foil trailing-edge.

Similarly, Fig. 3.17 shows the predicted deformation time-histories and corresponding snapshots of the streamline and vorticity contours for a hydrofoil at the divergence velocity for $\sqrt{\mu} = 1.98$ with $\overline{U} = 1.7$. Since $\overline{U} = 1.7$ corresponds to the divergence velocity, the amplitudes of both the bending and twisting motion increase monotonically with time.

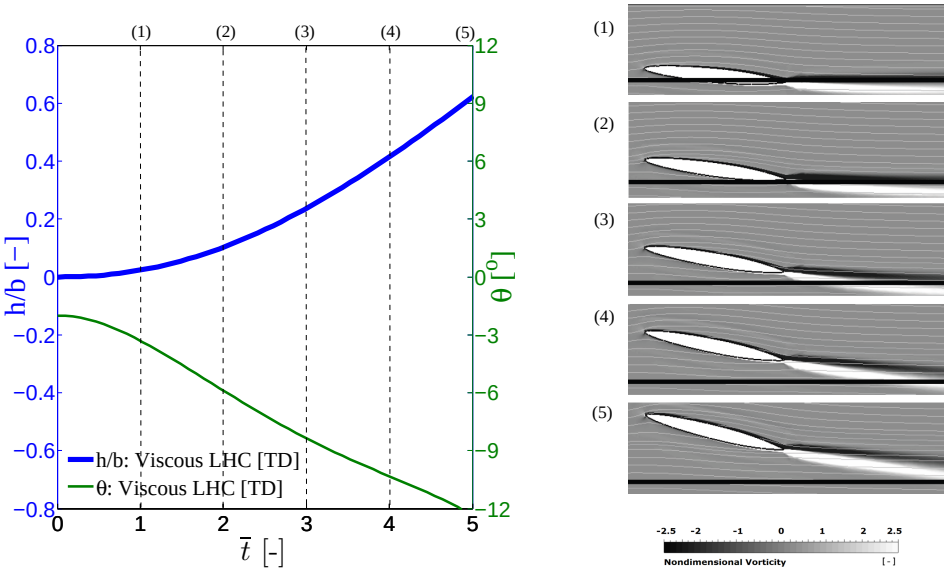

Figure 3.17: (Left) Time-histories of the bending and twisting deformation and (Right) the predicted vorticity contour with sample streamlines, for the balsa wood NACA16-010 foil used by *Woolston and Castile* (1951) at its divergence velocity ($\overline{U} = 1.7$) with $\sqrt{\mu} = 1.98$ ($\rho_f = 2.21 kg/m^3$ and $\rho_s = 97.13 kg/m^3$) and Re=3.24×10^6. $\overline{t} = t\omega_\theta$ is the non-dimensional time. The heavy black horizontal lines on the non-dimensional vorticity ($\varpi = \omega b/U$) contour plot indicate the initial vertical position of the foil trailing-edge.

Note that the vorticity contours in Figs. 3.16 and 3.17 show consistent thin trailing wake sheets; this is because $k < 1$, which is consistent with the wake patterns reported in *Munch et al.* (2010).

3.4 Total damping coefficient and vibration frequency

In this study, the flutter boundary is determined as the critical speeds when the total bending (or twisting) damping coefficient, $\zeta_{T,h}$ (or $\zeta_{T,\theta}$), is projected to be zero. To illustrate this process, the predicted total bending and twisting damping coefficients, $\zeta_{T,h}$ and $\zeta_{T,\theta}$, as a function of the reduced velocity ($\overline{U}$) are shown in Fig. 3.18 along with the measured flutter velocity values reported by *Woolston and Castile* (1951).

As noted earlier, when $\zeta_T > 0$, the deformations will decrease with time, so the

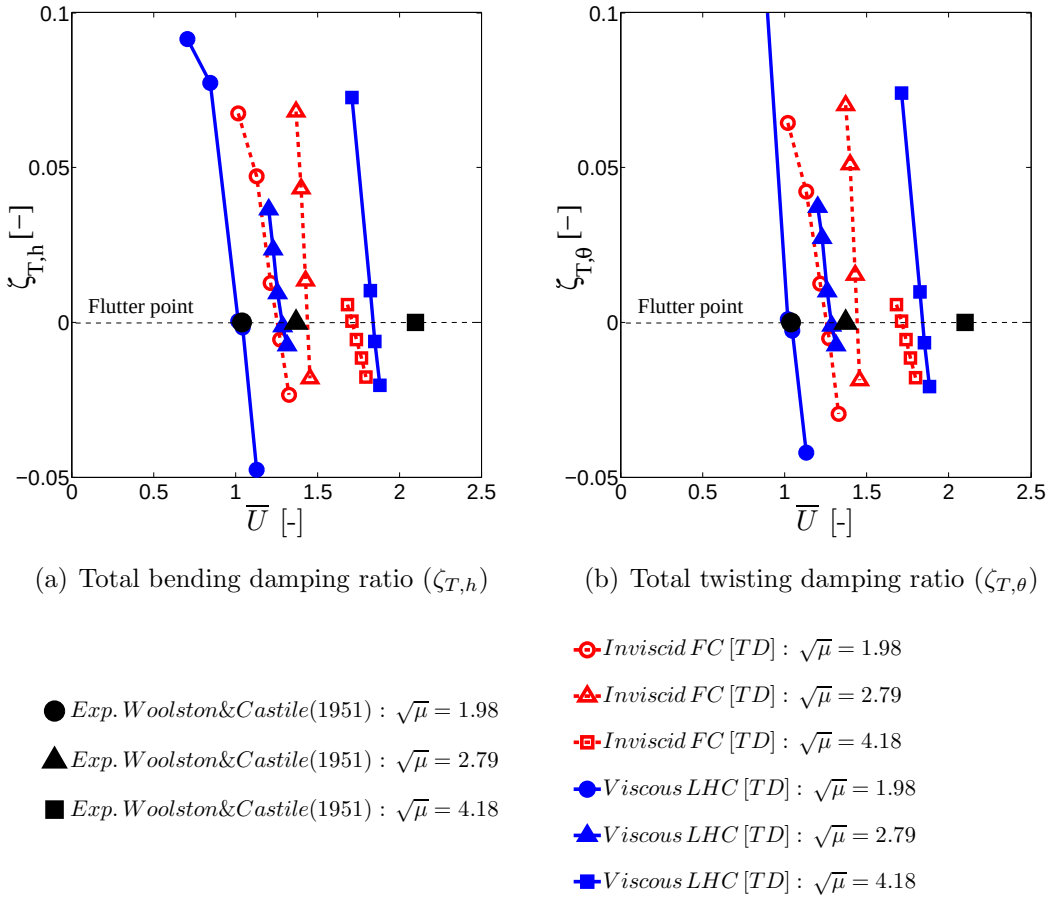

(a) Total bending damping ratio ($\zeta_{T,h}$)

(b) Total twisting damping ratio ($\zeta_{T,\theta}$)

Figure 3.18: (a) Total bending damping ratio ($\zeta_{T,h}$) and (b) total twisting damping ratio ($\zeta_{T,\theta}$) as function of the reduced velocity ($\overline{U}$) at different relative mass ratios $\sqrt{\mu}$. In this plot, $\sqrt{\mu}$ is varied by fixing ρ_s of 97.13 kg/m^3 corresponding to the balsa wood NACA16-010 foil used by *Woolston and Castile* (1951), but varying ρ_f. The filled symbols correspond to the experimental measurements, the dashed lines with open symbols correspond to inviscid FC simulations, and the solid lines with open symbols correspond to viscous LHC simulations.

system is stable. When $\zeta_T < 0$, the deformations will increase with time, so the system is unstable. The flutter velocities reported in Fig. 3.7 correspond to the projected critical speed in Fig. 3.18 at which either $\zeta_{T,h} = 0$ or $\zeta_{T,\theta} = 0$, whichever is earlier, although the two values are very close.

As shown in Fig. 3.18, the flutter velocity predicted by the viscous LHC method is higher than the velocities predicted by the inviscid FC method for $\sqrt{\mu} > 3$, but the opposite is true for $\sqrt{\mu} < 3$. Moreover, for all the cases shown, the flutter veloci-

ties predicted by the viscous LHC method are closer to the experimentally measured values than those predicted by the inviscid FC method. It should be noted that the current inviscid and viscous simulations assume the structural damping coefficients, $\zeta_{s,h}$ and $\zeta_{s,\theta}$, to be zero (for simplicity), which contribute to the slight under prediction of the flutter velocities predicted by the viscous LHC method compared to the experimentally measured values.

Figure 3.19 shows the predicted system bending and twisting vibration frequencies ($\overline{f_h} = f_{h,LHC}/f_\theta$ and $\overline{f} = f_{\theta,LHC}/f_\theta$) as a function of the reduced velocity ($\overline{U}$) for three different relative mass ratios. The predictions shown there are obtained using the viscous LHC method. It should be noted that results for the $\sqrt{\mu} = 1$ case are not shown in Fig. 3.19, because in that case divergence occurred prior to flutter. Note that although the measured flutter velocities were reported for multiple cases, the measured flutter frequency was only reported for the $\sqrt{\mu} = 4.18$ case in *Woolston and Castile* (1951). Additional comparisons of the predicted and measured non-dimensional flutter frequencies are shown in Fig. 3.9, which have different $\sqrt{\mu}$ values than the ones shown here. The results show that the viscous LHC simulations are in good agreement with the measured values.

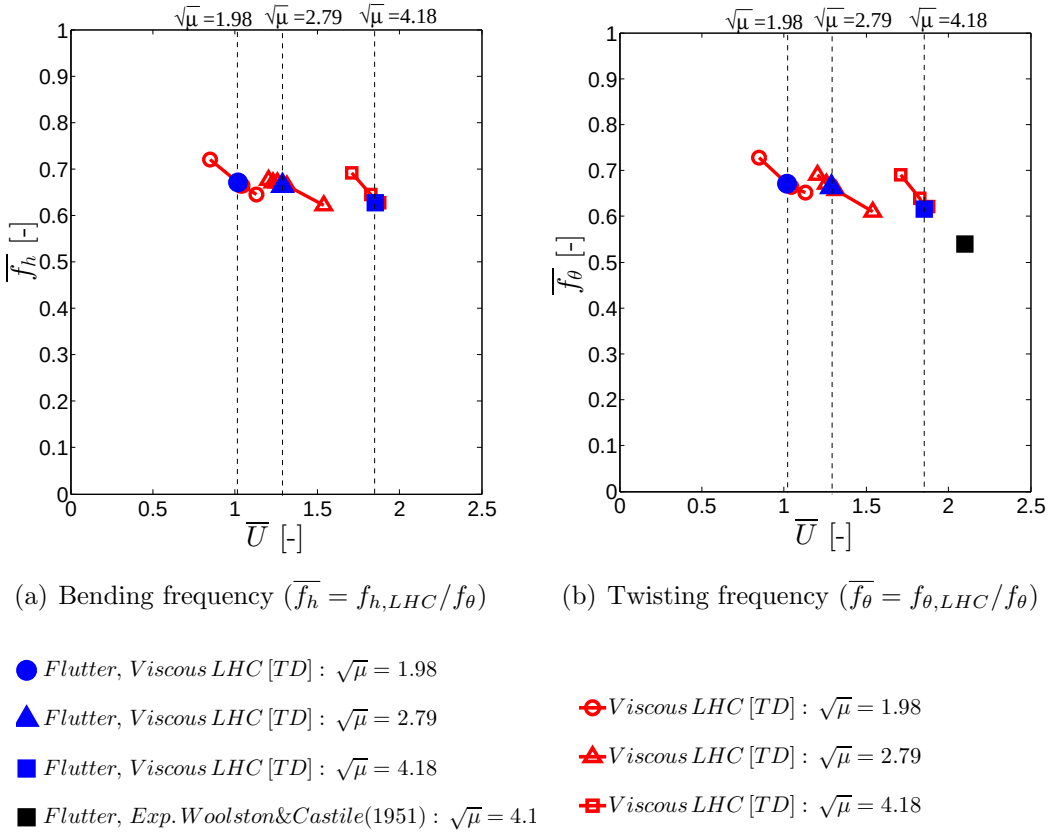

(a) Bending frequency ($\overline{f_h} = f_{h,LHC}/f_\theta$)

(b) Twisting frequency ($\overline{f_\theta} = f_{\theta,LHC}/f_\theta$)

Figure 3.19: Non-dimensional (a) bending frequency ($\overline{f_h} = f_{h,LHC}/f_\theta$) and (b) twisting frequency ($\overline{f} = f_{\theta,LHC}/f_\theta$) for NACA16-010 foil at different relative mass ratios ($\sqrt{\mu}$) as function of the reduced velocity ($\overline{U}$) at the various simulation points shown in Fig. 3.11. $\sqrt{\mu}$ is varied by fixing ρ_s of 97.13 kg/m^3 corresponding to the balsa wood NACA16-010 foil used by *Woolston and Castile* (1951) but varying ρ_f. Also shown are the measured flutter velocity (as shown by the vertical dot lines) and frequency (black filled square) from *Woolston and Castile* (1951). The experimental frequencies for different $\sqrt{\mu}$ are also shown in Fig. 3.9. The predicted system bending and twisting vibration frequencies ($f_{h,LHC}$ and $f_{\theta,LHC}$) from the viscous LHC method are noted by the open symbols. The predicted flutter bending and twisting frequencies are noted by the filled symbols.

CHAPTER IV

Flow-induced vibrations

As stated earlier, the fluid-structure interaction responses of a hydrofoil become more important with higher fluid loads. Hence, the results presented below demonstrate the flow-induced vibration response of a cantilevered flexible NACA0015 polyacetate (POM) hydrofoil. Section 4.1 presents the NACA0015 model setup of both the numerical and experimental simulations for the flow-induced vibration response. Section 4.2 and Section 4.3 present the influence of the reduced velocity and angle of attack, respectively, on the flow-induced vibration of the flexible NACA0015 hydrofoil. The times histories of bending and twisting deformations, total loss factors, wake structures, and vortex shedding frequencies of the flexible hydrofoil are shown in this section to explain the flow-induced vibrations. To reduce clutter in the graphs, only viscous FSI results are shown in this chapter and the predictions are compared with experimental measurements from the French Naval Academy Research Institute (IRENav).

4.1 NACA0015 model setup

Numerical simulations are performed on a cantilevered flexible NACA0015 polyacetate (POM) hydrofoil, where the key geometric, fluid, and material parameters are listed on the right most column in Table 4.1. The chord length (c) is 0.1 m and a

span length (s) is 0.192 m. To examine the trend of the in-water damping characteristic of flexible hydrofoils with varying μ and $\overline{U}$, current experimental and numerical viscous FSI models are compared with published experimental measurements (*Blake and Maga*, 1975; *Reese*, 2010) and the inviscid theory (*Blake and Maga*, 1975). Table 4.1 shows a comparison of the key parameters for the current POM NACA0015 foil with the hydrofoils tested by *Blake and Maga* (1975) and by *Reese* (2010). Note that the current NACA0015 hydrofoil has a much lower relative mass ratio ($\sqrt{\mu}$) and a much higher reduced velocity ($\overline{U}$) because of the lower density and elastic modulus of POM compared to the stainless steel hydrofoil used in *Blake and Maga* (1975) and the aluminum hydrofoil used in *Reese* (2010).

Table 4.1: Experimental and numerical parameters of the current POM NACA0015 hydrofoil, as well as the stainless steel and aluminum hydrofoils tested by *Blake and Maga* (1975) and *Reese* (2010), respectively.

Model	Blake & Maga(1975) Exp.	Reese(2010) Exp.	Current Exp.& Num.
Material	Stainless Steel	Aluminum	POM
Foil shape	Bullet	NACA66	NACA0015
$\sqrt{\mu}$ [-]	0.82	0.47	0.44
α_o [deg]	0	-4, 0, 4, 10	2, 8, 15, 20
Re [-]	$1 \times 10^5 \sim 5 \times 10^5$	$5.6 \times 10^4 \sim 5.6 \times 10^5$	$3 \times 10^5 \sim 12 \times 10^5$
$\overline{U}$ [-]	$0.007 \sim 0.04$	$0.004 \sim 0.04$	$0.02 \sim 0.1$
a [-]	0	0	0
x_θ [-]	N/A	N/A	-0.16
r_θ [-]	N/A	N/A	0.44
AR [–]	7.26	2	1.92
s [m]	0.508	0.1	0.192
c [m]	0.07	0.05	0.1
$\zeta_{s,h}$ [%]	0.1 (assumed)	0.2 (assumed)	2 (assumed)
$\zeta_{s,\theta}$ [%]	0.1 (assumed)	0.2 (assumed)	2 (assumed)
f_h [Hz]	114	319	81
f_θ [Hz]	897	1549	390
f_h^* [Hz]	79	163	$33 \sim 37$
f_θ^* [Hz]	678	869	$182 \sim 202$

4.1.1 NACA0015 mesh setup

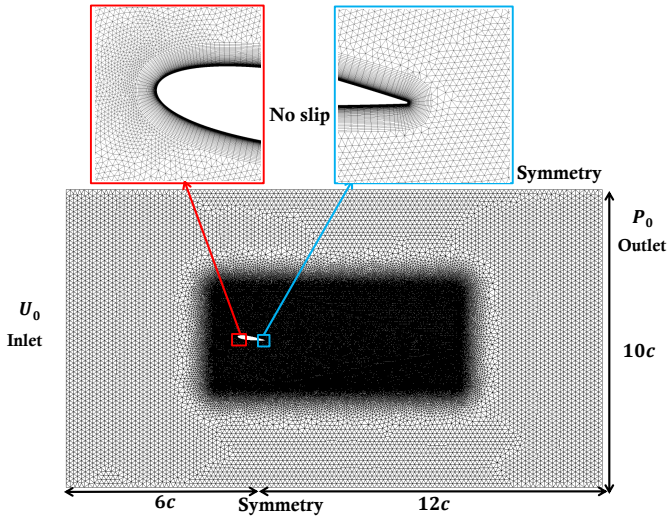

Figure 4.1: NACA0015 CFD (medium) mesh with 4.8×10^5 nodes and 9.1×10^5 elements and prescribed boundary conditions.

The NACA0015 CFD mesh is shown in Fig. 4.1. An unstructured mesh is used everywhere, apart from the hydrofoil surface. A structured boundary layer mesh is used near the foil surface, which satisfied $y^+ \approx 1$. To capture the flow details, the mesh is refined near the foil's leading-edge (LE), trailing-edge (TE), and the wake region. The boundary conditions of the CFD mesh domain are:

- uniform inlet boundary condition with 3% turbulence intensity at the left edge of the domain,
- prescribed pressure boundary condition at the right edge of the domain,
- symmetry boundary conditions at the top and bottom edges, and
- no-slip and no penetration boundary conditions at the foil interface.

Numerical viscous simulations are only performed for the NACA0015 POM hydrofoil. At each time-step, the mesh elements are deformed to conform to the hydrofoil geometry according to the foil motions obtained by using the viscous loose hybrid

coupled (LHC) method. (Readers should refer to *ANSYS-CFX* (2011) for details about the mesh deformation algorithm.) The numerical simulations of the flexible hydrofoil are initialized from the steady-state solution of flow around a stationary hydrofoil. All the CFD simulations assume the flow to be fully turbulent and are performed at $Re = 3 \times 10^5 \sim 1.2 \times 10^6$ and $\overline{U} = 0.02 \sim 0.1$ (by varying the inflow velocity, U) with geometric angles of attack (α_o) of 2°, 8°, 15°, and 20° with zero initial twisting and bending deformations.

4.1.2 Numerical mesh and time step size convergence studies for the NACA0015 POM hydrofoil

Numerical mesh and time step size convergence studies were conducted for the flexible NACA0015 POM hydrofoil at $\alpha_o = 8^o$, $\overline{U} = 0.05$, and $Re = 6 \times 10^5$.

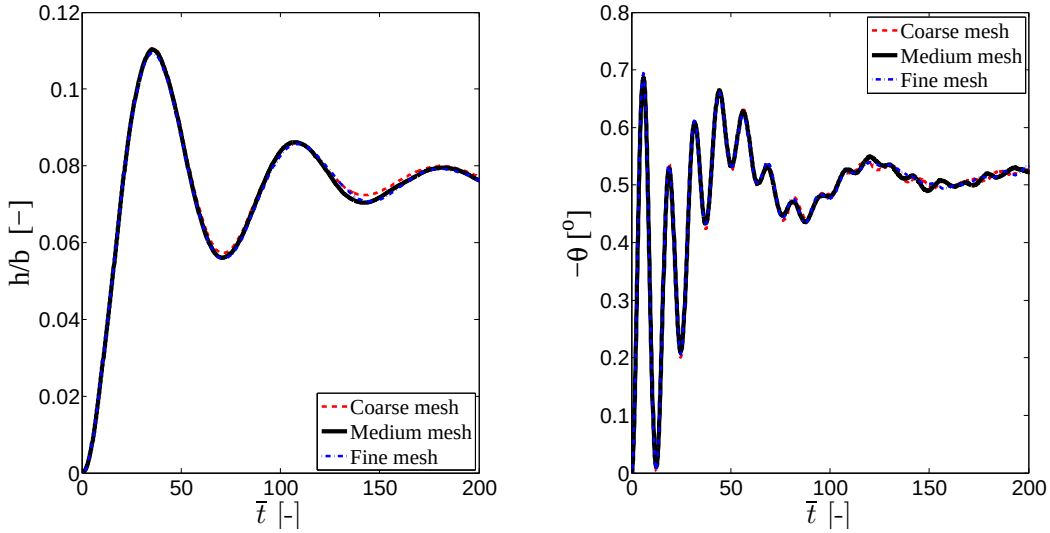

(a) Bending deformations (h/b) (b) Twisting deformations (θ)

Figure 4.2: Mesh convergence study of (a) bending deformations and (b) twisting deformations for the flexible NACA0015 POM hydrofoil at $\Delta t = T_h^*/480$ with $\alpha_o = 8^o$, $\sqrt{\mu} = 0.44$, $\overline{U} = 0.05$, and $Re = 6 \times 10^5$. Note that "coarse mesh" has 2.9×10^5 nodes and 2.7×10^5 elements, "medium mesh" has 4.8×10^5 nodes and 9.1×10^5 elements, and "fine mesh" has 9.2×10^5 nodes and 18.2×10^5 elements. $T_h^* = 1/f_h^*$ is the first in-water natural bending period of the flexible hydrofoil and $\bar{t} = t\omega_\theta$ is the non-dimensional time.

For the mesh convergence study, Fig. 4.2 compares the predicted time-histories of the bending and twisting deformations of the hydrofoil at $\Delta t = T_h^*/480$ with three different mesh sizes (i.e., "coarse mesh": 2.9×10^5 nodes and 2.7×10^5 elements, "medium mesh": 4.8×10^5 nodes and 9.1×10^5 elements, and "fine mesh": 9.2×10^5 nodes and 18.2×10^5 elements). Note that $T_h^* = 1/f_h^*$ is the first in-water natural bending period of the flexible hydrofoil and $\bar{t} = t\omega_\theta$ is the non-dimensional time. The results in Fig. 4.2 show that the predicted time-histories of the bending and twisting deformations with the medium mesh were sufficiently close to the predictions evaluated with the fine mesh. Therefore, the medium mesh was used to calculate the viscous FSI responses for the results shown in the rest of this thesis.

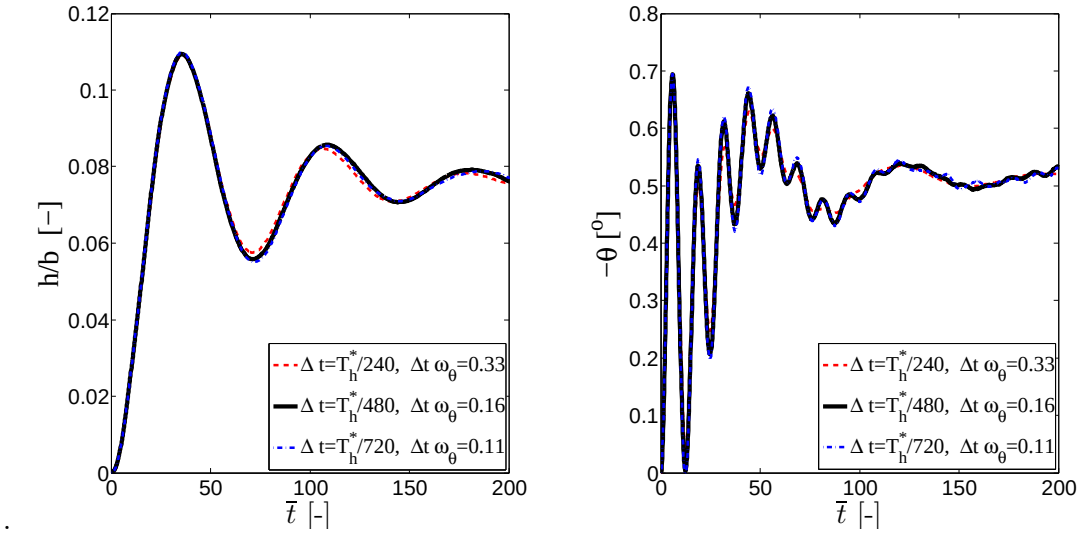

(a) Bending deformations (h/b) (b) Twisting deformations (θ)

Figure 4.3: Time step size convergence study of (a) bending deformations and (b) twisting deformations for the flexible NACA0015 POM hydrofoil on the "medium mesh" (4.8×10^5 nodes and 9.1×10^5 elements) with $\alpha_o = 8^o$, $\sqrt{\mu} = 0.44$, $\overline{U} = 0.05$, and $Re = 6 \times 10^5$. Note that $T_h^* = 1/f_h^*$ is the first in-water natural bending period of the flexible hydrofoil and $\bar{t} = t\omega_\theta$ is the non-dimensional time.

For the time step size convergence study, Fig. 4.3 compares the predicted time-histories of the bending and twisting deformations of the hydrofoil with three different time-step sizes, $\Delta t = T_h^*/240$, $T_h^*/480$, and $T_h^*/720$, (i.e., $\overline{\Delta t} = \Delta t\omega_\theta$=0.33, 0.16, and 0.11, for a flexible hydrofoil with the "medium mesh" with $\alpha_o = 8^o$, $\overline{U} = 0.05$, and

$Re = 6 \times 10^5$). Note in Fig. 4.3 that the predictions obtained using the two smallest time-steps were consistent. Consequently, all the simulations shown next used a time-step size of $\Delta t = T_h^*/480$. Comparisons of the numerical predictions and experimental measurements will be shown later in sections 4.2 and 4.3.

4.1.3 Experimental model for the NACA0015 POM hydrofoil

Experimental measurements were carried out in a recirculation cavitation tunnel at the French Naval Academy Research Institute (IRENav). The test section was 1 m long and had a 0.192 $m\times$ 0.192 m square section, as shown in Fig. 4.4(a).

The facility provided regulated velocities ranging from 2 m/s to 12 m/s, and regulated pressures from 30 mbar to 3 bars. The tunnel turbulence intensity measured by Laser Doppler Velocimetry (LDV) at the center of the test-section was 2%. A flexible, cantilevered, rectangular hydrofoil with a NACA0015 section geometry with a chord of c=0.1 m and a span of s=0.192 m was used. The hydrofoil was made of POM, with an elasticity modulus of E_s=3×10^9 Pa, Poisson's ratio of ν_s= 0.35, and solid density of ρ_s=1420 kg/m^3.

The foil was clamped at its root onto a steel cylinder, while its tip section was free, with a clearance of 1 mm between the free tip and the vertical wall, which could induce secondary flow at the large angle of incidence. Notice that the small clearance was used to minimize tip loss so the hydrodynamic response is approximately two-dimensional (2D). As shown in Fig. 4.4(b), the foil was mounted horizontally in the tunnel test section and was connected to an electric drive to change its undeformed angle of attack (α_o) according to a prescribed value. The rotation center, elastic axis (EA), was at the mid-chord.

Structural vibrations were measured using two Polytec ® LDVs: PSV-400 for scanning and PDV-100 for reference, using a class II HeNe laser of wavelength of 633 nm as shown in Figs. 4.4(b) and 4.4(c). The first laser measured the vibration

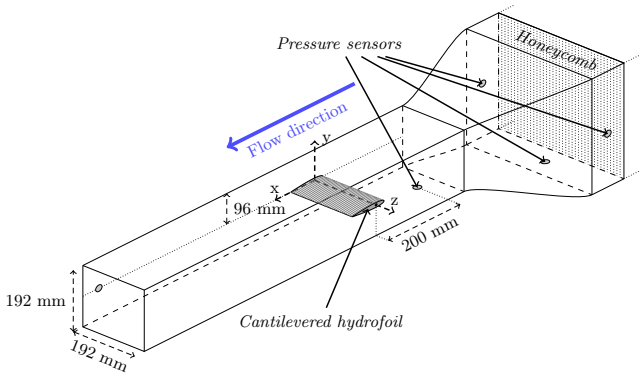

(a) Hydrodynamic cavitation tunnel

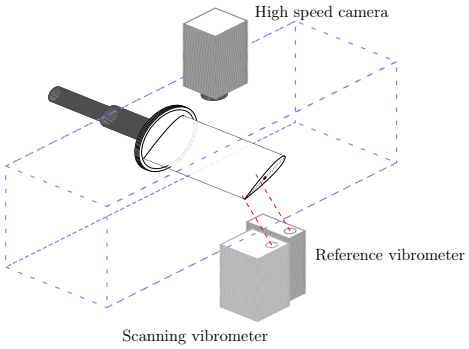

(b) Foil mounting and Laser Doppler Velocimetry (LDV) setup

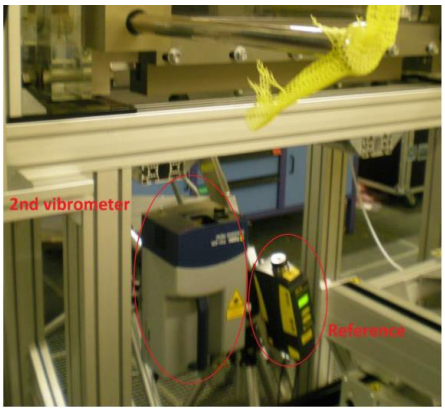

(c) Photo of the two Laser Doppler Velocimetries (LDV)

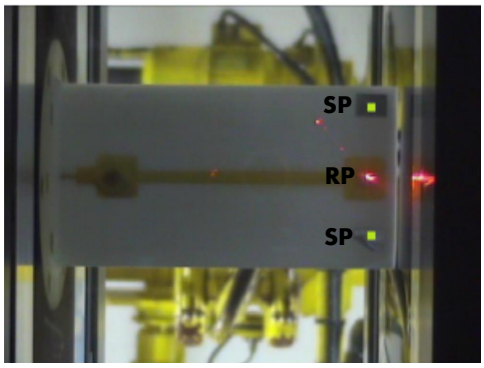

(d) Scanned measurement point (SP) and fixed reference point (RP) near the free end of the hydrofoil

Figure 4.4: The French Naval Academy Research Institute (IRENav) experimental setup: (a) cantilevered hydrofoil inside the cavitation tunnel, (b) foil mounting and Laser Doppler Velocimetry (LDV) setup, (c) photo of the two Laser Doppler Velocimetries (LDV) setup, and (d) pressure side (bottom) view of the cantilevered NACA0015 POM hydrofoil: the hydrofoil is fixed on the left end, and free on the right end, where there is a $1mm$ gap between the foil tip and the tunnel wall; flow goes from bottom to top. Also shown are the scanned measurement points (SP) and fixed reference point (RP) near the free end of the hydrofoil.

velocity on a reference point (RP), which was set at the mid-chord near the free end of the hydrofoil as shown by the red dot in Fig. 4.4(d). The second laser was equipped with a scanning system based on mirror motions, which could provide sequential vibration measurements over a user-defined predefined grid, as demonstrated via the green dots in Fig. 4.4(d). The measurements were optimized for a horizontal plane

surface subjected to vertical vibrations; the vibration velocities were captured with sensitivities ranging from 10 to 1000 $mm/s/V$. The system provided the Fourier transform of the vibration velocity signal for each measurement point for frequencies up to 40 kHz. The resultant velocity spectra were averaged using a user-defined number of acquisitions; specifically, the results shown in this work were computed by averaging 512 acquisitions per each measurement point. The frequency resolution for vibration measurements was Δf=0.625 Hz. The phase information (throughout the scan between the two measurement points) was preserved by utilizing the other reference velocimetry laser. The two laser setup made it possible to retrieve the deflection shape at a given frequency, and therefore to identify the natural frequencies of the structure and the corresponding vibration mode shapes. In order to focus on the first bending and twisting modes, two points were selected in the vicinity of the free foil tip, one close to the leading edge and one close to the trailing-edge (TE), while the reference measurement point was at the foil mid-chord near the free end of the hydrofoil, as shown in Fig. 4.4(d). These points were covered with reflective patches to avoid any light-absorption effects due to the hydrofoil material and to improve the signal to noise ratio. The hydrofoil vibrations were measured on the foil pressure side through the transparent bottom wall of the tunnel test section, while the velocimetry scanning head was held fixed to the ground.

Several measurements were carried out. The first set of measurements were conducted by measuring the mean spectral response of the foil subject to a series of impulses generated by an electrodynamic shaker both in-air and in-still-water (i.e., U= 0 m/s), which are shown in Fig. 4.5.

In Fig. 4.5, the first mode corresponds to primarily bending (f_h, f_h^*), and the second mode corresponds to primarily twisting (f_θ, f_θ^*). The third mode corresponds to the second bending natural frequency ($f_{h,2}$, $f_{h,2}^*$). According to the measurements, the first in-air natural bending and twisting frequencies were $f_h = 81$ Hz and $f_\theta = 390$

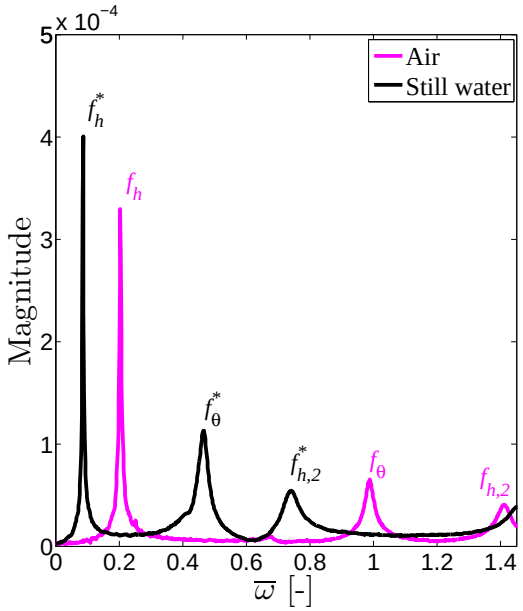

Figure 4.5: The French Naval Academy Research Institute (IRENav) experimental vibration frequency response of the NACA0015 POM hydrofoil for shock impulses in-air and in-still-water. Note that f_h, f_θ, $f_{h,2}$ are the first in-air natural bending frequency, the first in-air natural twisting frequency, and the second in-air natural bending frequency, receptively. f_h^*, f_θ^*, and $f_{h,2}^*$ are the first in-water natural bending frequency, the first in-water natural twisting frequency, and the second in-water natural bending frequency, receptively. $\overline{\omega} = \omega/\omega_\theta$ is the non-dimensional frequency.

Hz; the first in-still-water natural bending and twisting frequencies were $f_h^* = 34$ Hz and $f_\theta^* = 184$ Hz. It should be noted that during experiments, small disparities could occur on the measured frequencies due the repeatability of the assembly and disassembly of the mechanical mounting system sustaining the hydrofoil. Based on repeated measurements under the same conditions, the uncertainty in the frequency measurement was approximately 2%. The experimental series consisted of measuring the vibration response of the foil subject to various flow velocities and different angles of attack ($\overline{U} = 0.02$, 0.03, 0.04, 0.05; $Re = 3, 4, 5, 6 \times 10^5$; α_o= 0, 2, 4, 6, 8^o).

Examples of the variation of the frequency spectra with varying inflow velocities at $\alpha_o = 8^o$ and varying angles of attack at $\overline{U} = 0.05$ are shown in Fig. 4.6. In general, the amplitude of the frequency spectra increased with increasing flow velocity. It should be noted that the in-still-water vibration response ($\overline{U} = 0$) in Fig. 4.6 is scaled down,

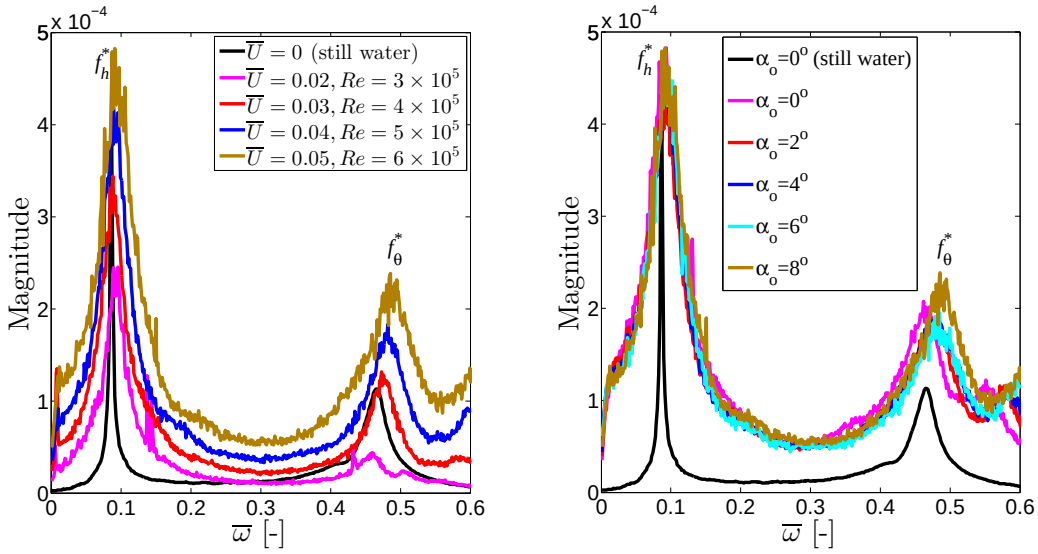

(a) Varying inflow velocity at $\alpha_o = 8^o$ (b) Varying angle of attack at $\overline{U} = 0.05$

Figure 4.6: Examples of the variation of the measured frequency spectra for the NACA0015 POM hydrofoil with (a) varying inflow velocity at $\alpha_o = 8^o$ and (b) varying angle of attack at $\overline{U} = 0.05$. Note that $\overline{\omega} = \omega/\omega_\theta$ is the non-dimensional frequency.

as it was obtained using an electrodynamic shaker, while the in-flowing-water cases ($\overline{U} > 0$) correspond to natural flow-induced vibrations. The results in Fig. 4.6(a) show that the first in-water natural bending frequency was insensitive to variations in the inflow velocity, but the first in-water natural twisting frequency increased with the inflow velocity. Fig. 4.6(b) indicates that the in-water natural frequencies varied slightly with the angle of attack (α_o), but the variation was non-monotonic and was much smaller than the variations observed in Fig. 4.6(a) for varying $\overline{U}$.

4.1.4 Validation study with other experimental measurements for the NACA0015 hydrofoil

To check the validity of the current experimental measurements (by the French Naval Academy Research Institute) and numerical predictions, the measured and predicted lift coefficient (C_L), drag coefficient (C_D), and moment coefficient (C_M) with varying angles of attack for a rigid NACA0015 hydrofoil are compared against the published experimental results (*Jacobs and Sherman*, 1937) in Fig. 4.7. The setup

of the rigid NACA0015 hydrofoil in the current steady is the same as presented in section 4.1.3, but the foil is made of stainless steel and the axis of rotation was at $0.25c$ from the foil's LE. Note that *Jacobs and Sherman* (1937) used a NACA0015 airfoil with $AR = 6$ while the current experiments used a NACA0015 hydrofoil with $AR = 1.92$. Figure 4.7 also includes the predicted lift coefficients from the inviscid thin-airfoil theory given in Eq. (4.1).

$$C_L = 2\pi\alpha_o \tag{4.1}$$

The theoretical steady-state drag coefficients given in Fig. 4.7(b) were calculated using Eq. (4.2), where C_{D_o} is the skin friction drag coefficient based on 1/7 power law, and C_{D_i} is the induced 100% suction drag coefficient.

$$C_D = C_{D_o} + C_{D_i} = 0.0576Re^{-1/5} + C_L^2/(\pi AR) \tag{4.2}$$

The theoretical moment coefficients at the aerodynamic center, $C_{Mo,AC}$, given in Fig. 4.7(c) are zero because the inviscid theory assumes the center of pressure (CP) to be located at the AC.

As shown in Fig. 4.7, the current experimental and numerical results agree well with experimental results of *Jacobs and Sherman* (1937) at approximately the same Reynolds number (Re).

In the current experiments conducted by the French Naval Academy Research Institute (IRENav), the hydrodynamic forces were measured on a rigid (i.e., stainless steel) hydrofoil mounted in a 3-component hydrodynamic balance measuring lift, drag and moment. In that case, the axis of rotation was located at $0.25c$ from the leading-edge (LE). Each data acquisition was for about 10 s with a sampling frequency of 1 kHz. To ensure fully turbulent flow, a roughness strip was placed close to the foil leading edge. Taking into account the mounting system, the uncertainty in the

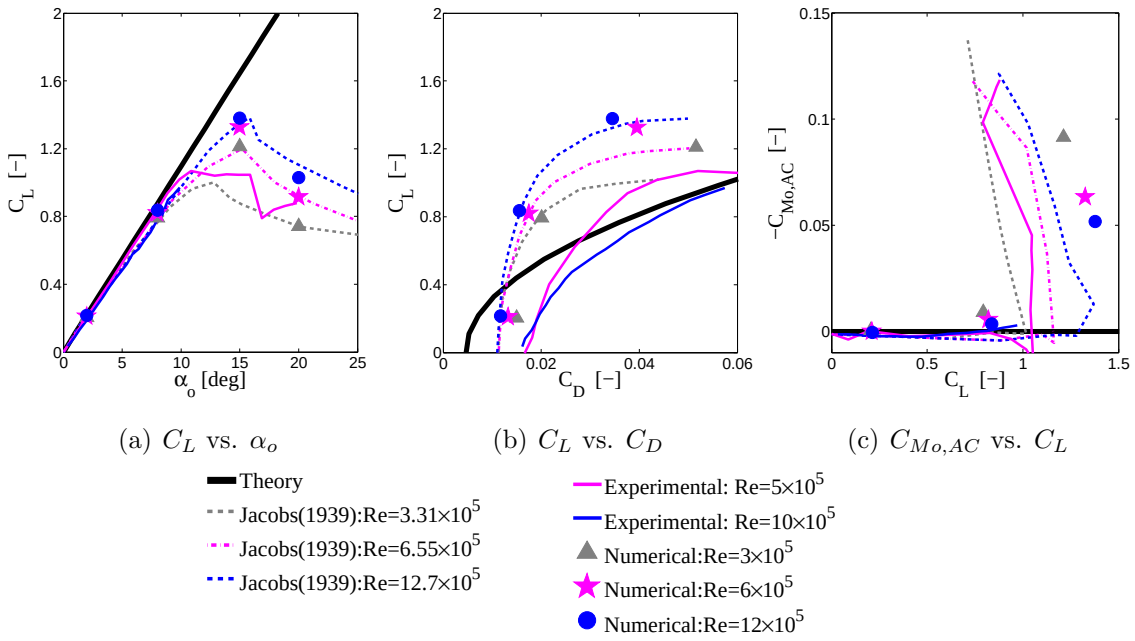

Figure 4.7: (a) C_L vs. α_o, (b) C_L vs. C_D, and (c) $C_{Mo,AC}$ at the aerodynamic center (AC) vs. C_L plots for a rigid NACA0015 foil and at steady-state. The aspect ratio ($AR = s/c$) was 6 for the experiments by *Jacobs and Sherman* (1937) and was 1.92 for the current experiments by the French Naval Academy Research Institute (IRENav). The numerical simulation is based on a 2D uRANS simulation.

angle of attack was about $\pm 0.15^o$. Taking into account the tunnel regulation system, the uncertainties of the flow rate computed from pressure measurements (Fig. 4.4(a)) were $\pm 0.02\ m/s$. The experimental accuracy of the balance obtained from calibrations was $\pm 5\ N$ for the lift, $\pm 1.6\ N$ for the drag and $\pm 1\ Nm$ for the moment.

The results in Fig. 4.7 show that the slopes of the measured and predicted lift coefficients are less than those of inviscid theory. The decrease in slope is caused by the development of a small separated region near the foil's trailing-edge (TE), which expands toward the foil's leading-edge (LE) as the angle of attack increased until the flow was fully separated, i.e. stalled, which occurred at $\alpha_o = 16^o - 18^o$ for the NACA0015 depending on Re. It is noteworthy that the moment coefficient also changed with the development of the trailing-edge vortex (TEV) because of the change in lift and the movement of the center of pressure towards the mid-chord. At

lower Re regions (i.e., $Re < 6 \times 10^5$), the numerical results overestimated the C_D and C_M because the viscous simulation assumed fully turbulent flow, but the actual flow regime might have been transitional.

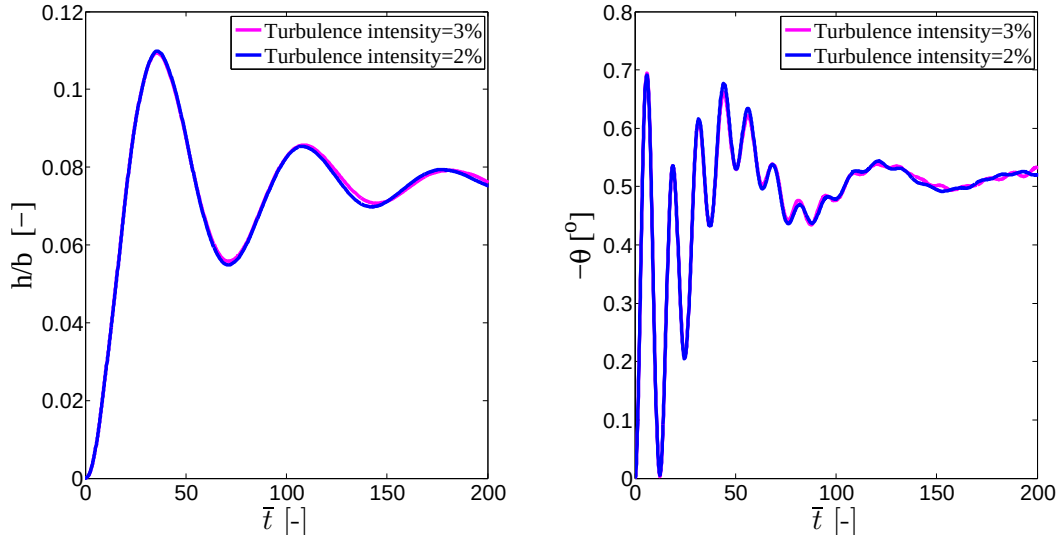

(a) Bending deformations (h/b) (b) Twisting deformations (θ)

Figure 4.8: Variation of the time-histories of (a) bending deformations and (b) twisting deformations with varying inlet turbulence intensity on the flexible NACA0015 POM hydrofoil at $\alpha_o = 8^o$, $\sqrt{\mu} = 0.44$, $\overline{U} = 0.05$, and $Re = 6 \times 10^5$. Note that $\overline{t} = t\omega_\theta$ is the non-dimensional time.

The inlet turbulence intensity is defined as the root-mean-square (RMS) value of the inlet velocity fluctuations divided by the mean inlet velocity. The experimental and numerical setups differ in the inlet turbulence intensity. For the experimental study, the inlet turbulence intensity of 2% is measured at the inlet of the test section, which is about 350 mm from the hydrofoil's leading-edge. For the numerical simulation, on the other hand, the inlet turbulence intensity is set at 3%, as the inlet is set at 550 mm from the hydrofoil's leading-edge. The turbulence intensity of uRANS simulations models generally decreases in the stream-wise direction due to numerical diffusions; Therefore, the inlet turbulence intensity is set to be 3% at the left end of the CFD domain so that at the leading-edge (LE) of the hydrofoil, the numerical turbulence intensity becomes similar to the measured value of 2%. To check the in-

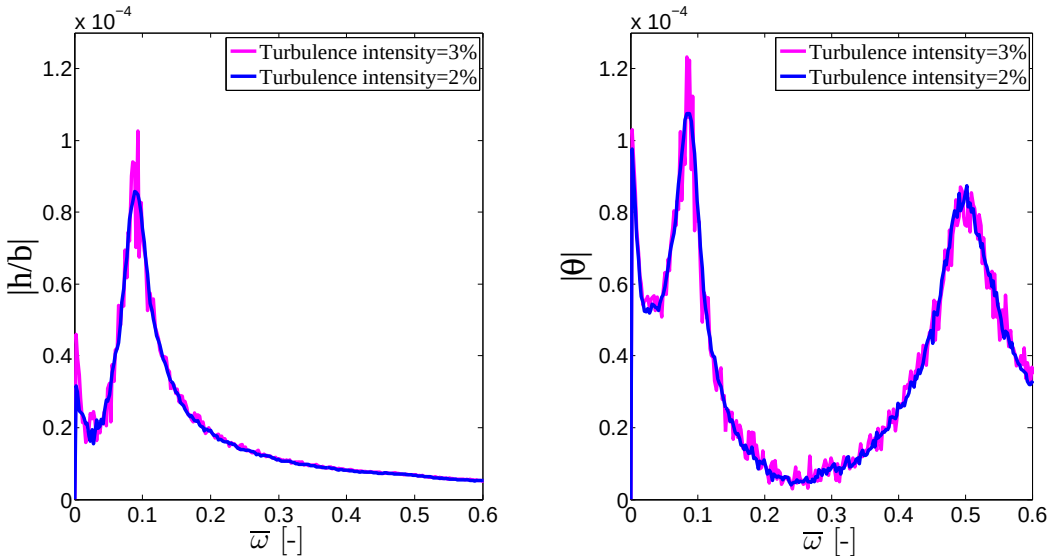

(a) Bending frequencies (b) Twisting frequencies

Figure 4.9: Variation of the predicted frequency spectra ($\overline{\omega} = \omega/\omega_\theta$) of the (a) bending deformations and (b) twisting deformations with varying inlet turbulence intensity for the flexible NACA0015 POM hydrofoil at $\alpha_o = 8^o$, $\sqrt{\mu} = 0.44$, $\overline{U} = 0.05$, and $Re = 6 \times 10^5$. Note that the FFT window size is $\bar{t} = 0 - 2500$.

fluence of inlet turbulence intensity, Figs. 4.8 - 4.9 show the predicted time-histories and frequency spectra, respectively, of bending and twisting deformations for prescribed inlet turbulence intensity of 2% and 3%, respectively. The results show that the difference between 2% and 3% of the inlet turbulence intensity has a practically negligible influence on the numerical predictions.

4.1.5 Prediction of the total loss factor

The total loss factor (also called Q-factor in the acoustic literature) is equal to two times the total damping coefficient (i.e., η_T=$2\zeta_T$) and is the sum of the solid loss factor (η_s) and the fluid loss factor (η_f) .

$$\eta_T \quad = \quad \eta_s + \eta_f. \tag{4.3}$$

For the current NACA0015 POM hydrofoil, the solid damping coefficients for both bending and twisting are assumed to be 2%, and hence $\eta_{s,h} = \eta_{s,\theta} = 0.04$. The theoretical inviscid, uncoupled mode fluid loss factors are calculated following *Blake and Maga* (1975), which was derived based on *Theodorsen* (1935)'s fluid loads, as shown in Eqs. (4.4) - (4.5).

$$\eta_{f,h} = \frac{2C(k)\overline{U}}{\frac{\omega_h^*}{\omega_\theta}(\mu+1)}, \tag{4.4}$$

$$\eta_{f,\theta} = \frac{d[2C(k)e-1]\overline{U}}{\frac{\omega_\theta^*}{\omega_\theta}\left[\mu r_\theta^2 + (\frac{1}{8}+a^2)\right]}. \tag{4.5}$$

It should be noted that Eqs. (4.4) - (4.5) neglected the flow-induced bend-twist coupling terms (i.e., off-diagonal terms in $\mathbf{M}^T$ and $\mathbf{C}^T$ in Eqs. (2.6) and (2.7)).

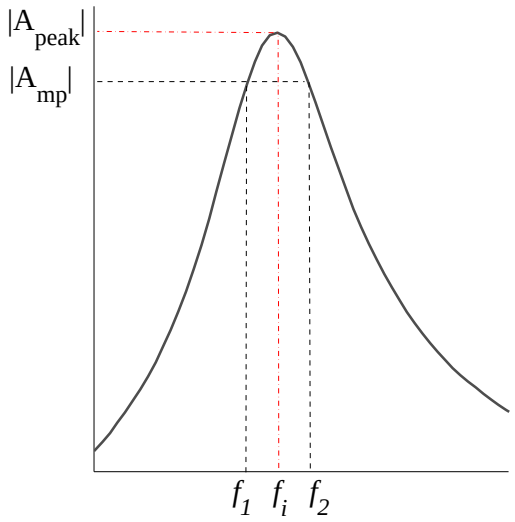

Figure 4.10: Illustration of the mobility peak power down method used to calculate the total loss factors based on the frequency spectrum.

The mobility peak power down method by *Cremer et al.* (2005), Eq. (4.6), was used to calculate the total loss factor ($\eta_T = 2\zeta_T$), by processing the frequency spectra of both the experimental measurements and viscous simulations. Note that the experimental results by IRENav only have the frequency spectra, therefore the logarithmic

decrement method cannot be used in this section. The mobility peak power down method used to calculate the total loss factor is shown in Eq. (4.6), and in Fig. 4.10.

$$\eta_T = \frac{f_2 - f_1}{f_i\sqrt{p-1}}, \tag{4.6}$$

where p is the number of the reduction of the mobility. In this study, $p = 5$ was used when processing both experimental and viscous FSI results.

In Eq. (4.6) and Fig. 4.10, f_i is the frequency of interest (e.g. bending and twisting natural frequencies, or the vortex shedding frequency) with peak amplitude (i.e., $|\mathrm{A_{peak}}|$). f_1 and f_2 correspond to the frequencies on the left and right, respectively, at the amplitude $|\mathrm{A_{mp}}|$ (i.e., "p"th mobility peak amplitude, on each side of f_n) as shown in Fig. 4.10. It should be noted that for $p = 5$, the $\sqrt{5}$-th amplitude reduction, $|\mathrm{A_{mp}}| = |\mathrm{A_{peak}}|/\sqrt{5}$.

4.2 Influence of the reduced velocity

Detailed variation of the time and frequency response with inflow velocity (as reflected by the change in $\overline{U} = U/\omega_\theta b$, the reduced velocity) will be shown in this section.

4.2.1 Time-histories of the bending and twisting responses at pre-stall conditions

Figure 4.11 shows the time-histories of the bending and twisting deformations with reduced velocity ($\overline{U} = 0.02 \sim 0.1$, $Re = 3 \sim 12 \times 10^5$) on the flexible NACA0015 POM hydrofoil ($\sqrt{\mu} = 0.44$) at $\alpha_o = 8^o$. The results in Fig. 4.11 indicate that the amplitudes of bending and twisting deformations increase with $\overline{U}$ before the stall angle. It should be noted that $\alpha_{\mathrm{eff}} = \alpha_o - \theta$ and $\theta < 0$, so $\alpha_{\mathrm{eff}} > \alpha_o$ because flow induces a clockwise moment as the center of pressure (CP) is upstream of the elastic

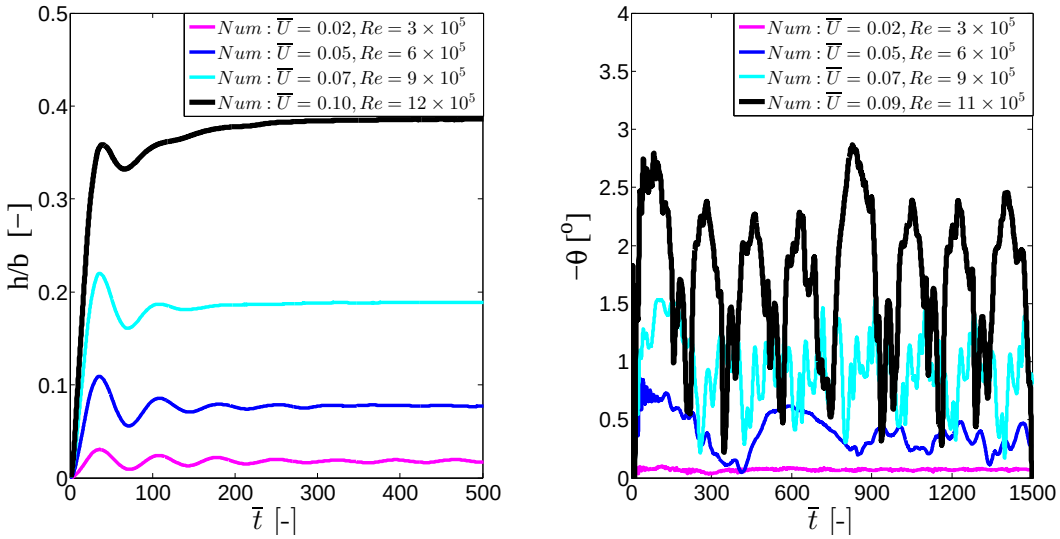

(a) Bending deformations (h/b) (b) Twisting deformations (θ)

Figure 4.11: Variation of the predicted time-histories of (a) bending deformations and (b) twisting deformations with varying reduced velocity ($\overline{U} = 0.02 \sim 0.1$, $Re = 3 \sim 12 \times 10^5$) on the flexible NACA0015 POM hydrofoil ($\sqrt{\mu} = 0.44$) at $\alpha_o = 8^o$. Note that $\overline{t} = t\omega_\theta$ is the non-dimensional time.

axis (EA) prior to stall. Stall occurs when $\alpha_{\text{eff}} = 16^o \sim 18^o$ for $Re = 5 \sim 12 \times 10^5$, based on the rigid NACA0015 results shown in Fig. 4.7(a).

4.2.2 Frequency spectra of the bending and twisting responses at pre-stall conditions

Figure 4.12 presents the predicted and measured variation of the frequency spectra (via fast Fourier transform (FFT) method) of the bending and twisting deformations with varying reduced velocity ($\overline{U} = 0.02 \sim 0.1$, $Re = 3 \sim 12 \times 10^5$) for the flexible NACA0015 POM hydrofoil ($\sqrt{\mu} = 0.44$) at $\alpha_o = 8^o$. For all the cases, $\overline{U}$ was varied by fixing ω_θ and varying U. Generally, the predicted first in-water natural bending and twisting frequencies are in good agreement with experimental measurements at $\overline{U} = 0.02$ and 0.05. It should be noted that experimental measurements are not available for $\overline{U} > 0.05$. Figure 4.12 shows that the viscous FSI model is able to capture the frequency peaks corresponding to the natural bending and twisting frequencies

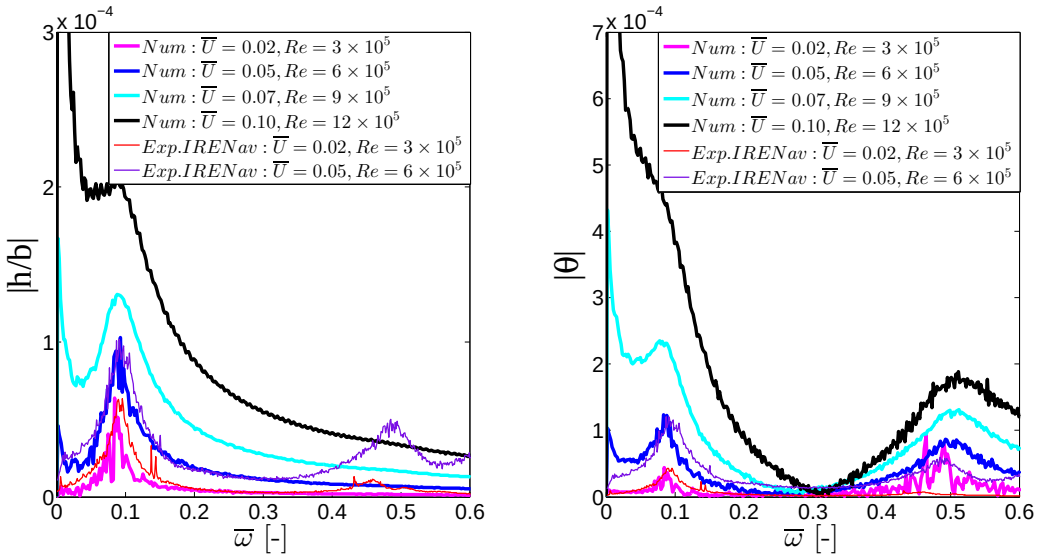

(a) Bending deformations (h/b) (b) Twisting deformations (θ)

Figure 4.12: Variation of the predicted and measured frequency spectra ($\overline{\omega} = \omega/\omega_\theta$) of (a) bending deformations and (b) twisting deformations with varying reduced velocity ($\overline{U} = 0.02 \sim 0.1$, $Re = 3 \sim 12 \times 10^5$) for the flexible NACA0015 POM hydrofoil at $\alpha_o = 8^o$. Note that the FFT window size is $\bar{t} = t\omega_\theta = 0 - 2500$, and experimental data were only available for $\overline{U} = 0.02 - 0.05$.

for the twisting deformation, and the natural bending frequency peak in the bending deformation, but the predicted twisting frequency peak in the bending deformation was much smaller than the measured value. In addition, the numerical model could not capture a third frequency peak that was observed in the experiment because it corresponded to the second bending mode ($f^*_{h,2}$), as the current 2-DOF model is designed to capture the first bending and the first twisting modes only.

Table 4.2 compares the predicted and measured first in-water natural bending and twisting frequencies with varying reduced velocity (i.e., varying inflow velocity) based on frequency spectra shown in Fig. 4.12 through the FFT method. In general, good comparisons are observed between predictions and measurements.

The results shown in Figs. 4.6 and 4.12, as well as Table 4.2, suggest that while the first in-water natural bending frequency is relatively insensitive to variations in $\overline{U}$, the first in-water natural twisting frequency tends to increase with increasing reduced

Table 4.2: Comparison of the predicted and measured first in-water natural bending and twisting frequencies (f_h&f_θ in-air and f_h^*&f_θ^* in-water). It should be noted that the numerical values with superscript "+" are computed using *Theodorsen* (1935)'s approach as they correspond to the still-water conditions.

f_h =81 [Hz] f_θ =390 [Hz]		$\overline{U}=0$ Re=0×10^5	$\overline{U}=0.02$ Re=3×10^5	$\overline{U}=0.05$ Re=6×10^5	$\overline{U}=0.07$ Re=9×10^5	$\overline{U}=0.1$ Re=12×10^5
f_h^* [Hz]	Exp.	34	36	36	N/A	N/A
	Num.	33^+	33	37	35	35
f_θ^* [Hz]	Exp.	184	182	192	N/A	N/A
	Num.	190^+	184	195	199	202

velocity. The change of the first in-water natural twisting frequency with $\overline{U}$ is due to the dependence of the fluid damping and fluid stiffness terms with the $\overline{U}$, as shown in Eqs. (2.7) and (2.8), and viscous FSI effects (see *Chae et al.* (2015b) for more details). The resonance frequencies of a flexible hydrofoil are different between still-water and flowing-water conditions, particularly for lightweight structures operating at high speed in a dense fluid, i.e. cases with low μ and high $\overline{U}$, because of changes in fluid forces in phase with the acceleration, velocity, and displacement, respectively, with operating conditions. The same is expected to be true for flexible mooring lines and pipelines in-water (*Klamo*, 2007). In addition, the resonance frequencies may change non-monotonically with $\overline{U}$ due to viscous effects on the hydrodynamic loads caused by transition, flow separations, and shed vortices in the wake.

4.2.3 Total loss factors of the bending and twisting responses at pre-stall conditions

Figures 4.13 - 4.14 show a comparison of the total loss factors (η_T) obtained using the viscous FSI solver, using inviscid, uncoupled mode linear theory given by *Blake and Maga* (1975) in Eqs. (4.4) - (4.5), and with experimental measurements. Experimental and linear theory results are shown for the current NACA0015 POM hydrofoil as well as the stainless steel hydrofoil tested by *Blake and Maga* (1975) and

the aluminum hydrofoil tested by *Reese* (2010). Viscous FSI simulations were only conducted for the NACA0015 POM hydrofoil.

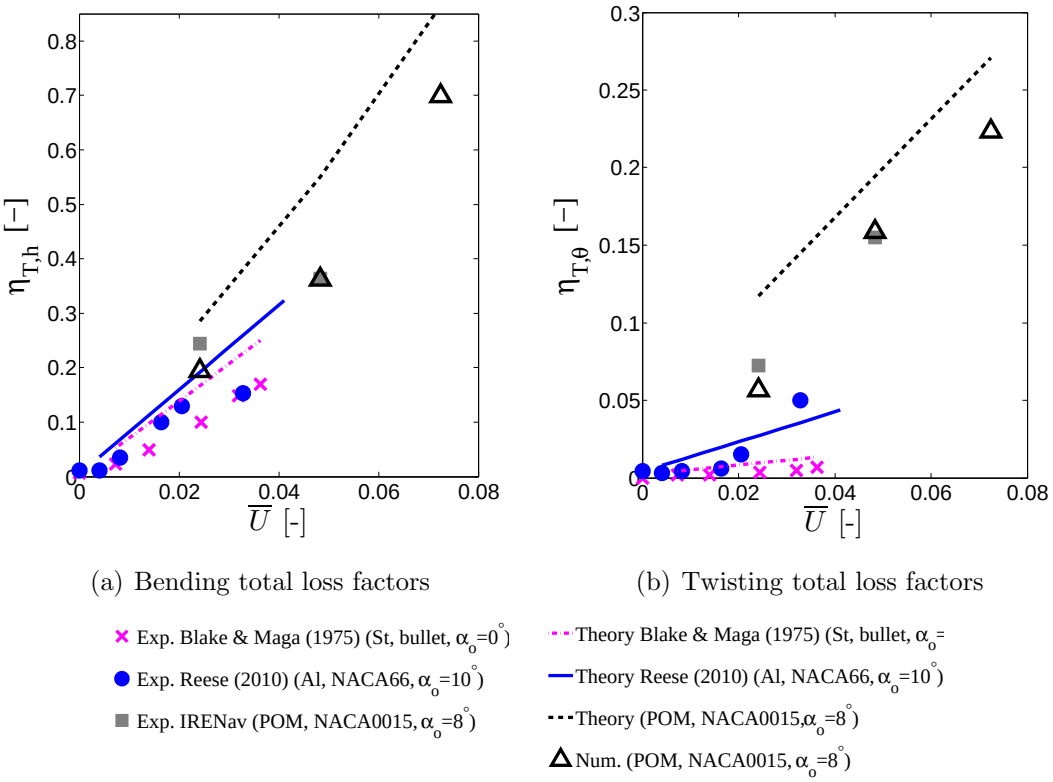

(a) Bending total loss factors

(b) Twisting total loss factors

Figure 4.13: Comparison of the measured and predicted total loss factor (η_T) vs. reduced velocity ($\overline{U}$) for a (a) bending and (b) twisting deformations for the flexible NACA0015 POM hydrofoil. Also shown are experimental measurements of a stainless steel bullet shape hydrofoil from *Blake and Maga* (1975) and an aluminum NACA66 hydrofoil from *Reese* (2010), along with the theoretical prediction obtained using Eqs. (4.4) - (4.5) according to *Blake and Maga* (1975). Note that viscous FSI simulations are only shown for the POM NACA0015 hydrofoil.

The assumed solid damping values for the three different hydrofoils are shown in Table 4.1. Although the geometry and natural frequencies of the stainless steel and aluminum hydrofoils examined in the experimental studies by *Blake and Maga* (1975) and by *Reese* (2010), respectively, are not the same as the current experimental and numerical model for the POM NACA0015 hydrofoil, the trends of the variation of total loss factor with the reduced velocity ($\overline{U}$) and relative mass ratio (μ) are similar.

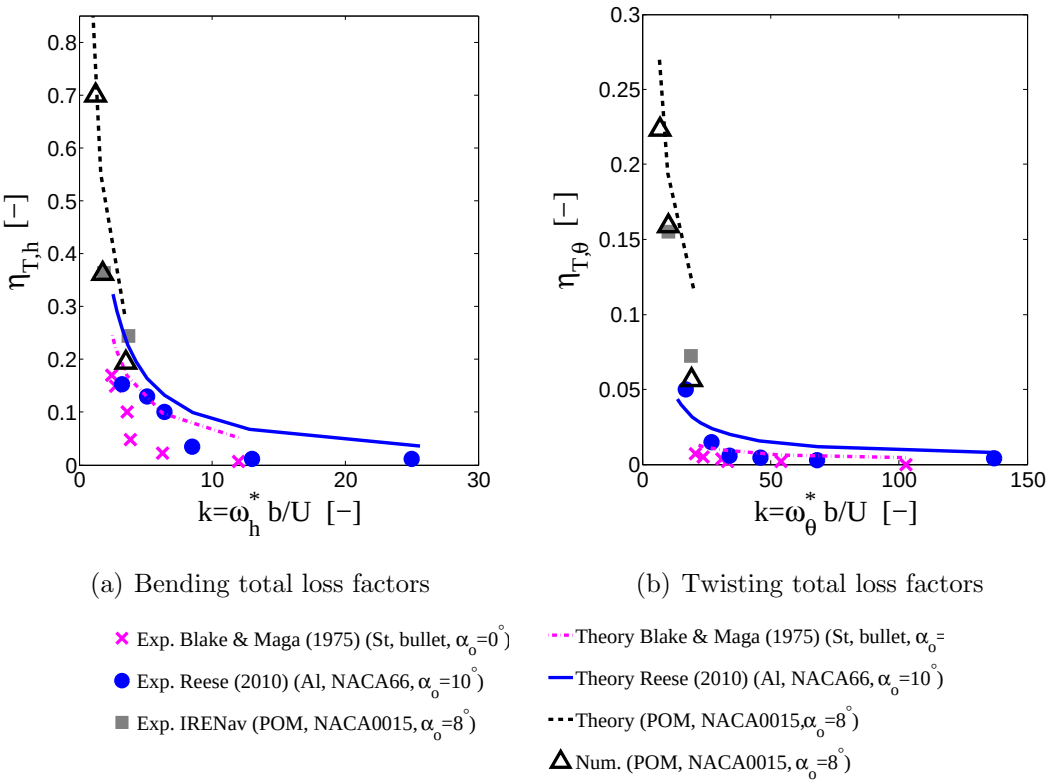

(a) Bending total loss factors

(b) Twisting total loss factors

Figure 4.14: Comparison of the measured and predicted total loss factor (η_T) vs. reduced frequency (k) for a (a) bending and (b) twisting deformations for the flexible NACA0015 POM hydrofoil. Also shown are experimental measurements of a stainless steel bullet shape hydrofoil from *Blake and Maga* (1975) and an aluminum NACA66 hydrofoil from *Reese* (2010), along with the theoretical prediction obtained using Eqs. (4.4) - (4.5) according to *Blake and Maga* (1975). Note that viscous FSI simulations are only shown for the POM NACA0015 hydrofoil.

Generally, the total loss factor increases with increasing $\overline{U}$ (and hence decreases with $k = \omega b/U = \omega/(\omega_\theta \overline{U})$) and with decreasing solid-to-fluid added mass ratio (μ), consistent with the trends as expected in Eqs. (4.4)-(4.5). Note that the current NACA0015 POM hydrofoil has a higher $\overline{U}$ (more flexible) and lower $\sqrt{\mu}$ (lighter) than the aluminum NACA66 foil tested by *Reese* (2010) and the stainless steel bullet shape hydrofoil tested by *Blake and Maga* (1975), as shown in Table 4.1. It is noteworthy that for most of the cases shown in Fig. 4.14, $k > 1$, so the wake pattern contains distinct point vortices instead of a simple flat vortex sheet, as shown later in Fig.

4.16. The inviscid, uncoupled mode linear theory equation provided in *Blake and Maga* (1975) tends to over-predict the total loss factor for all three hydrofoils, and the over-prediction increases with decreasing $\sqrt{\mu}$. This is both because the linear theory by *Blake and Maga* (1975) ignores the contribution of flow-induced bend-twist coupling of the hydrodynamic loads (i.e., the off-diagonal terms in $\mathbf{C}^T$ and $\mathbf{K}^T$ in Eqs. (2.7) and (2.8)) and because it ignores viscous effects. Note that e, d, and $C(k)$ will be different that assumed in linear inviscid theory because of the movement on the center of pressure, the magnitude and frequency of the effective induced velocity by the wake vortices, the change in shedding frequencies, and the resulting phase lag caused by the wake vortices. The over-prediction of η_T by the inviscid theory increases with increasing $\overline{U}$ and decreasing $\sqrt{\mu}$, as shown in Fig. 4.13. This over-prediction is not desirable since unexpected lower damping can accelerate fatigue, lead to longer settling time, result in greater noise and vibration, and may lead to earlier susceptibility to flutter and divergence (as observed in *Chae et al.* (2013)).

4.2.4 Comparison of the predicted rigid and flexible foil responses and vortex shedding frequencies at post-stall condition

Figure 4.15 compares the time-histories of the predicted bending and twisting deformations of the flexible NACA0015 POM hydrofoil ($\sqrt{\mu} = 0.44$) with varying reduced velocity ($\overline{U} = 0.02 \sim 0.09$, $U = 3 \sim 11 m/s$) at $\alpha_o = 20^o$, post-stall. The results in Fig. 4.15 show that the amplitudes of the predicted bending and twisting deformations increase with $\overline{U}$, even for the post stall angle case because of the higher fluid loads.

Figure 4.16 shows snapshots of the vorticity contours of the flow around the rigid and flexible NACA0015 hydrofoils with $\alpha_o = 20^\circ$ at different time instances ($\bar{t} = t\omega_\theta$) for the rigid foil ($\overline{U} = 0$) with U= 3 m/s (i.e., $Re = 3 \times 10^5$), and for the flexible foil ($\overline{U} = 0.02 \sim 0.09$) with U= 3 $\sim$ 11 m/s (i.e., $Re = 3 \times 10^5 \sim 11 \times 10^5$). Notice that

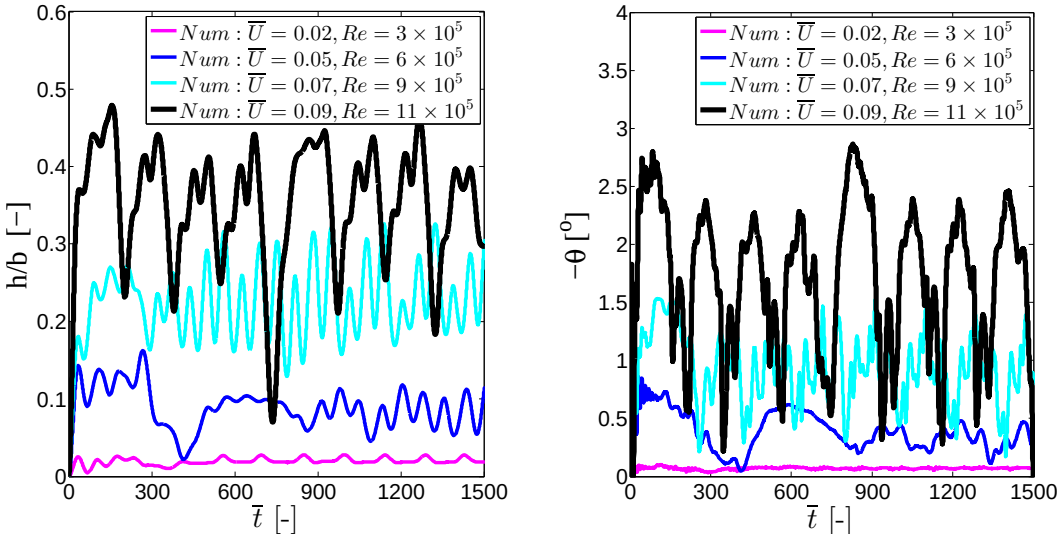

(a) Bending deformations (h/b) (b) Twisting deformations (θ)

Figure 4.15: Variation of the predicted time-histories of (a) bending deformations and (b) twisting deformations with different reduced velocities ($\overline{U} = 0.02 \sim 0.09$, $Re = 3 \sim 11 \times 10^5$) for the flexible NACA0015 POM hydrofoil ($\sqrt{\mu} = 0.44$) at $\alpha_o = 20^o$. Note that $\overline{t} = t\omega_\theta$ is the non-dimensional time.

only U is varied and f_θ=390 Hz for the flexible foil. It should be noted that $\omega_\theta = 2\pi f_\theta$ for the rigid foil is theoretically infinite. To allow consistent comparisons with the flexible foil results, $\overline{t}$ for the rigid foil is defined using f_θ= 390 Hz, the same as for the flexible foil and the results in the left most column were obtained for U=3 m/s. For the rigid foil ($\overline{U} = 0$), von Kármán vortex type wake patterns are observed. The vorticity patterns and vortex shedding frequencies are very different for the flexible foil compared to the rigid foil because the bending and twisting deformations generate, modify, and interact with the vorticity field around the foil, as shown in Fig. 4.16.

Figure 4.17 shows the wake patterns of rigid and flexible hydrofoils ($\sqrt{\mu} = 0.44$) at the steady-state condition with $\alpha_o = 20^\circ$ (the rigid foil ($\overline{U} = 0$) with U= 3 m/s (i.e., $Re = 3 \times 10^5$), and for the flexible foil ($\overline{U} = 0.02 \sim 0.09$) with U= 3 $\sim$ 11 m/s (i.e., $Re = 3 \times 10^5 \sim 11 \times 10^5$). When the hydrofoil becomes increasingly flexible, the wake pattern changes from the"2S" mode to the "P+S" mode. Following *Williamson and Roshko* (1988), the definition of the "S" and "P" mode correspond to single

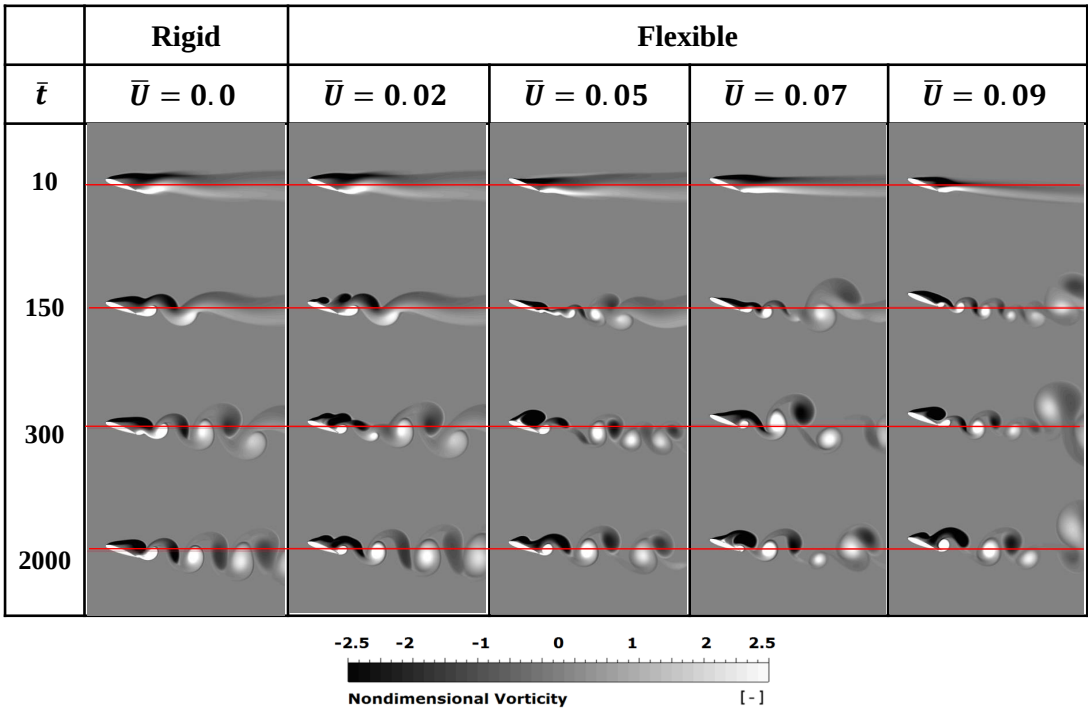

Figure 4.16: Snapshots of the non-dimensional vorticity ($\varpi = \omega b/U$) contours of the flow around the rigid and flexible NACA0015 hydrofoils with $\alpha_o = 20^\circ$ at different time instances ($\bar{t} = t\omega_\theta$) for the rigid foil ($\overline{U} = 0$) with U= 3 m/s (i.e., $Re = 3 \times 10^5$), and for the flexible foil ($\overline{U} = 0.02 \sim 0.09$) with U= 3 $\sim$ 11 m/s (i.e., $Re = 3 \times 10^5 \sim 11 \times 10^5$). The horizontal lines pass through the elastic axis of the undeformed hydrofoil. Notice that only U is varied and f_θ=390 Hz for the flexible foil. It should be noted that $\omega_\theta = 2\pi f_\theta$ for the rigid foil is theoretically infinite. To allow consistent comparisons with the flexible foil results, $\bar{t}$ for the rigid foil is defined using f_θ= 390 Hz, the same as for the flexible foil and the results in the left most column were obtained for U=3 m/s.

vortex and pair vortices, respectively. There is a change in wake pattern because the foil's deformations modify the flow separation and wake patterns. For the "2S" mode, a vortex is fed into the wake in each half cycle, which is known as Kármán vortex shedding. The "P+S" mode has asymmetric wakes, consisting of a pair of counter-rotating vortices as well as a solitary vortex; the solitary vortex is caused by the bending motion, as it is locked in to the bending natural frequency.

Figure 4.18 shows the variation of frequency spectra by taking the FFT of the

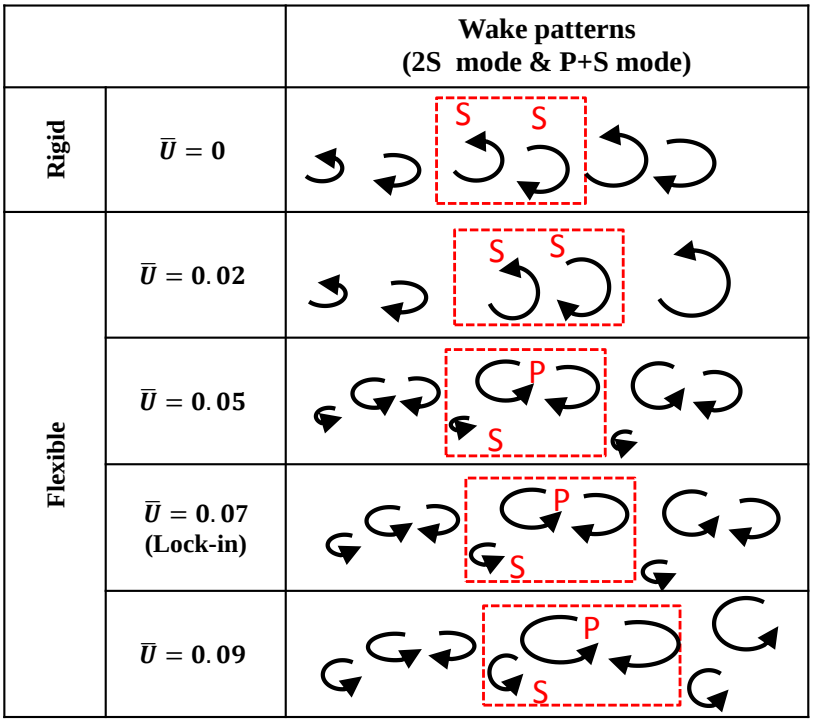

Figure 4.17: Wake patterns at the steady-state condition with $\alpha_o = 20°$ for the rigid and flexible NACA0015 hydrofoils ($\sqrt{\mu} = 0.44$). Note that the horizontal lines pass through the undeformed hydrofoils elastic axis and "S" means solitary vortex, and "P" means pair of counter-rotating vortices.

time-histories of the predicted lift and moment coefficients. The red dashed line is the primary vortex shedding frequency, f_{vs}, and the blue dotted line is the first in-water natural bending frequency, f_h^*. The first in-water natural bending frequencies varied slightly with inflow velocity, and are the same as those shown in Fig. 4.12 and Table 4.2. The results for the rigid hydrofoil show that the primary vortex shedding frequency varies almost linearly with the inflow velocity, and the corresponding reduced frequency is approximately $k_{\text{vs,rigid}}$ =2.5 ($k_{\text{vs,rigid}} = 2\pi f_{\text{vs,rigid}} b/U$). For the flexible hydrofoil, however, the reduced vortex shedding frequency is not constant. In particular, for $U = 7 \sim 9m/s$ (i.e., $\overline{U} = 0.06 \sim 0.07$), the vortex shedding frequencies of the flexible hydrofoil snap into the first in-water natural bending frequency of the flexible hydrofoil (i.e., lock-in), which lead to amplified vibrations and load fluctuations. It should be noted that the FFT results show zero mean frequency, as the mean

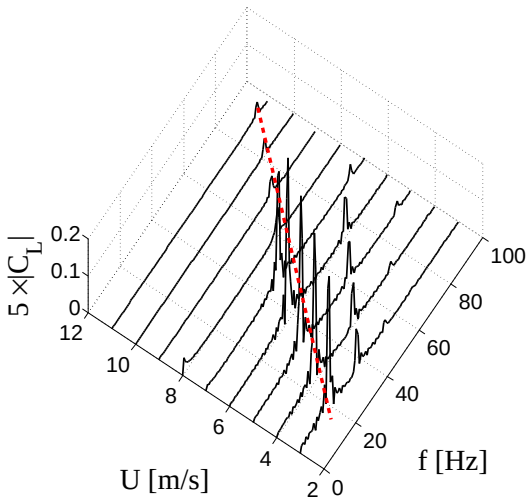

(a) C_L of rigid foil ($\overline{U}$=0)

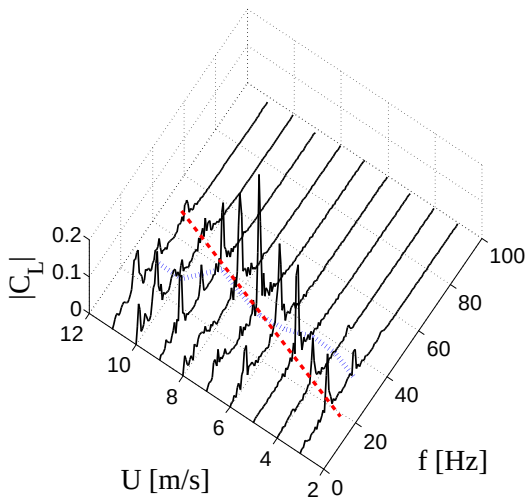

(b) C_L of flexible foil ($\overline{U}$=0.02-0.09)

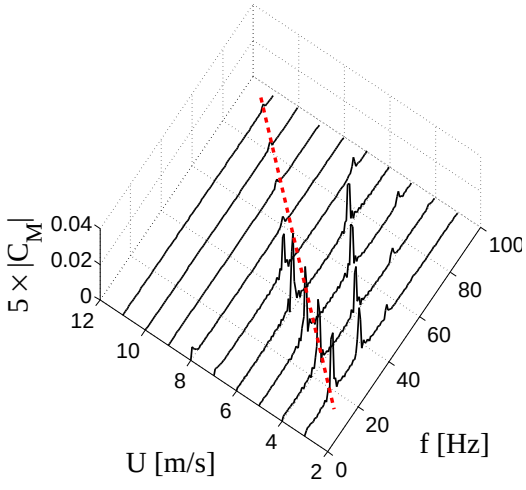

(c) C_M of rigid foil ($\overline{U}$=0)

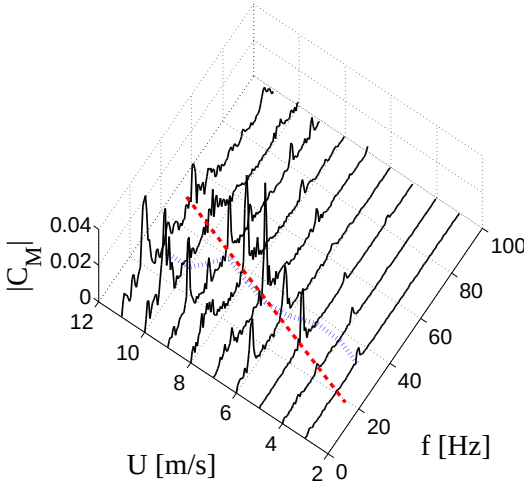

(d) C_M of flexible foil ($\overline{U}$=0.02-0.09)

Figure 4.18: Frequency spectra of the lift coefficients (C_L) of the (a) rigid foil and (b) flexible foil, and moment coefficients (C_M) of the (c) rigid foil and (d) flexible hydrofoil at $\alpha_o = 20°$ and $U = 3 \sim 11m/s$ (i.e., $\overline{U} = 0 \sim 0.09$). Note that FFT window size is $\bar{t} = t\omega_\theta = 1000 - 2500$ of the flexible foil to focus on the established vortex shedding frequencies. The red dashed line is the primary vortex shedding frequency, f_{vs}, and the blue dotted line is the first in-water natural bending frequency, f_h^*. It should be noted that the dimensional parameters are plotted as the natural frequency of the rigid foil is theoretically infinite.

values are subtracted from the data before taking the FFT. Thus, comparing the amplitudes from the FFT alone might be misleading. Nevertheless, the increase in the amplitude of the fluctuation at lock-in can be observed in Fig. 4.18, and the change in the trend of the vortex shedding frequency for the lock-in case with $U = 7 \sim 9$ m/s (i.e., $\overline{U} = 0.06 \sim 0.07$) can be observed in Figs. 4.15, 4.16, and 4.18.

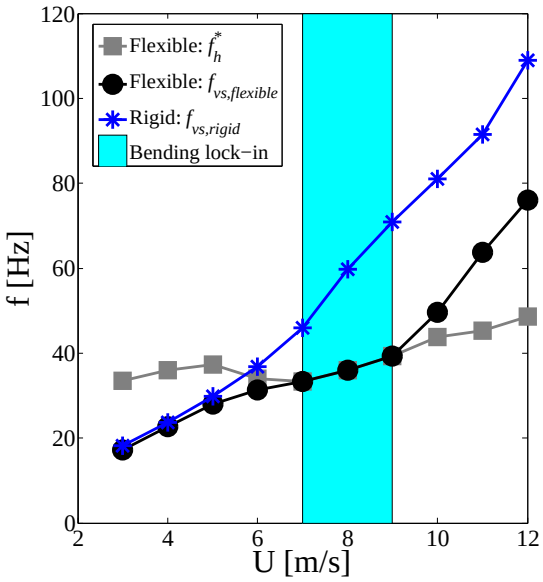

Figure 4.19: Variation of the vortex shedding frequencies and natural frequencies with inflow velocity ($U = 3 \sim 12$ m/s, $\overline{U} = 0 \sim 0.09$) for the rigid and flexible NACA0015 hydrofoil at $\alpha_o = 20^o$. The shadowed blue region, $U = 7 \sim 9 m/s$ (i.e., $\overline{U} = 0.06 \sim 0.07$), corresponds to the lock-in condition, where the vortex shedding frequency matches with the first in-water natural bending frequency. This plot is a summary of the results shown in Fig. 4.18. It should be noted that the dimensional parameters are plotted as the natural frequency of the rigid foil is theoretically infinite.

Fig. 4.19 shows the variation of the predicted vortex shedding frequencies with inflow velocity for both the rigid and flexible hydrofoils, as well as the predicted first in-water natural bending frequency of the flexible hydrofoil. The results show that before and after the lock-in region, the slope of the vortex shedding frequency versus inflow velocity (U) curve for the flexible foil is similar to that of the rigid foil, but the shedding frequency of the rigid foil is higher than that of the flexible foil. Hence, the reduced shedding frequency of the rigid hydrofoil is $k_{\mathrm{vs,rigid}}$=2.5, which is higher

than that of the flexible hydrofoil in the lock-off region with $k_{\text{vs,flexible}}$=1.3 ($k_{\text{vs,flexible}} = 2\pi f_{\text{vs,flexible}} b/U$). This is because the flexible hydrofoil's bend-twist motion changes the wake characteristics and stimulates earlier shedding. It should be noted that the dimensional parameters are plotted in Figs. 4.18 - 4.19 as the natural frequency of the rigid foil is theoretically infinite.

Figure 4.20 shows the frequency spectra of the flow-induced moment coefficient, C_M, for both the rigid and the flexible hydrofoils at $\alpha_o = 20^\circ$ ($\overline{U} = 0$ for rigid foil and $\overline{U} = 0.04 \sim 0.09$ for flexible foil (i.e.$Re = 5 \times 10^5 \sim 11 \times 10^5$)), where $\overline{U}$=0.065 is the lock-in case and $\overline{U}$=0.04 & 0.09 are the lock-off cases for the flexible hydrofoil. The results in Fig. 4.20(c) show that the flexible hydrofoil is in lock-in with the bending mode at $\overline{U} = 0.065$, where the first in-water natural bending frequency is the same as the vortex shedding frequency ($f_h^* = f_{\text{vs}}$); hence, the amplitudes of hydrodynamic loads are amplified. Moreover, the dynamic response of the flexible hydrofoil has subharmonic and harmonic frequencies of the vortex shedding frequencies (i.e., $1/2 f_{\text{vs}}$, f_{vs}, $2f_{\text{vs}}$, $3f_{\text{vs}}$...), as observed in Fig. 4.20 (b) - (d).

4.3 Influence of angle of attack

The dynamic responses of flexible hydrofoils are expected to be sensitive to variations in the angle of attack (α_o) due to changes in the dynamic lift, center of pressure (CP), and wake patterns. Detailed variations of the time and frequency responses with angle of attack are shown in this section.

4.3.1 Time-histories of the bending and twisting responses

Figure 4.21 shows the predicted time-histories of the bending and twisting deformations with varying angle of attack ($\alpha_o = 2^o \sim 20^o$) for the flexible NACA0015 POM hydrofoil ($\sqrt{\mu} = 0.44$) for $\overline{U} = 0.05$ and $Re = 6 \times 10^5$.

Before the foil stalls, α_{eff} <$16^o \sim 18^o$, the amplitude of twisting deformation

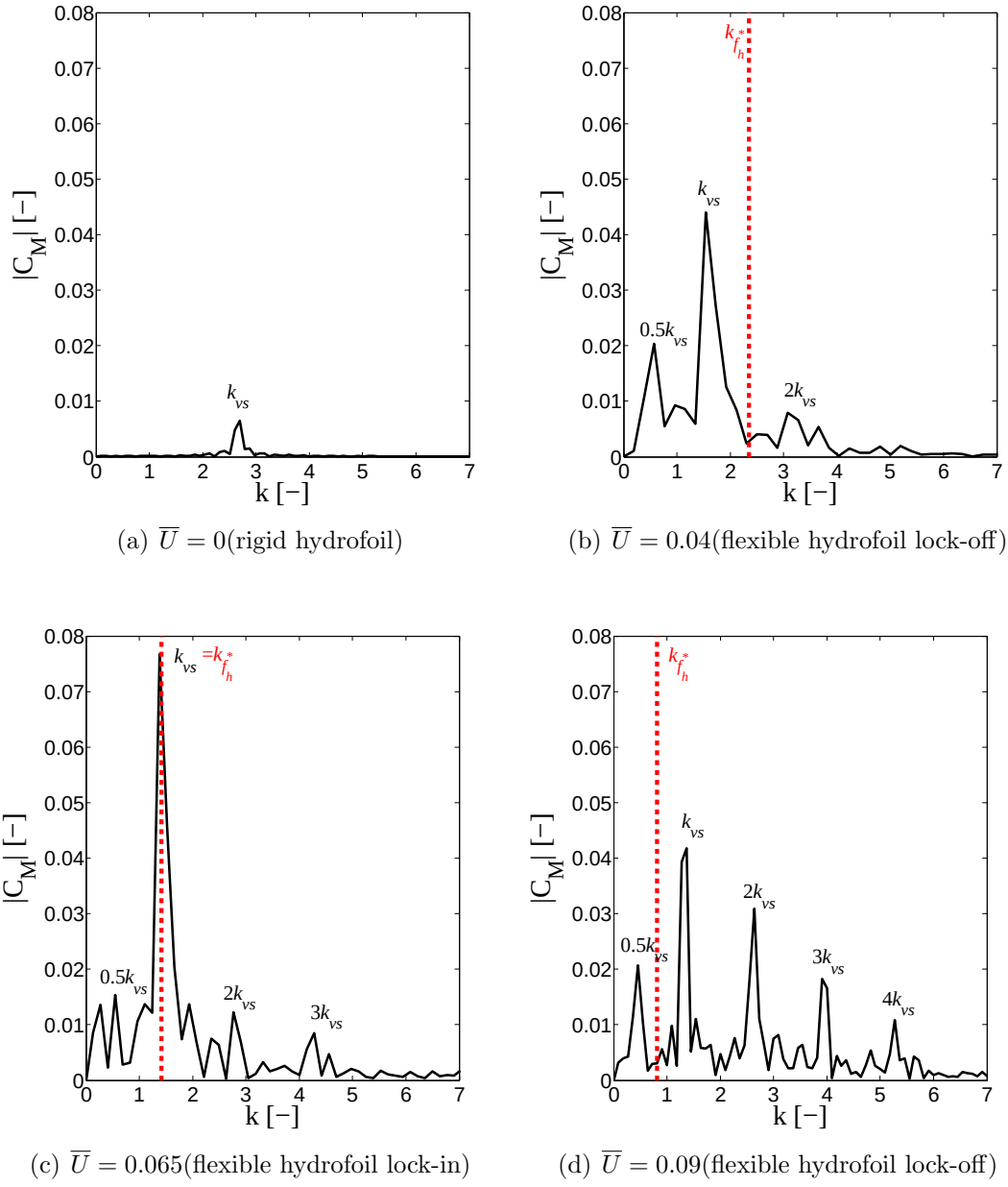

(a) $\overline{U} = 0$(rigid hydrofoil)

(b) $\overline{U} = 0.04$(flexible hydrofoil lock-off)

(c) $\overline{U} = 0.065$(flexible hydrofoil lock-in)

(d) $\overline{U} = 0.09$(flexible hydrofoil lock-off)

Figure 4.20: The frequency spectra of C_M at (a) $\overline{U} = 0$ (rigid NACA0015 hydrofoil), (b) $\overline{U} = 0.04$ (flexible NACA0015 POM hydrofoil lock-off case), (c) $\overline{U} = 0.065$ (flexible NACA0015 POM hydrofoil lock–in case), and (s) $\overline{U} = 0.09$ (flexible NACA0015 POM hydrofoil lock-off case) at $\alpha_o = 20°$ and $\sqrt{\mu} = 0.44$. Note that the FFT window size is $\bar{t} = t\omega_\theta = 2000 \sim 2500$.

increases approximately linearly with the angle of attack because the elastic flow-induced deformations are linearly related to the lift force, which varies approximately linearly with the angle of attack until a trailing-edge vortex (TEV) develops at $\alpha_o >$

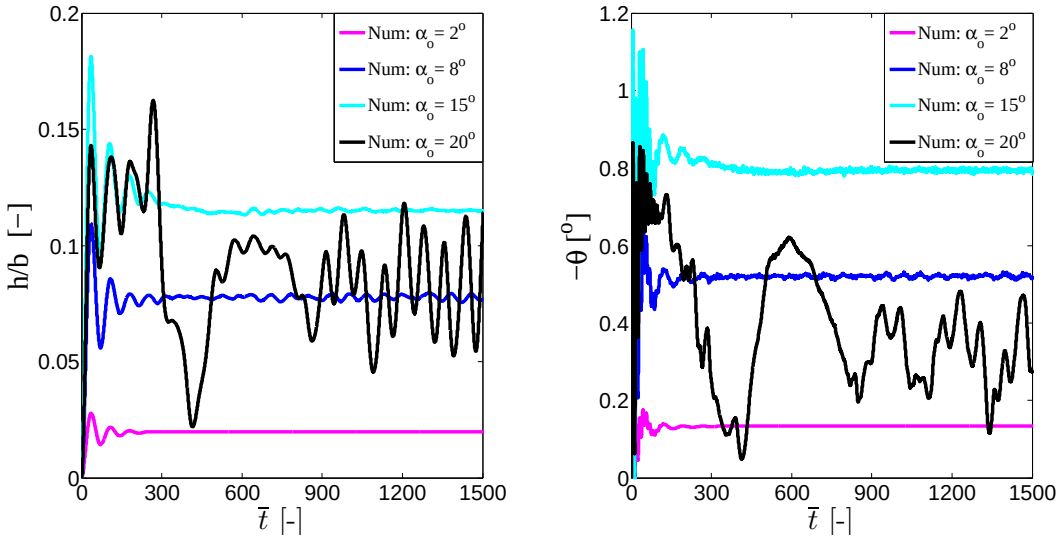

(a) Bending deformations (h/b) (b) Twisting deformations (θ)

Figure 4.21: The effect of the angle of attack on the predicted time-histories of the (a) bending and (b) twisting deformations of a flexible NACA0015 POM hydrofoil ($\sqrt{\mu} = 0.44$) for $\overline{U} = 0.05$ and $Re = 6 \times 10^5$. Note that $\overline{t} = t\omega_\theta$ is the non-dimensional time.

8^o, as shown in Fig. 4.7. After the foil stalls, $\alpha_{\text{eff}} > 16^o \sim 18^o$, the mean lift drops and the mean amplitude of twisting deformation also shows a sudden drop along with the development of large oscillations due to dynamic vortex shedding.

4.3.2 Frequency spectra of the bending and twisting responses

Figure 4.22 shows the variation of the predicted and measured frequency spectra of first in-water natural bending and twisting frequencies with angle of attack for the flexible NACA0015 POM hydrofoil ($\sqrt{\mu} = 0.44$) at $\overline{U} = 0.05$ and $Re = 6 \times 10^5$. The results show good comparisons between the predicted and measured response at $\alpha_o = 2^o$ and $\alpha_o = 8^o$. Experimental data are not available for $\alpha_o > 8^o$ to avoid breaking the foil and to avoid an interference effect from the top and bottom wall boundary layers of the test section.

Table 4.3 compares the predicted and measured first in-water natural bending and twisting frequencies with angle of attack based on the frequency response. The

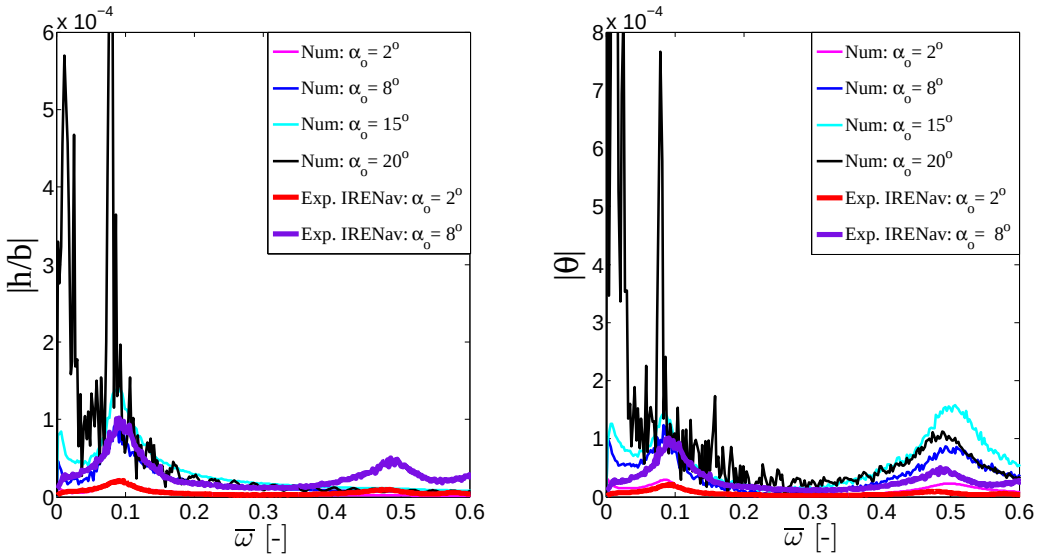

(a) Bending deformations (h/b) (b) Twisting deformations (θ)

Figure 4.22: Variation of the predicted and measured frequency spectra ($\overline{\omega} = \omega/\omega_\theta$) of the (a) bending deformations and (b) twisting deformations with angle of attack for the flexible NACA0015 POM hydrofoil ($\sqrt{\mu} = 0.44$) at $\overline{U} = 0.05$ and $Re = 6 \times 10^5$. Note that the FFT window size is $\overline{t} = 0 - 2500$, and experimental data were only available for $\alpha_o = 2^o$ & 8^o.

Table 4.3: Comparison of the predicted and measured first in-water natural bending and twisting frequencies for a flexible NACA0015 POM hydrofoil ($\sqrt{\mu} = 0.44$) for $\overline{U} = 0.05$ and $Re = 6 \times 10^5$. (f_h&f_θ are the in-air and f_h^*&f_θ^* are the in-water natural frequencies)

f_h =82 [Hz], f_θ =396 [Hz]		$\alpha_o = 2^o$	$\alpha_o = 8^o$	$\alpha_o = 15^o$	$\alpha_o = 20^o$
f_h^* [Hz]	Exp.	36	36	N/A	N/A
	Num.	35	37	37	34
f_θ^* [Hz]	Exp.	187	192	N/A	N/A
	Num.	197	195	200	193

first in-water natural bending and twisting frequencies vary slightly with the angle of attack. The dependence of the in-water natural frequencies with angle of attack is non-monotonic and is associated with viscous FSI effects caused by the change in the pressure distribution and wake patterns with the angle of attack.

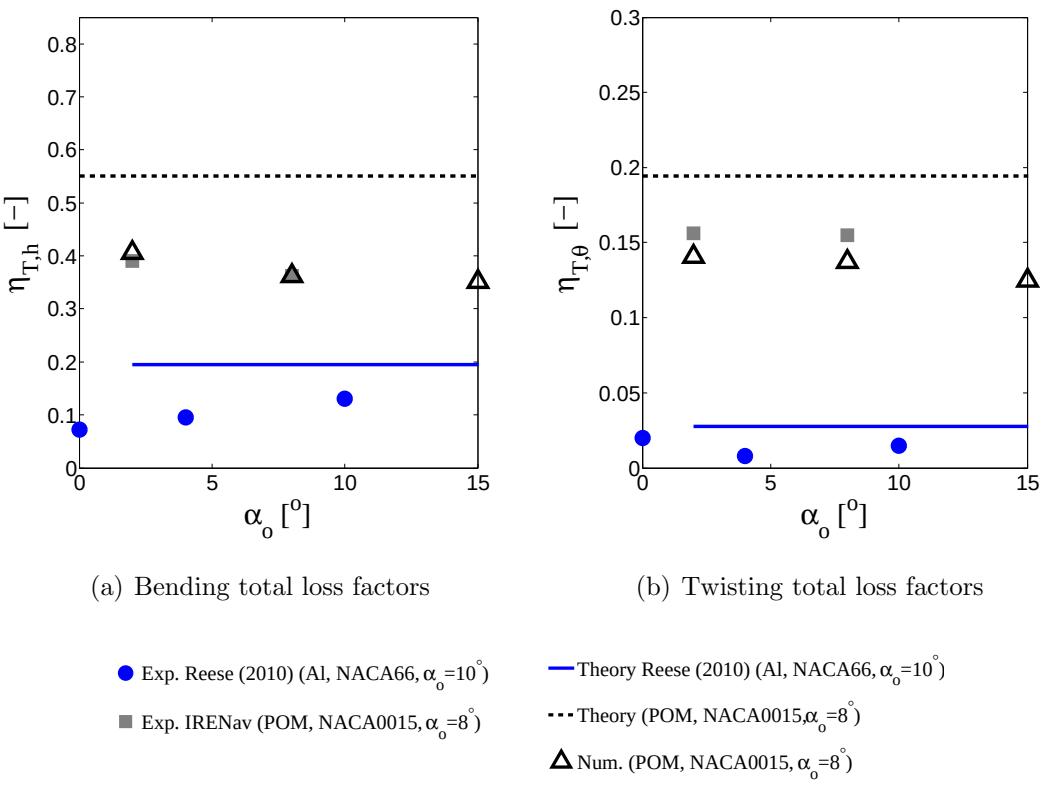

(a) Bending total loss factors

(b) Twisting total loss factors

Figure 4.23: Comparison of the measured and predicted total loss factor (η_T) vs. angle of attack (α_o) for the (a) bending, and (b) twisting deformations for the flexible NACA0015 POM hydrofoil at $\overline{U} = 0.05$ and $Re = 6 \times 10^5$. Also shown are experimental measurements of an aluminum NACA66 hydrofoil from *Reese* (2010), as well as the theoretical predictions by using Eqs. (4.4) - (4.5) according to *Blake and Maga* (1975). Note that viscous FSI simulations are only shown for the POM NACA0015 hydrofoil.

4.3.3 Total loss factors of the bending and twisting responses

Figure 4.23 shows a comparison of the total loss factors (η_T) obtained using the viscous FSI solver, the inviscid, uncoupled mode linear theory given by *Blake and Maga* (1975) in Eqs. (4.4) and (4.5), as well as the experimental studies of the NACA0015 POM hydrofoil from both IRENav and of the NACA66 aluminum hydrofoil from *Reese* (2010) with varying angle of attack. Note that viscous FSI simulations are only shown for the NACA0015 POM hydrofoil. The predicted viscous results compare well with the experimental measurements for the NACA0015 POM hydrofoil. The inviscid linear theory (as given in Eqs. (4.4)-(4.5)) overestimates the total loss

factor for both hydrofoils. Inviscid theory also cannot predict the variation of the total loss factor with the angle of attack caused by viscous effects such as flow separation and unsteady vortex shedding. Similar to the results shown in Section 4.2, the over-prediction of η_T by the inviscid linear theory is more severe for the lighter POM NACA0015 hydrofoil than the heavier aluminum NACA66 hydrofoil studied by *Reese* (2010). At post-stall (i.e., $\alpha_o = 20^o$), the results of bending and twisting deformations become over-damped locally as shown in Fig. 4.21. However, the mobility peak power down method is only valid for an under-damped system, where the total damping coefficients (ζ_T) < 1 (i.e., $\eta_T < 2$). Therefore, Fig. 4.23 shows the total loss factors for $2^o \leq \alpha_o \leq 15^o$ only.

4.3.4 Wake structures

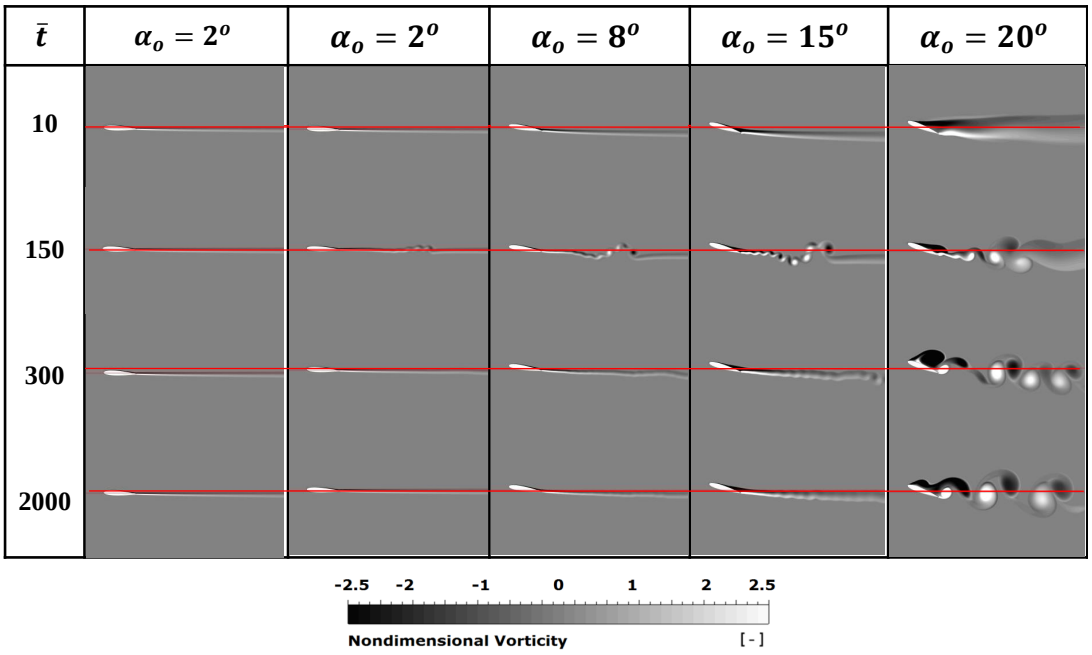

Figure 4.24: Snapshots of the predicted non-dimensional vorticity ($\varpi = \omega b/U$) contours of the flow around a flexible POM (bottom row) NACA0015 hydrofoil at different time instances ($\bar{t} = t\omega_\theta$) for $\alpha_o = 2 \sim 20^\circ$ at $\overline{U} = 0.05$ and $Re = 6 \times 10^5$. The horizontal lines pass through the elastic axis of the undeformed hydrofoil.

The snapshots of the predicted vorticity contours of viscous FSI simulations at selected time instances ($\overline{t} = t\omega_\theta$) for a flexible NACA0015 hydrofoil for $\alpha_o = 2 \sim 20^\circ$ at $\overline{U} = 0.05$ and $Re = 6 \times 10^5$ are shown in Fig. 4.24. The results in Fig. 4.24 show that unsteady vortex sheddings can be observed even for the $\alpha_o = 2^o$ case during the transient responses phase prior to reaching static equilibrium. At $\alpha_o = 15^o$, the flow is nearly fully separated due to increases in the effective angle of attack caused by the clockwise flow-induced twisting motion. At $\alpha_o = 20^o$, the flow is fully separated. It should be noted that the vortex shedding frequency of the flexible hydrofoil shown in Fig. 4.24 is close to lock-in with the first in-water natural bending frequency at $\alpha_o = 20^o$, which results in large-scale fluctuations in loads and deformation, as shown in the time-histories plot in Fig. 4.21.

CHAPTER V

Flow-induced bend-twist coupling

For lightweight, flexible hydrofoils, the natural frequencies and total loss factors vary with the inflow velocity and the angle of attack, as shown in chapter IV. For the lightweight, flexible POM NACA0015 hydrofoil, in particular, there are flow-induced bend-twist coupling effects because the elastic axis differs from the center of pressure. Section 5.1 shows the predicted uncoupled and coupled in-water natural frequencies and total loss factors for varying reduced velocity, angle of attack, and relative mass ratio. The experimental measurements of the flexible POM NACA0015 hydrofoil are obtained by the French Naval Academy Research Institute (IRENav). Section 5.2 presents the parametric maps for a wide range of common materials to compare the inviscid, uncoupled and coupled mode of in-water natural frequencies and fluid loss factors of NACA0015 foils.

5.1 Influence of the flow-induced bend-twist coupling on the natural frequency and total loss factor

Flow-induced bend-twist coupling can affect the hydrofoil's dynamics, as there are non-zero off-diagonal terms of the fluid damping and disturbing force/moment (i.e., C_{12}^T, C_{21}^T, K_{12}^T, and K_{21}^T in Eqs. (2.7) - (2.8)). In addition to the off-diagonal terms induced in the linear potential-flow solution, the location of the center of pressure

(CP) and the lift force may change with the effective angle of attack (α_{eff}) due to viscous effects such as transition, separation, and interaction with shed vortices in the wake. This section examines how the system's in-water natural frequencies and total loss factors depend on the flow-induced bend-twist coupling effects.

5.1.1 NACA0015 model setup

Numerical simulations are performed on a cantilevered, rectangular NACA0015 hydrofoil made of five different materials: low-density polyethylene (LDPE), nylon, polyacetate (POM), aluminum, and stainless steel materials.

Table 5.1: Model parameters for the NACA0015 hydrofoil with five different materials

Material	LDPE	Nylon	POM	Aluminum	Stainless Steel
ρ_s $[kg/m^3]$	920	1000	1480	2700	7480
E_s $[GPa]$	0.3	2	3	69	180
ν_s [-]	0.35	0.39	0.35	0.34	0.31
$\sqrt{\mu}$ [-]	0.35	0.36	0.44	0.59	0.99
α_o $[^o]$	8	8	$2 \sim 20$	8	8
Re [-]	2.35×10^5	6.02×10^5	$3 \times 10^5 \sim 12 \times 10^5$	21.22×10^5	20.37×10^5
$\overline{U}$ [-]	0.05	0.05	$0.02 \sim 0.1$	0.05	0.05
a [-]	0	0	0	0	0
x_θ [-]	-0.16	-0.16	-0.16	-0.16	-0.16
r_θ [-]	0.44	0.44	0.44	0.44	0.44
c $[m]$	0.1	0.1	0.1	0.1	0.1
s $[m]$	0.192	0.192	0.192	0.192	0.192
τ/c [-]	0.15	0.15	0.15	0.15	0.15
$\zeta_{s,h}$ [%]	2	3	2	0.2	0.1
$\zeta_{s,\theta}$ [%]	2	3	2	0.2	0.1
$\Omega = f_h/f_\theta$ [-]	0.21	0.21	0.21	0.21	0.21
f_h [Hz]	32	83	82	291	279
f_θ [Hz]	156	399	395	1398	1342

Table 5.1 lists the range of the model parameters for the NACA0015 hydrofoil with five different materials. To investigate the influence of the reduced velocity ($\overline{U}$)

and the angle of attack (α_o), the POM NACA0015 hydrofoil is used, varying the $\overline{U}$ (by changing U) and α_o. To investigate the influence of the relative mass ratio (μ), the $\overline{U}$ is fixed by varying the inflow velocity (U) proportional with changing stiffness for the five different materials (e.g. LDPE, nylon, POM, aluminum, stainless steel). The relative mass ratio ($\mu = m/(\pi\rho_f b^2)$) is varied by changing the solid density (ρ_s) and fixing both the fluid density (ρ_f) and the semi-chord length. Following *Leissa* (1969), the first in-air natural bending and twisting frequencies (ω_h and ω_θ) can be calculated as shown in Eqs. (5.1)-(5.2) for a rectangular, homogeneous, isotropic, cantilevered plate with an aspect ratio (AR) of 1.92.

$$\omega_h = 2\pi f_h = \frac{\beta_1}{s}\sqrt{\frac{E_s(\tau/s)^2}{12(1-\nu_s^2)\rho_s}}, \tag{5.1}$$

$$\omega_\theta = 2\pi f_\theta = \frac{\beta_2}{s}\sqrt{\frac{E_s(\tau/s)^2}{12(1-\nu_s^2)\rho_s}}, \tag{5.2}$$

where β_1= 2.88 and β_2=13.84, and therefore $\Omega = \omega_h/\omega_\theta = \beta_1/\beta_2 = 0.21$ for all materials. β_1 and β_2 are found by matching the in-air natural frequencies of the POM NACA0015 hydrofoil measured at the French Naval Academy Research Institute. In Eqs. (5.1)-(5.2), τ is the maximum thickness.

The FSI responses of the flexible hydrofoils are modeled by solving a two-degrees-of-freedom (2-DOF) equation of motion (EOM) using both an inviscid fluid model and a viscous fluid model via the LHC method discussed in chapter II. The same viscous formulation was previously used in *Young et al.* (2012), *Chae et al.* (2013), and *Akcabay et al.* (2014). The flow is assumed to be fully turbulent and $2.35\times10^5 \leq Re \leq 20.37\times10^5$ for the cases shown in this section. In addition, the foil is assumed to be deeply submerged so free surface and cavitation effects are not relevant. This chapter uses the same medium NACA0015 mesh (about 929,000 nodes and 910,000 elements) and time step size of $\Delta t = T_h^*/480$ (i.e., $\overline{\Delta t} = \Delta t\omega_\theta = 0.16$) as shown in chapter IV to solve the fluid dynamics.

5.1.2 In-water natural frequencies

For the time domain (TD) viscous FSI simulations, the natural frequencies are determined by inspecting the peaks of the frequency spectra obtained via fast Fourier transform (FFT) of the time-histories. In addition, frequency domain (FD) inviscid solutions of natural frequencies are obtained by solving the eigenvalue problem.

The inviscid, uncoupled mode in-water natural bending and twisting frequencies (f^*_{h-UM} and $f^*_{\theta-UM}$) based on *Theodorsen* (1935)'s approach are expressed as:

$$f^*_{h-UM} = f_h\sqrt{\frac{\mu}{\mu+1}}, \tag{5.3}$$

$$f^*_{\theta-UM} = f_\theta\sqrt{\frac{\mu r_\theta^2 - 2C(k)e\overline{U}^2}{\mu r_\theta^2 + (\frac{1}{8}+a^2)}}, \tag{5.4}$$

where the superscript "$*$" is used for the in-water natural frequencies.

The inviscid, coupled mode in-water natural bending and twisting frequencies (f^*_h and f^*_θ) of the frequency domain (FD) inviscid solutions are obtained by assuming a solution in the form of:

$$\mathbf{X} = \mathbf{A}e^{\lambda t} \quad \text{with} \quad (\mathbf{M}_\text{s} + \mathbf{M}^T)\ddot{\mathbf{X}} + (\mathbf{C}_\text{s} + \mathbf{C}^T)\dot{\mathbf{X}} + (\mathbf{K}_\text{s} + \mathbf{K}^T)\mathbf{X} = 0. \tag{5.5}$$

In Eq. (5.5), $\mathbf{A}$ is a constant vector that depends on the initial bending or twisting deformation, and λ is the eigenvalue of the EOM. In general, the eigenvalues have real and imaginary terms in the form of:

$$\lambda = -\zeta_T\omega_n \pm i\omega_n\sqrt{1-\zeta_T^2} = Re(\lambda) \pm iIm(\lambda), \tag{5.6}$$

where ζ_T is the total damping coefficient and ω_n is the undamped natural frequency.

The equation for the damped in-water natural frequency (ω_d) is shown in Eq. (5.9).

$$\omega_n = \sqrt{Re(\lambda)^2 + Im(\lambda)^2} \tag{5.7}$$

$$\zeta_T = \frac{-Re(\lambda)}{\omega_n} = \frac{\eta_T}{2} \tag{5.8}$$

$$\omega_d = \omega_n\sqrt{1-\zeta_T^2} = Im(\lambda) \tag{5.9}$$

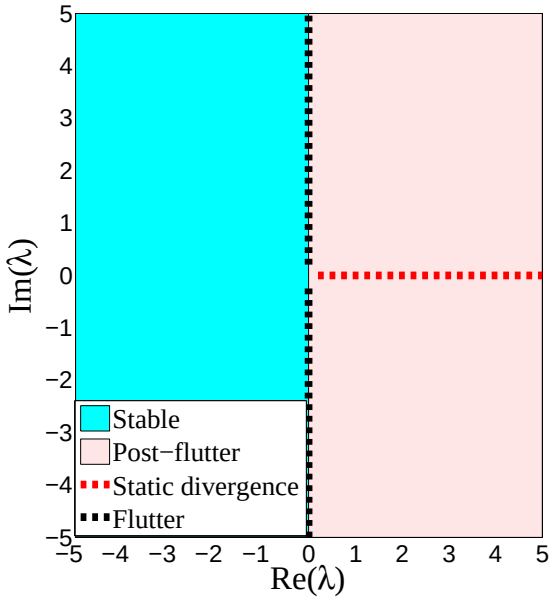

Figure 5.1: Stability zones of the system as a function of the real and imaginary components of the eigenvalues of the fully coupled inviscid FSI equations shown in Eq. 5.5.

Based on the inviscid eigenvalue calculation, the plot shown in Fig. 5.1 classifies the stability regions as follows:

- When $Re(\lambda)<0$, $\zeta_T > 0$, the system is stable, as shown in Fig. 5.2(a), as the deformation will damp out with time. When $Re(\lambda)> 0$, $\zeta_T < 0$, the system is unstable, as shown in Figs. 5.2(b) and 5.2(d). When $Re(\lambda)= 0$, $\zeta_T = 0$, the system is neutral, as shown in Figs. 5.2(c).

- When $Im(\lambda)=0$ or $\zeta_T \geq 1$, there is no oscillation frequency; on the other hand, when $Im(\lambda)\neq 0$, there is an oscillation frequency.

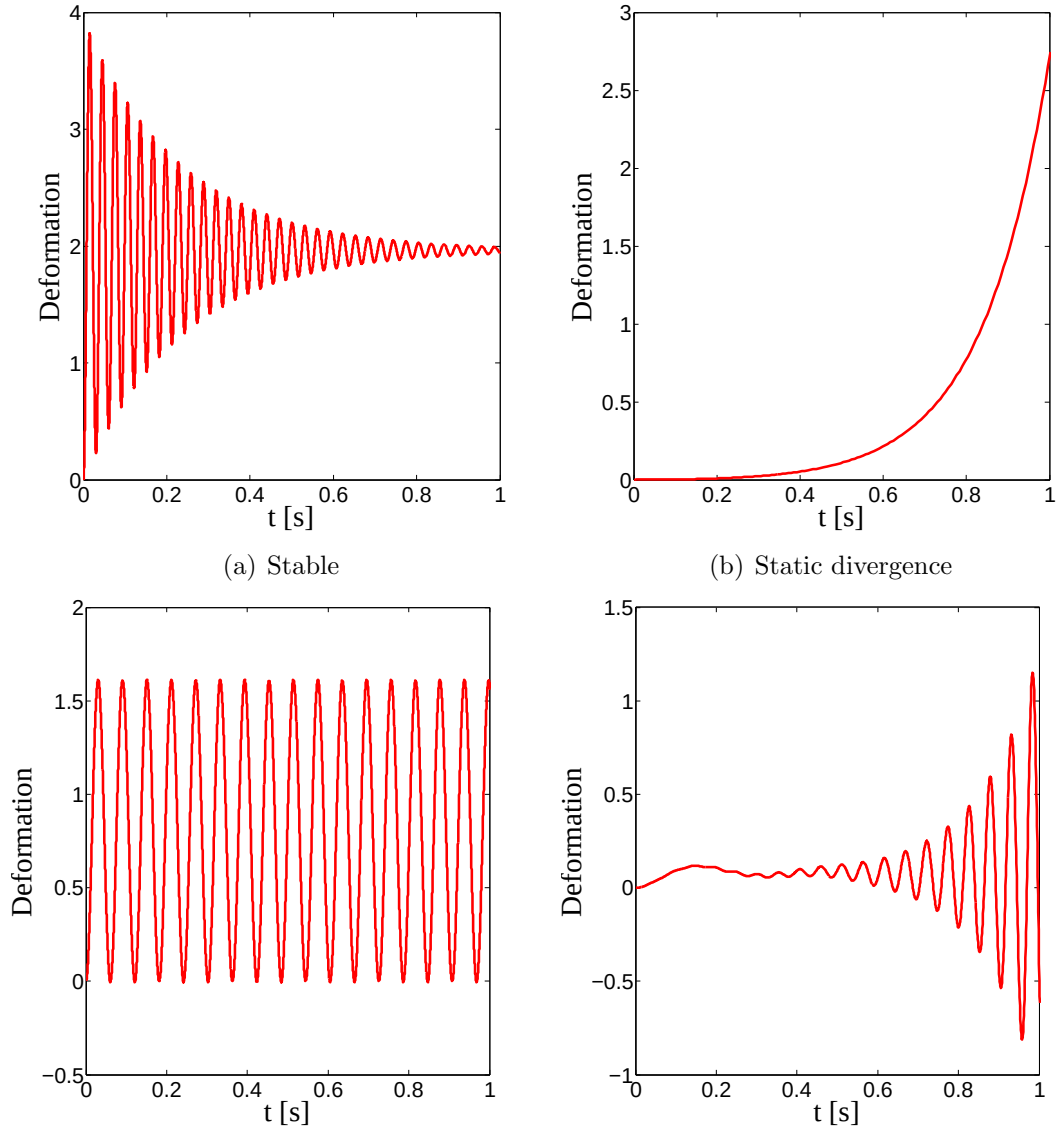

(a) Stable

(b) Static divergence

(c) Flutter

(d) Post-flutter

Figure 5.2: Examples of the system response in (a) stable, (b) static divergence, (c) flutter, and (d) post-flutter conditions.

- When $Re(\lambda)>0$ & $Im(\lambda)=0$, the system undergoes a static divergence as shown in Fig. 5.2(b), as the deformation will grow exponentially with time without oscillation.

- When $Re(\lambda)=0$ & $Im(\lambda)\neq 0$, $\zeta_T = 0$, the system is at the flutter boundary as shown in Fig. 5.2(c), where the system oscillates with constant amplitude and frequency.

- When $Re(\lambda)>0$ & $Im(\lambda)\neq 0$, $\zeta_T < 0$, the system is at post-flutter as shown in Fig. 5.2(d); the deformations increase with time and with oscillations.

5.1.3 The effects of the reduced velocity ($\overline{U}$)

Figure 5.3 shows the effect of the reduced velocity ($\overline{U}$) on the first in-water natural bending and twisting frequencies (f_h^* & f_θ^*) for the flexible NACA0015 POM hydrofoil with $\sqrt{\mu} = 0.44$ at $\alpha_o = 8°$ (the Re is between $3 \times 10^5 \sim 19 \times 10^5$).

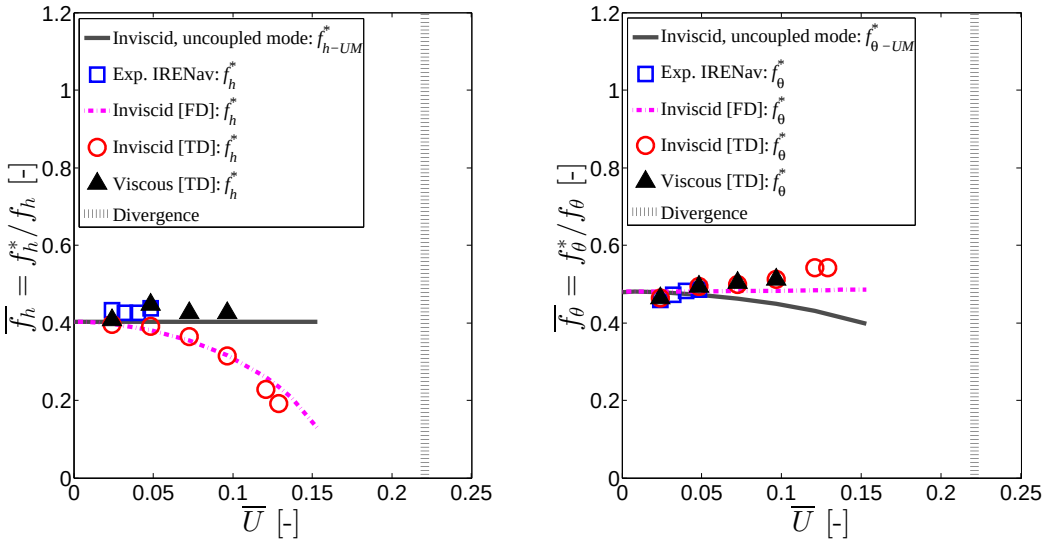

(a) Bending frequencies (b) Twisting frequencies

Figure 5.3: Effect of reduced velocity ($\overline{U}$) on the non-dimensional (a) bending frequencies and (b) twisting frequencies of the flexible NACA0015 POM hydrofoil ($\sqrt{\mu}$=0.44) at $\alpha_o = 8^o$ and $\overline{U} = 0.02 \sim 0.15$ (i.e., $Re = 3 \times 10^5 \sim 19 \times 10^5$). FD is the frequency domain solution and TD is the time domain solution.

The reduced velocity ($\overline{U} = U/\omega_\theta b$) is varied by changing the inflow velocity and fixing the foil geometry and material. The experimental results are from IRENav (*Chae et al.*, 2015a). It should be noted that for the both inviscid and viscous FSI solutions in a time domain (TD), the numerical simulations were iterated to get the initial oscillation reduced frequency (k).

For the flexible NACA0015 POM hydrofoil with the characteristics shown in Table 5.1, the non-dimensional static divergence velocity ($\overline{U_d}$) is calculated as 0.22, as shown

in Fig. 5.3, by using the static force balance relation given in Eq. (5.10).

$$\overline{U_d} = \frac{U_d}{\omega_\theta b} = \sqrt{\frac{k_\theta}{2\pi\rho_f e b^4 \omega_\theta^2}} = \sqrt{\frac{\mu r_\theta^2}{1+2a}} \tag{5.10}$$

As shown in Fig. 5.3, the in-water natural frequencies (f_h^* & f_θ^*) are lower than in-air natural frequencies (f_h & f_θ) due to the added mass effect. The IRENav experimental measurements agree well with time domain (TD) viscous predictions, and both results show that while f_h^* is practically independent of $\overline{U}$, f_θ^* tended to increase with $\overline{U}$, which is consistent with the frequency spectra shown in Figs. 4.6 and 4.12. On the other hand, both the frequency domain (FD) and time domain (TD) inviscid solutions predict that f_h^* decreases as $\overline{U}$ increases, which does not agree with experimental measurements nor with TD viscous predictions. The difference between inviscid and viscous solutions of f_h^* increases as $\overline{U}$ increases. The inviscid, uncoupled mode theory $f_{\theta-UM}^*$ in Eq. (5.4) decreases with $\overline{U}$, and it is opposite to the trend observed in the FD and TD inviscid solutions, and differ from the TD viscous simulations to experimental measurements. The inviscid, uncoupled mode solution differs from the inviscid, coupled mode solution because the flow-induced bend-twist coupling terms (C_{12}^T, C_{12}^T, and K_{12}^T in Eqs. (2.7) - (2.8)) are neglected in the derivation of Eqs. (5.3) and (5.4). The FD inviscid solution also differs from the TD inviscid solution due to the application of harmonic motion assumption in the FD solution, which is not true in the low mass ratio (μ) regime due to the high fluid damping. The difference between the TD inviscid and TD viscous solutions is mainly caused by viscous effects (e.g. separation and interaction of shed vortices with body motion) on the fluid damping ($\mathbf{C}^T$) and stiffness ($\mathbf{K}^T$) terms.

Figure 5.4 compares bending and twisting total loss factors ($\eta_{T,h}$ and $\eta_{T,\theta}$, respectively) with varying reduced velocity ($\overline{U} = 0.02 \sim 0.07$, $Re = 3 \times 10^5 \sim 9 \times 10^5$) on the flexible NACA0015 POM hydrofoil ($\sqrt{\mu} = 0.44$) at $\alpha_o = 8^o$. $\eta_{T,h}$ and $\eta_{T,\theta}$ are

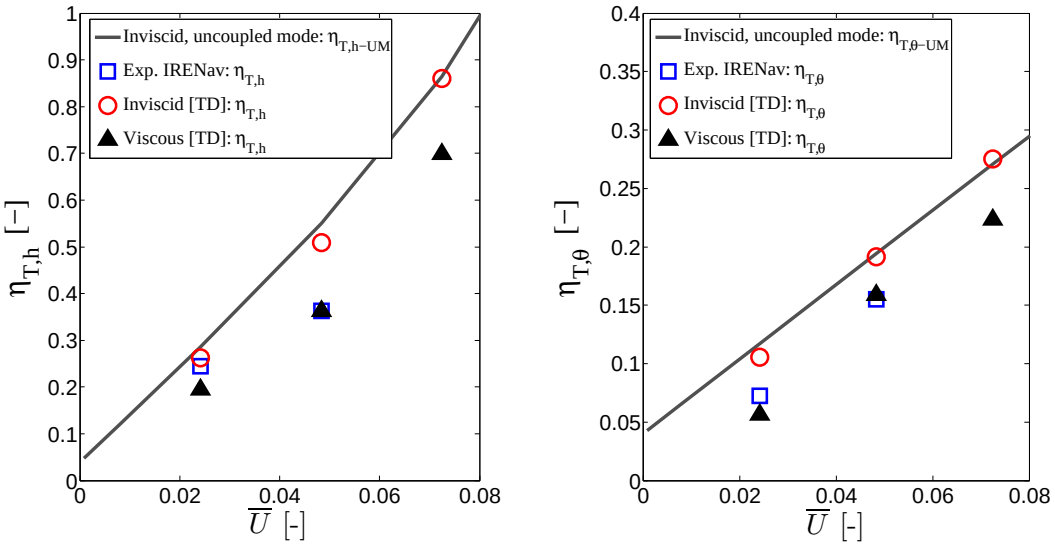

(a) Bending total loss factors

(b) Twisting total loss factors

Figure 5.4: Effect of reduced velocity ($\overline{U}$) on the non-dimensional in-water (a) bending total loss factors and (b) twisting total loss factors of the flexible NACA0015 POM hydrofoil ($\sqrt{\mu}$=0.44) at $\alpha_o = 8^o$ and $\overline{U} = 0.02 \sim 0.07$ (i.e., $Re = 3\times10^5 \sim 9 \times 10^5$). Note that TD is the time domain solution.

measured by the mobility peak power down method (shown in chapter IV of section 4.1.5) for all the methods except for the inviscid, uncoupled mode theory, which is given in Eqs. (4.4) and (4.5).

As noted in chapter IV, the total loss factors increase with $\overline{U}$ because the fluid damping force is proportional to $\overline{U}$. In Fig. 5.4, the predicted total loss factors from the TD viscous simulations are in good agreement with experimental results, which is the same as those shown in chapter IV. Moreover, the total loss factors of both the inviscid, uncoupled mode theory by *Blake and Maga* (1975) and the TD inviscid FSI solution are similar, and both over-predicted the actual total loss factors compared to both the TD viscous FSI and experimental results. This is because of two factors: 1) the wake consists of point vortices, which may not behave as assumed in *Theodorsen* (1935), i.e. the wake is not aligned with the inflow, dynamic interactions between the vortices in the wake, and body motion leads to changes in vortex shedding frequencies and induced velocity on the foil, leading to the development of viscous

dissipation; and 2) the actual center of pressure (CP) may come closer to the EA instead of the aerodynamic center (AC) (i.e., $c/4$ from the foil's leading-edge) assumed in *Theodorsen* (1935). It should be noted that over-prediction of the total loss factors is a risk as the structure may undergo earlier fatigue, longer settling time, higher noise and vibration. All of these effects will modify e, d, k, and $C(k)$, which, in turn, affect the inviscid natural frequencies and total loss factors predictions.

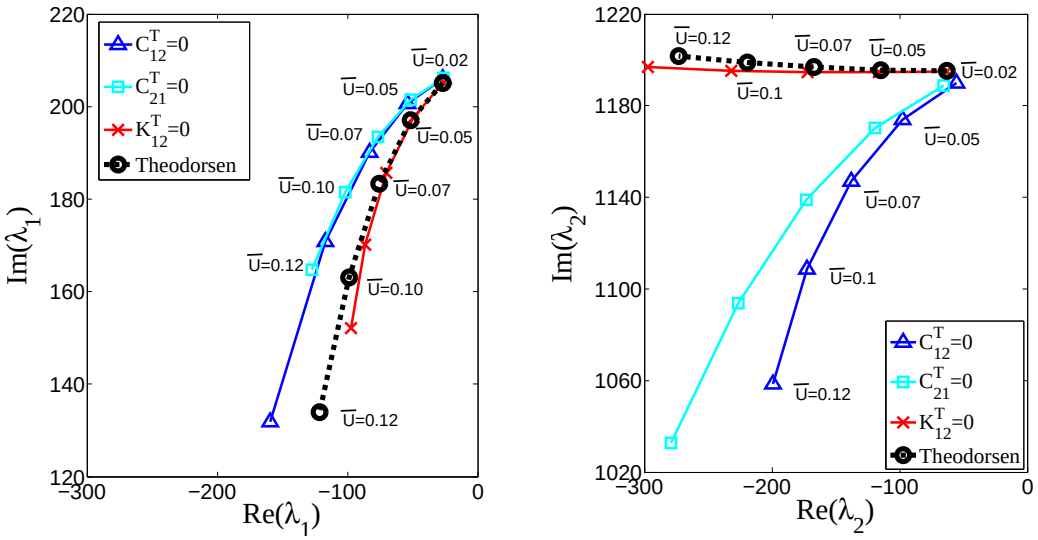

(a) Bending mode (b) Twisting mode

Figure 5.5: Influence of reduced velocity ($\overline{U}$) on the root locus plot of (a) bending eigenvalues and (b) twisting eigenvalues of the inviscid frequency domain (FD) solution for the flexible NACA0015 POM hydrofoil ($\sqrt{\mu} = 0.44$) with $\overline{U} = 0.02 \sim 0.12$ (i.e., $Re = 3 \sim 15 \times 10^5$). Theodorsen corresponds to the FD inviscid solution with all terms included. $C_{12}^T = 0$, $C_{21}^T = 0$, and $K_{12}^T = 0$ corresponds to when the respective flow-induced bend-twist coupling terms are set to zero for the FD inviscid solution.

To better understand the influence of the flow-induced bend-twist coupling terms, Fig. 5.5 shows the root locus plot of the bending and twisting eigenvalues of Eq. (5.6) for the flexible NACA0015 POM hydrofoil ($\sqrt{\mu}$=0.44) with $\overline{U} = 0.02 \sim 0.12$ (i.e., $Re = 3 \sim 15 \times 10^5$). It should be noted that the bending and twisting eigenvalues correspond to the solution of the frequency domain (FD) inviscid problem shown in Eq. 5.5. Theodorsen corresponds to the FD inviscid solution with all the terms

included, while $C_{12}^T = 0$, $C_{21}^T = 0$, and $K_{12}^T = 0$ correspond to the FD inviscid solutions when the respective flow-induced bend-twist coupling terms are set to zero in Eqs. (2.7) and (2.8) that makes up Theodorsen's solution.

The results in Fig. 5.5 show that the in-water damped natural frequencies, ω_d (i.e., imaginary eigenvalues, $Im(\lambda)$, in Eq. (5.9)) vary with $\overline{U}$ as shown in Fig. 5.3; for the FD inviscid (Theodorsen) solution, the in-water damped natural bending frequency (f_h^*) as represented by $Im(\lambda_1)$ decreases with higher $\overline{U}$, and the in-water natural twisting frequency (f_θ^*) as represented by $Im(\lambda_2)$ increases with higher $\overline{U}$, which are consistent with the results shown in Fig. 5.3. The results also show that increasing $\overline{U}$ increases the bending and twisting total damping coefficients ($\zeta_{T,h}$, $\zeta_{T,\theta}$) (i.e., a function of the real and imaginary eigenvalues as shown in Eq. (5.8)), which are consistent with the results shown in Fig. 5.4. Note that $\zeta_{T,h}$ increases 20% faster with $\overline{U}$ than $\zeta_{T,\theta}$ as indicated by the differences in the slope of the bending mode corresponding to the twisting mode of Theodorsen's solution in Figs. 5.4 and 5.5.

In Fig. 5.5, if the inviscid flow-induced bend-twist coupling damping terms are ignored (i.e., $\mathrm{C}_{12}^T = 0$ or $\mathrm{C}_{21}^T = 0$ in Eq. (2.7)) with varying $\overline{U}$, the eigenvalues of the bending mode (λ_1) and the twisting mode (λ_2) are different, compared with the FD inviscid fully coupled solution (i.e., *Theodorsen*), particularly for λ_2. The results in Fig. 5.5 show that the flow-induced bend-twist coupling damping terms highly affect the in-water natural frequencies and total loss factors. The results in Fig. 5.5 further show that when the inviscid stiffness related to the flow-induced bend-twist coupling terms is ignored (i.e., $\mathrm{K}_{12}^T = 0$ in Eq. (2.8)), λ_1 and λ_2 are slightly underestimated compared to *Theodorsen* (1935)'s solution. These findings imply that the disturbing force components of the flow-induced bend-twist coupling terms also affect the in-water natural frequencies and total loss factors. As shown in Eqs. (2.7) and (2.8), the flow-induced bend-twist coupling terms (C_{12}^T, C_{21}^T, and K_{12}^T) depend on $\overline{U}$, as well as e, d, k, and $C(k)$, where the values will differ for inviscid vs. viscous flows, resulting

in different trends of the natural frequencies and total loss factors, as observed in Figs. 5.3 and 5.4.

5.1.4 The effect of the angle of attack (α_o)

Figure 5.6 shows the effect of angle of attack (α_o) on the first in-water natural bending and twisting frequencies (f_h^* & f_θ^*) for the flexible NACA0015 POM hydrofoil ($\sqrt{\mu} = 0.44$) at $\overline{U} = 0.05$ (i.e., $Re = 6 \times 10^5$).

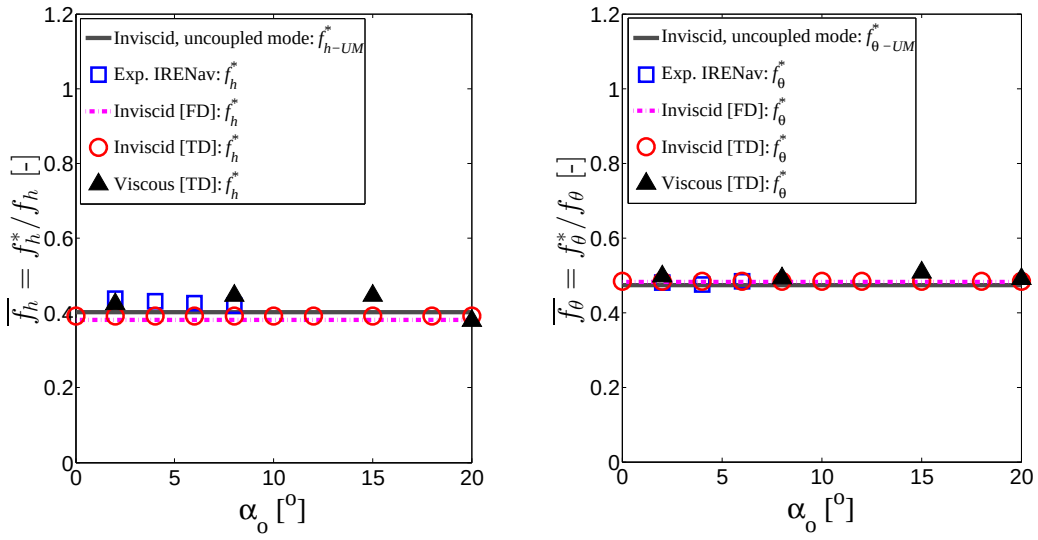

(a) Bending frequencies (b) Twisting frequencies

Figure 5.6: Effect of angle of attack (α_o) on the non-dimensional in-water (a) bending frequencies and (b) twisting frequencies of the flexible NACA0015 POM hydrofoil ($\sqrt{\mu}$=0.44) at $\overline{U} = 0.05$ (i.e., $Re = 6 \times 10^5$). Note that FD is the frequency domain solution and TD is the time domain solution.

Generally, the TD viscous results of the in-water natural frequencies are in good agreement with IRENav experimental results shown in *Chae et al.* (2015a), and both vary slightly with the angle of attack. Both the FD and TD inviscid solutions are similar, and a slight difference can be observed with the inviscid, uncoupled mode theory frequencies given by Eqs. (5.3) and (5.4). Nevertheless, the inviscid solutions compared fairly well with the experimental and TD viscous results, as the results are for $\overline{U} = 0.05$, where the flow-induced bend-twist effects corresponding to the off-

diagonal terms on the damping and stiffness are small. Note that C^T is proportional to $\overline{U}$ and K^T is proportional to $\overline{U}^2$ in Eqs. (2.7) and (2.8).

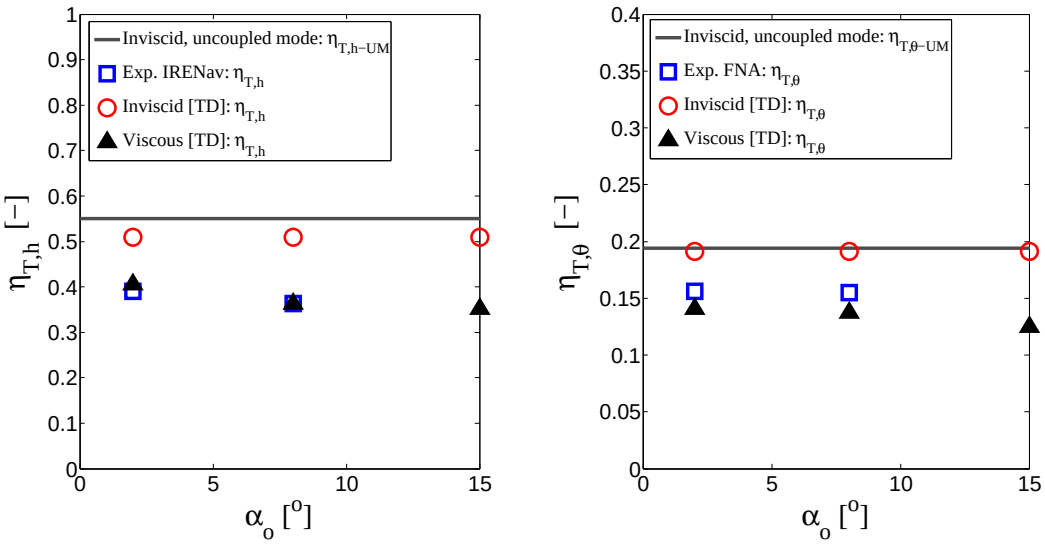

(a) Bending total loss factors

(b) Twisting total loss factors

Figure 5.7: Effect of angle of attack (α_o) on the non-dimensional (a) bending total loss factors and (b) twisting total loss factors of the flexible NACA0015 POM hydrofoil ($\sqrt{\mu}$=0.44) at $\overline{U} = 0.05$ (i.e., $Re = 6 \times 10^5$). Note that TD is the time domain solution.

Similarly, Fig. 5.7 compares the predicted and measured bending and twisting motions of total loss factors (η_T) with varying angle of attack (α_o) for the same flexible NACA0015 POM hydrofoil ($\sqrt{\mu} = 0.44$) at $\overline{U} = 0.05$ (i.e., $Re = 6 \times 10^5$). As with the results shown in Fig. 5.4, there is a good comparison between TD viscous numerical and experimental total loss factors. Both the inviscid, uncoupled mode theory (given in Eqs. (5.3) and (5.4)) and the TD inviscid solution significantly overestimate the total loss factors for the flexible NACA0015 POM hydrofoil ($\sqrt{\mu}$=0.44) with different angles of attack. The results show that both the in-water natural frequencies and the total loss factors have a weak dependence on the angle of attack (α_o), which is expected, as the dependence is due to the higher order nonlinear viscous effects.

5.1.5 The effect of the relative mass ratio ($\sqrt{\mu}$)

Figure 5.8 shows the effect of the relative mass ratio ($\sqrt{\mu}$) on the first in-water natural bending and twisting frequencies (f_h^* & f_θ^*) for the flexible NACA0015 hydrofoil at $\alpha_o = 8^o$ and $\overline{U} = 0.05$. Note that the different $\sqrt{\mu}$ values are obtained by changing the solid material from stainless steel ($\sqrt{\mu}$= 0.99) to low-density polyethylene (LDPE) ($\sqrt{\mu}$= 0.35) for a given fluid (ρ_f=1000kg/m^3). Detailed simulation parameters are listed in Table 5.1. To investigate the influence of the relative mass ratio ($\sqrt{\mu}$), the $\overline{U}$ is fixed at 0.05 (where experimental data is available for IRENav) by varying the inflow velocity (U) proportional with changing stiffness (and hence ω_θ) for the five different materials (e.g. LDPE, nylon, POM, aluminum , and stainless steel).

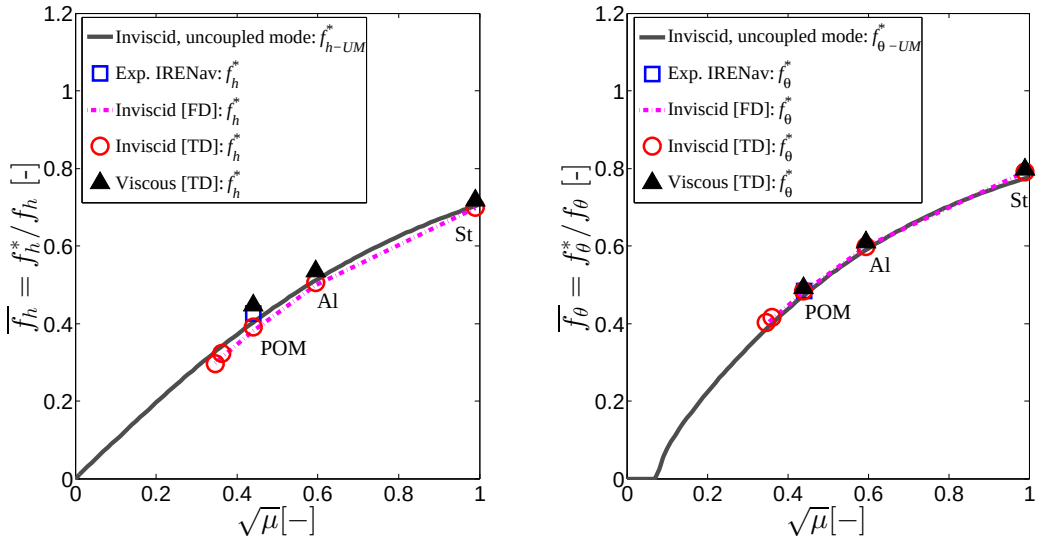

(a) Bending frequencies

(b) Twisting frequencies

Figure 5.8: Effect of relative mass ratio ($\sqrt{\mu}$) on the non-dimensional in-water (a) bending frequencies and (b) twisting frequencies of the flexible NACA0015 hydrofoil at $\alpha_o = 8^o$ and $\overline{U} = 0.05$. Note that FD is the frequency domain solution and TD is the time domain solution. Note also that the different $\sqrt{\mu}$ values are obtained by changing the solid material from stainless steel ($\sqrt{\mu}$= 0.99) to low-density polyethylene (LDPE) ($\sqrt{\mu}$= 0.35) for a given fluid (ρ_f=1000kg/m^3). The reduced velocity ($\overline{U} = U/(\omega_\theta b)$) is fixed by changing the inflow velocity for a given foil's in-air natural twisting frequency.

The results in Fig. 5.8 show that inviscid, uncoupled mode theory and both

FD and TD inviscid solutions are similar to the TD viscous solution of the in-water natural bending and twisting frequencies at $\sqrt{\mu} \simeq 1$. With decreasing $\sqrt{\mu}$, the differences between inviscid, uncoupled mode and coupled mode results are increased slightly due to changes induced by the flow-induced bend-twist coupling term. Figure 5.8 also shows that the in-water to in-air natural frequency ratios ($\overline{f_h} = f_h^*/f_h$ and $\overline{f_\theta} = f_\theta^*/f_\theta$) decrease rapidly with lower $\sqrt{\mu}$, and approach zero as $\sqrt{\mu} \to 0$, as shown in Eqs. (5.3) and (5.4).

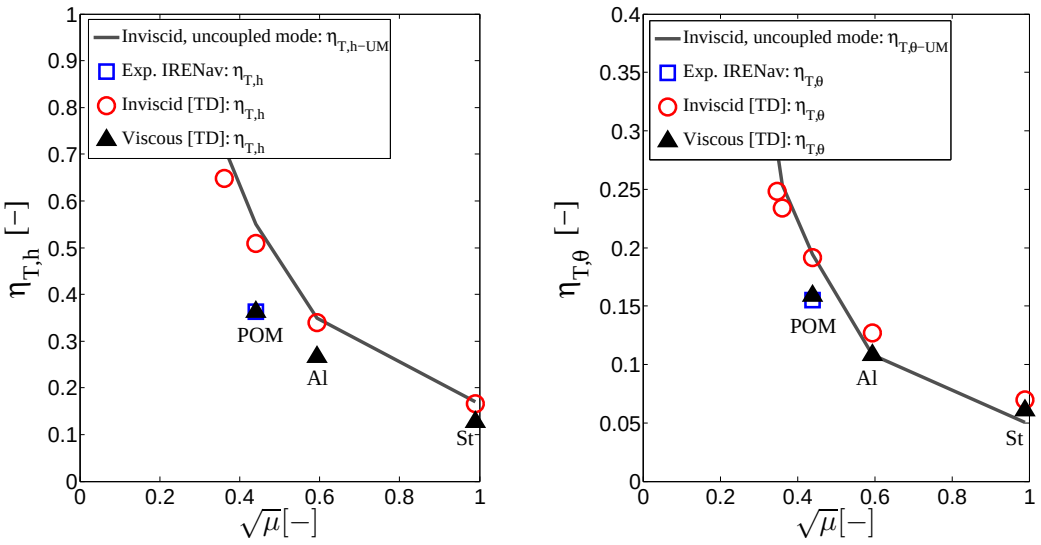

(a) Bending total loss factors

(b) Twisting total loss factors

Figure 5.9: Effect of relative mass ratio ($\sqrt{\mu}$) on the non-dimensional (a) bending total loss factors and (b) twisting total loss factors of the flexible NACA0015 hydrofoil at $\alpha_o = 8^o$ and $\overline{U} = 0.05$. Note that TD is the time domain solution. Note also that the different $\sqrt{\mu}$ values are obtained by changing the solid material from stainless steel ($\sqrt{\mu}$= 0.99) to low-density polyethylene (LDPE) ($\sqrt{\mu}$= 0.35) for a given fluid (ρ_f=1000kg/m^3). The reduced velocity ($\overline{U} = U/(\omega_\theta b)$) is fixed by changing the inflow velocity for a given foil's in-air natural twisting frequency.

Figure 5.9 compares the total loss factors (η_T) for bending and twisting motions with the varying relative mass ratio ($\sqrt{\mu}$) for the same flexible NACA0015 hydrofoil at $\alpha_o = 8^o$ and $\overline{U} = 0.05$. The results in Fig. 5.9 show that the inviscid, uncoupled mode theory and TD inviscid solutions again overestimate the total loss factors compared with experimental and TD viscous solutions; the overestimation increases

with decreasing $\sqrt{\mu}$. It should be noted that the rapid increase of the total loss factor with decreasing $\sqrt{\mu}$ is the reason why flutter, which occurs when total effective fluid and solid damping is zero, is usually not a great concern for hydrofoils compared to airfoils. The high damping also leads to non-harmonic, rapidly decaying oscillations, resulting in the transition from fluter to dynamic divergence to static divergence.

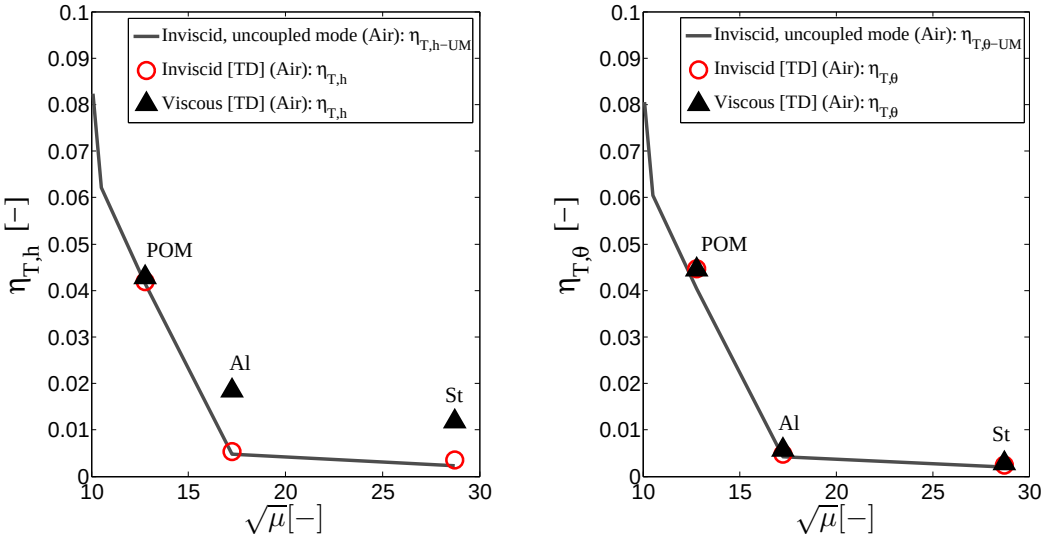

(a) Bending total loss factors

(b) Twisting total loss factors

Figure 5.10: Effect of relative mass ratio ($\sqrt{\mu}$) on the non-dimensional (a) bending total loss factors and (b) twisting total loss factors of the flexible NACA0015 airfoil at $\alpha_o = 8^o$ and $\overline{U} = 0.05$. Note that TD is the time domain solution. Note also that the different $\sqrt{\mu}$ values are obtained by changing the solid material from stainless steel to POM for a given fluid (ρ_f=1.185kg/m^3). The reduced velocity ($\overline{U} = U/(\omega_\theta b)$) is fixed by changing the inflow velocity for a given foil's in-air natural twisting frequency.

To contrast the in-water vs. in-air response, Fig. 5.10 compares the total loss factors (η_T) for bending and twisting motions with the varying relative mass ratio ($\sqrt{\mu}$) for the same flexible NACA0015 foil shown in Fig. 5.9, but in air (with ρ_f=1.185 kg/m^3) at $\alpha_o = 8^o$ and $\overline{U}$=0.05. Notice that the foils are in air so $\sqrt{\mu} > 10$ for the range of materials considered. The results in Fig. 5.10 show that the total loss factors predicted by inviscid, uncoupled mode theory are similar to that predicted by the TD viscous solutions for airfoils, and η_T values of airfoils are approximately an order

of magnitude less than those of hydrofoils. Therefore, the flow-induced bend-twist coupling effects in air are very small compared to those in water due to smaller fluid loads. Moreover, when $\sqrt{\mu}$ increases, the inviscid, uncoupled mode theory slightly underestimates the total loss factor for the bending motion compared with TD viscous solutions (i.e., the inviscid theory is conservative.), which is the opposite of the trend observed for the hydrofoils, as shown in Fig. 5.9.

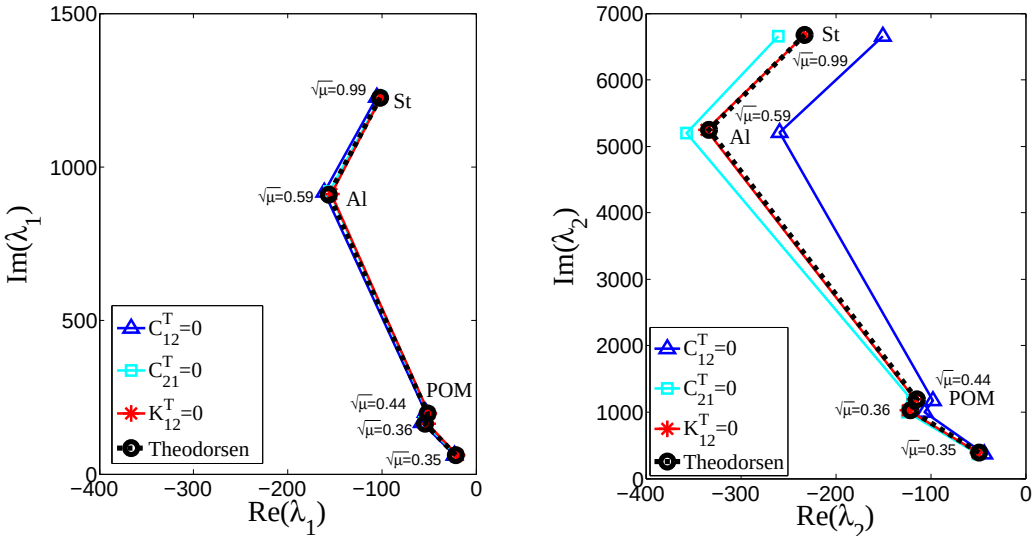

(a) Bending mode (b) Twisting mod

Figure 5.11: Influence of relative mass ratio ($\sqrt{\mu}$) on the root locus plot of (a) bending mode and (b) twisting mode for the flexible NACA0015 hydrofoil with $\overline{U} = 0.05$. Note that the different $\sqrt{\mu}$ values are obtained by changing the solid material from stainless steel ($\sqrt{\mu}$= 0.99) to low-density polyethylene (LDPE) ($\sqrt{\mu}$= 0.35) for a given fluid (ρ_f=1000kg/m^3). Theodorsen corresponds to the FD inviscid solution with all terms included. $C_{12}^T = 0$, $C_{21}^T = 0$, and $K_{12}^T = 0$ correspond to when the respective flow-induced bend-twist coupling terms are set to zero for the FD inviscid solution.

To better understand the influence of the flow-induced bend-twist coupling terms with relative mass ratio ($\sqrt{\mu}$), Fig. 5.11 shows the root locus plot of bending and twisting eigenvalues (for the flexible NACA0015 hydrofoil with $\overline{U} = 0.05$) correspond to the solution of the frequency domain (FD) inviscid problem shown in Eq. 5.5. As with the results shown in Fig. 5.5, all the simulations for bending and twisting eigenvalues with varying relative mass ratio considered in this work are for stable

systems, as $Re(\lambda_1) < 0$ & $Re(\lambda_2) < 0$. The results in Fig. 5.11 show that as $\sqrt{\mu} \to 0$, both $Re(\lambda)$ & $Im(\lambda) \to 0$, which implies $\zeta_T \to 1$ and f_h^* & $f_\theta^* \to 0$. The results also show that when the inviscid damping and stiffness of the flow-induced bend-twist coupling terms are ignored (i.e., $C_{12}^T = 0$, $C_{21}^T = 0$, or $K_{12}^T = 0$ in Eqs. (2.7) and (2.8)) with varying relative mass ratio ($\sqrt{\mu}$), λ_1 and λ_2 change only slightly from the Theodorsen's solution due to the low $\overline{U}$, which in turn, affect the natural frequencies and total loss factors as shown in Figs. 5.8 and 5.9. It should be noted that for high values of $\overline{U}$, the flow-induced bend-twist coupling terms would have more impact on the eigenvalues, and hence the in-water natural frequencies and loss factors, as shown in Figs. 5.3 and 5.4.

5.2 Influence of the flow-induced bend-twist coupling on the parametric maps

To illustrate the influence of the flow-induced bend-twist coupling terms and hydrodynamic damping effects, comparisons of the inviscid, undamped uncoupled mode natural frequency ratios (f_{h-UM}^*/f_h, $f_{\theta-UM}^*/f_\theta$ in Eqs. (5.3) - (5.4)) and inviscid, damped coupled mode natural frequency ratios (f_h^*/f_h, f_θ^*/f_θ in Eq. (5.9)) for a rectangular, cantilevered NACA0015 foils with $\nu_s = 0.35$, $C(k) = 0.5$, and $\overline{U} = 0.07$ are shown in Figs. 5.12 and 5.13 for a wide range of common materials.

The rectangular, cantilevered NACA0015 hydrofoils are assumed to be structurally homogeneous and materially isotropic, and they are assumed to be cantilevered at their root. As the mass ratio (μ) decreases, f_{h-UM}^*, $f_{\theta-UM}^*$, f_h^*, and f_θ^* decrease for a given $\overline{U}$. When $\sqrt{\mu} \leq 0.5$ & $\overline{U} \geq 0.05$, the discrepancy between inviscid, uncoupled mode and coupled mode in-water natural frequencies increases, which are consistent with the results shown in Fig. 5.8 (i.e., $f_{h-UM}^* \geq f_h^*$ and $f_{\theta-UM}^* \leq f_\theta^*$).

Figures 5.14 and 5.15 show the influence of flow-induced bend-twist coupling of

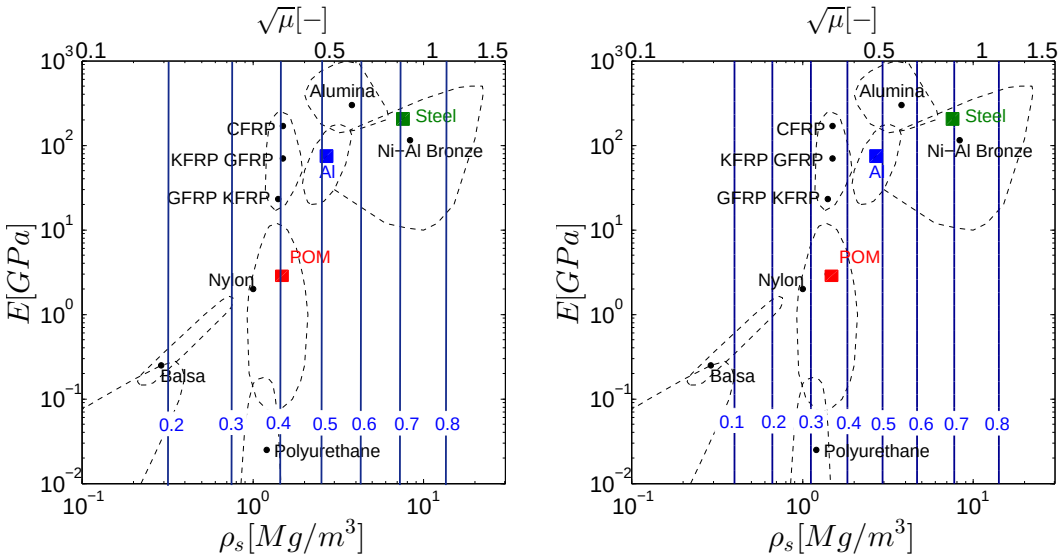

(a) Inviscid, uncoupled mode of f^*_{h-UM}/f_h (b) Inviscid, coupled mode of f^*_h/f_h

Figure 5.12: Comparison of the natural bending frequency ratios of (a) the inviscid, undamped uncoupled mode (f^*_{h-UM}/f_h) solution obtained using Eq. (5.3) and (b) the inviscid, damped coupled mode (f^*_h/f_h) solution obtained using Eq. (5.9) for a rectangular, cantilevered NACA0015 hydrofoils made of different materials with $\nu_s = 0.35$, $C(k) = 0.5$, and $\overline{U} = 0.07$.

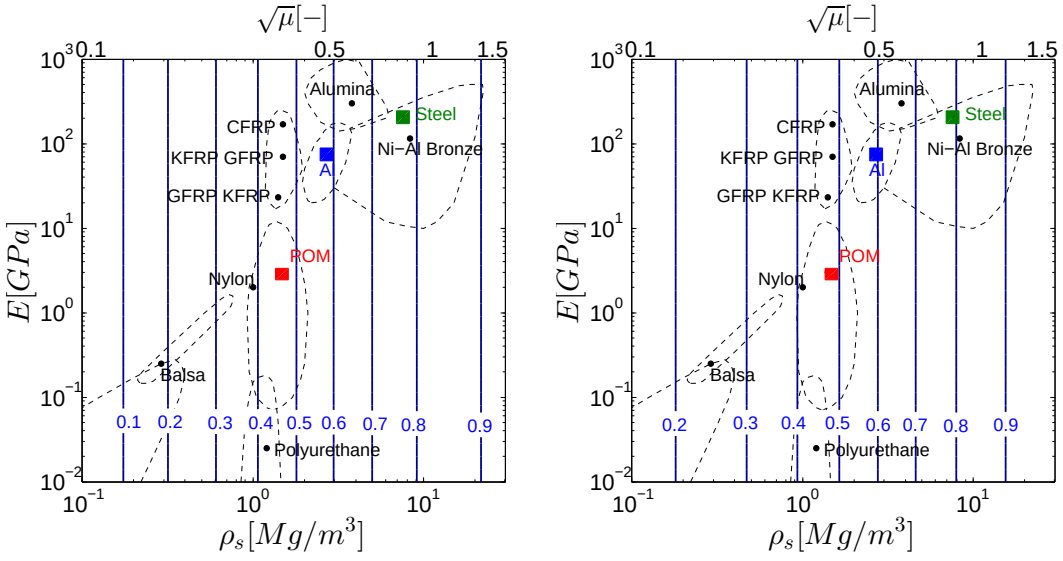

(a) Inviscid, uncoupled mode of $f^*_{\theta-UM}/f_\theta$ (b) Inviscid, coupled mode of f^*_θ/f_θ

Figure 5.13: Comparison of the natural twisting frequency ratios of (a) the inviscid, undamped uncoupled mode ($f^*_{\theta-UM}/f_\theta$) solution obtained using Eq. (5.4) and (b) the inviscid, damped coupled mode (f^*_θ/f_θ) solution obtained using Eq. (5.9) for a rectangular, cantilevered NACA0015 hydrofoils made of different materials with $\nu_s = 0.35$, $C(k) = 0.5$, and $\overline{U} = 0.07$.

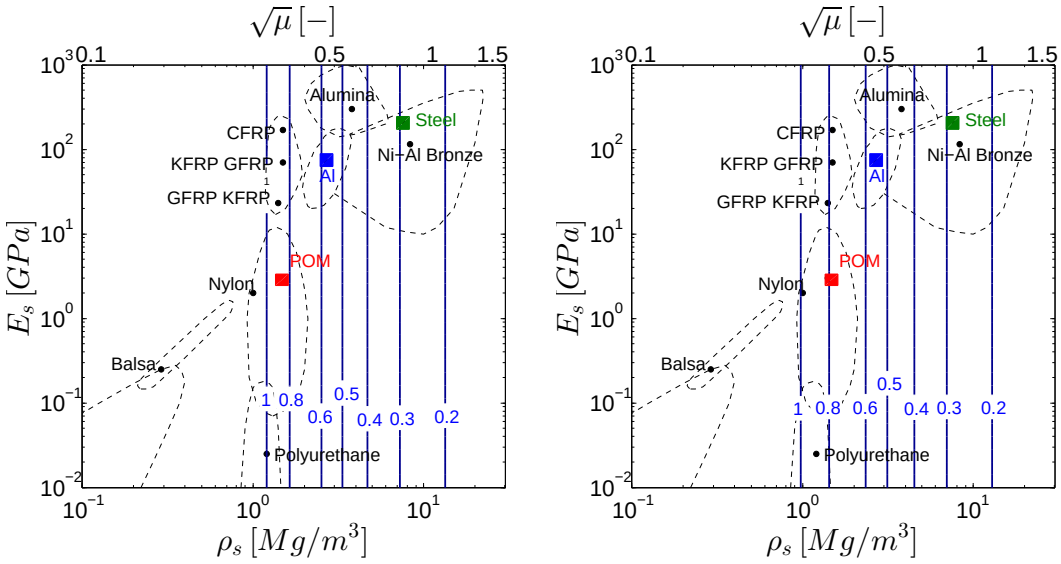

(a) Inviscid, uncoupled mode of $\eta_{f,h-UM}$ (b) Inviscid, coupled mode of $\eta_{f,h}$

Figure 5.14: Comparison of the bending fluid loss factors of (a) the inviscid, uncoupled mode ($\eta_{f,h-UM}$) solution obtained using Eq. (4.4) and (b) the inviscid, coupled mode ($\eta_{f,h}$) solution obtained using Eq. (5.8) for a rectangular, cantilevered NACA0015 hydrofoils made of different materials with $\nu_s = 0.35$, $C(k) = 0.5$, and $\overline{U} = 0.07$.

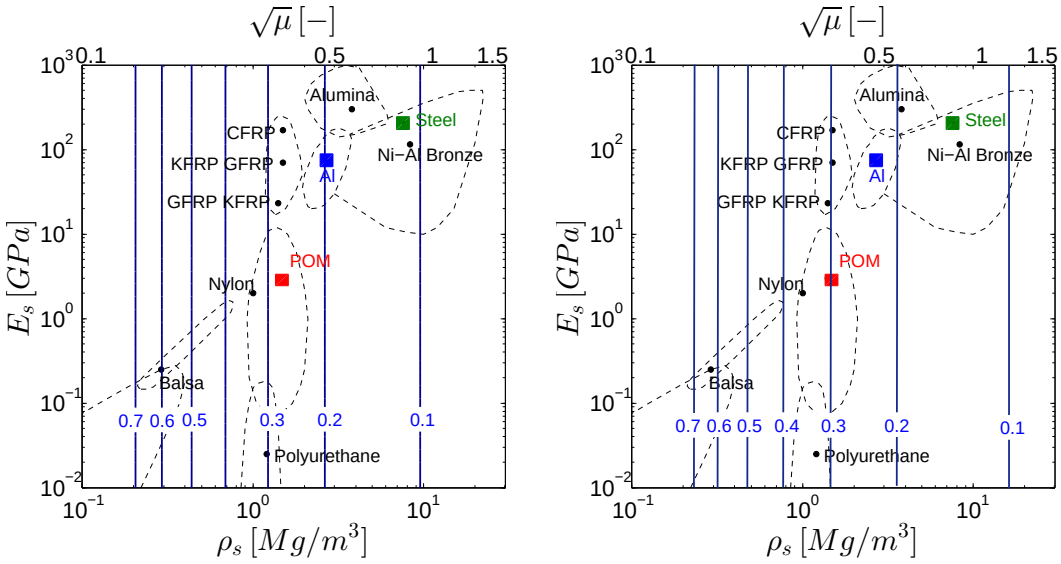

(a) Inviscid, uncoupled mode of $\eta_{f,\theta-UM}$ (b) Inviscid, coupled mode of $\eta_{f,\theta}$

Figure 5.15: Comparison of the twisting fluid loss factors of (a) the inviscid, uncoupled mode ($\eta_{f,\theta-UM}$) solution obtained using Eq. (4.5) and (b) the inviscid, coupled mode ($\eta_{f,\theta}$) solution obtained using Eq. (5.8) for a rectangular, cantilevered NACA0015 hydrofoils made of different materials with $\nu_s = 0.35$, $C(k) = 0.5$, and $\overline{U} = 0.07$.

the fluid loss factors (by comparing the inviscid, uncoupled mode ($\eta_{f,h-UM}$ & $\eta_{f,\theta-UM}$ in Eqs. (4.4) - (4.5)) and inviscid, coupled mode ($\eta_{f,h}$ & $\eta_{f,\theta}$ in Eq. (5.8))) solutions for a rectangular, cantilevered NACA0015 foils made of different materials with $\nu_s = 0.35$, $C(k) = 0.5$, and $\overline{U} = 0.07$. The results in Figs. 5.14 and 5.15 show that as the μ decreases, $\eta_{f,h-UM}$, $\eta_{f,\theta-UM}$, $\eta_{f,h}$, and $\eta_{f,\theta}$ increase for a given $\overline{U}$. Inviscid, uncoupled and coupled mode results are similar, but some difference can still be observed for $\sqrt{\mu} \leq 0.5$ & $\overline{U} \geq 0.05$. In addition, as mentioned when presenting the results shown in Fig. 5.8, both inviscid results over-predicted the actual total loss factors compared to viscous results and experimental measurements for $\sqrt{\mu} < 1$; and this overestimation will increases with decreasing μ and increasing $\overline{U}$. The results in this and the precious chapter show that the impacts of the flow-induced bend-twist coupling terms increase with higher $\overline{U}$ and lower μ, and the flow-induced bend-twist coupling terms are affected by viscous effects via e, d, and $C(k)$ due to flow separations, shed vorticies, and interaction with body motion.

CHAPTER VI

Conclusion and future work

6.1 Conclusion

Rectangular, cantilevered, flexible foils with chordwise rigid and spanwise bending and twisting deformations in incompressible and viscous flow were studied via combined numerical and experimental modeling. The unsteady Reynolds-average Navier-Stokes (uRANS) fluid solver was coupled with a two degrees-of-freedom (2-DOF) solid solver through an efficient and stable loose hybrid coupling (LHC) method introduced by *Young et al.* (2012), *Chae et al.* (2013), and *Akcabay and Young* (2014). A commercial computational fluid dynamics (CFD) solver (i.e., *ANSYS-CFX* (2011)) was used for viscous simulations to solve the uRANS equation with the $k-\omega$ shear stress transport ($k-\omega$ SST) turbulence model. A fully coupled (FC) inviscid fluid-structure interaction (FSI) model was also developed based on the potential flow theory following *Theodorsen* (1935).

For the FSI response and stability boundary, the results of viscous simulations were compared with predictions obtained using the inviscid fully coupled (FC) FSI model, as well as published experimental data given in *Woolston and Castile* (1951) and *Besch and Liu* (1971). The NACA16-010 foil geometry, which was the same as that used in the experimental study in *Woolston and Castile* (1951), was used in viscous and inviscid simulations for the stability boundary study presented in chapter

III. The operating conditions were $Re = 3.05\times10^5-4.27\times10^6$ and $\sqrt{\mu} = 0.3-4.18$. In general, as the fluid density increased for a given solid density, the relative mass ratio ($\sqrt{\mu}$) decreased, which in turn led to a decrease of the critical reduced flutter velocity and the reduced divergence velocity. The following major findings were observed:

- The frequency domain (FD) linear potential theory solution predicted higher flutter velocities than measured for cases with low relative mass ratios ($\sqrt{\mu} < 3$). This is because in the low relative mass ratio regime, the fluid forces were comparable to the solid forces, and the relative contribution of viscous effects increased, which led to strong viscous interactions. In particular, as the fluid damping and inertial forces increased with higher fluid density, the flow-induced oscillation would be quickly damped out, leading to non-harmonic motion, and hence greater error between linear FD inviscid predictions (that assume harmonic motion) and the experimental results.

- The governing instability mode varied with $\sqrt{\mu}$:

  - for $\sqrt{\mu}<$ 1, static divergence was the governing instability mode as the fluid disturbing force dominated and became equal to, or greater than, the solid restoring force. Divergence can occur even if the elastic axis (EA) is at the aerodynamic center (AC), which contradicts linear potential theory predictions for thin symmetric foils. This is because, in reality, the center of pressure (CP) may not coincide with the AC; the CP will vary with the angle of attack and flow conditions due to viscous and flow separation effects, which will lead to a non-zero moment arm between the EA and the CP, even if the EA is at the AC, leading to the possibility of divergence, which could only be captured by viscous FSI models;

  - for $1 \leq \sqrt{\mu} < 2$, dynamic divergence was the governing instability mode, which could only be captured by viscous nonlinear FSI models because

the response is non-harmonic and the oscillation frequencies decrease with time as the mean deformation amplitude increases; and

  - for $\sqrt{\mu} \geq 2$, flutter was the governing instability mode and the difference between inviscid and viscous models became relatively small, and both predictions agreed well with experimental measurements.

- The predicted flutter velocity, flutter frequency, and divergence velocity obtained using the viscous LHC simulations compared well with the measured values from previously published experimental data. Even though the inviscid FC method with a time domain (TD) solution technique provided a reasonable approximation of the flutter and static divergence velocities at a much lower computational cost compared to the viscous LHC method, viscous LHC simulations in a time domain were recommended to predict the dynamic response and stability boundary to capture nonlinear viscous FSI effects.

For the flow-induced vibration studies shown in chapter IV, the simulations were performed on a cantilevered NACA0015 hydrofoil made of a polyacetate (POM) material with a chord length, $c = 2b$, of 0.1 m and a span length, s, of 0.192 m, with reduced velocity (by changing inflow velocity) ranging from $\overline{U} = 0.02 \sim 0.1$ (i.e., $Re = 3 \sim 12 \times 10^5$) and angles of attack ranging from $\alpha_o = 2 \sim 20^o$. The model was validated by comparing the numerical predictions with experimental measurements conducted inside a cavitation tunnel at the French Naval Academy Research Institute (IRENav). Comparisons between the current numerical and experimental results with prior published results of other flexible hydrofoils were also shown. The results indicated that:

- Numerical viscous FSI predictions of both the first in-water natural bending and twisting frequencies and total loss factors compared well with available experimental measurements.

- While the first in-water natural bending frequency was mostly independent of the inflow velocity, the first in-water natural twisting frequency tended to increase with the inflow velocity for the flexible NACA0015 POM hydrofoil due to changes in the system stiffness and damping caused by viscous effects including separation, generation, and interaction of vortices with foil bending and twisting motion.

- The inviscid, linear, uncoupled mode theory provided in *Blake and Maga* (1975) tended to over-predict the total loss factors. The over-prediction increases with increasing $\overline{U}$ and with decreasing μ, and was found to be as high as 52% for bending and 25% for twisting for the current flexible NACA0015 POM hydrofoil. The over-prediction is mostly caused by neglecting of the flow-induced bend-twist coupling terms and viscous FSI effects, which are more significant for cases with low μ and high $\overline{U}$. Viscous effects could modify the location of center of pressure, the trajectory of the wake sheet, vortex shedding frequencies, phase lag caused by the wake vortices, and resulting interaction with foil motions, which could lead to lower the fluid damping than predicted using inviscid theory.

- At $\alpha_o = 20^o$, the reduced vortex shedding frequency was approximately $k_{\text{vs,rigid}}$ =2.5 for the rigid hydrofoil, and $k_{\text{vs, flexible}}$=1.3 for the flexible hydrofoil (in lock-off region) with varying reduced velocity (i.e., varying inflow velocity). In other words, the vortex shedding frequency of the rigid foil was much higher than that of the flexible foil. In the lock-in region, the vortex shedding frequencies of the flexible hydrofoil snapped into the first in-water natural bending frequencies, which led to amplified vibrations and load fluctuations.

- Both experimental and numerical results indicated that both the in-water natural frequencies and loss factors varied slightly with the angle of attack due to viscous effects, but the variations were small compared to those observed with

$\overline{U}$.

For the flow-induced bend-twist coupling study shown in chapter V, numerical simulations were performed on cantilevered NACA0015 hydrofoils with a chord length, c, of 0.1 m, and a span length, s, of 0.192 m, which were made of low-density polyethylene (LDPE), nylon, polyacetate (POM), aluminum, and stainless steel materials corresponds to relative mass ratios of $\sqrt{\mu} = m/(\pi\rho_f b^2) = 0.35 \sim 0.99$. In the simulations, water is the operating fluid. The reduced velocity ranged from $\overline{U} = U/(\omega_\theta b) = 0$ (rigid) to 0.15, Reynolds numbers from $Re = 3\times10^5 \sim 2.0\times10^6$, and angles of attack from $\alpha_o = 2°$, 8°, 15°, and 20°. Specifically, the following results were observed:

- The inviscid, uncoupled mode theory, and both the frequency domain (FD) and the time domain (TD) inviscid solutions under-predicted the first in-water natural bending frequencies compared to the time domain (TD) viscous solutions; the difference between inviscid and viscous predictions increased with increasing $\overline{U}$ and lower μ.

- As μ decreases toward zero, the in-water natural frequencies also reduce rapidly toward zero while the damping coefficient increases rapidly toward one. Consequently, the structural response time lengthens, and the flow-induced vibrations will be rapidly damped out, which is why the governing instability mode goes from flutter for $\sqrt{\mu} > 2$ to dynamic divergence for $1 \leq \sqrt{\mu} < 2$ to static divergence for $\sqrt{\mu} < 1$.

- The inviscid, uncoupled mode theory and the TD inviscid solver overestimated the total loss factors, and this overestimation increased with higher $\overline{U}$ or with lower $\sqrt{\mu}$ at low mass ratios (i.e., $\sqrt{\mu} < 1$, the region for most hydrofoils). The opposite was observed for $\sqrt{\mu} > 1$, the region for most airfoils. It should be noted that over-predicting the total loss factors could be dangerous as it could lead to designs that were more prone to earlier fatigue, longer settling time,

increased noise and vibration, as well as earlier flutter and greater deformation and load amplification resonance.

- The flow-induced bend-twist coupling terms in the fluid damping and stiffness are found to affect natural frequencies and loss factors. The impacts of the flow-induced bend-twist coupling terms increase with higher $\overline{U}$ and lower μ. The flow-induced bend-twist coupling terms are responsible for the difference between inviscid, uncoupled and coupled mode, TD inviscid FC and TD viscous LHC solutions. Notice that the flow-induced bend-twist coupling terms are affected by viscous effects via e, d, and $C(k)$ due to flow separations, shed vorticies, and interaction with body motion.

6.2 Future work

In this thesis, we developed a new loose hybrid coupling (LHC) method for viscous FSI simulations (*Young et al.*, 2012; *Chae et al.*, 2013; *Akcabay et al.*, 2014). The LHC method subtracts the potential flow estimation of the FSI force from both the left hand side and right hand side of the equations of motion to accelerate the convergence and to avoid the numerical instability issues. The LHC method was validated for numerical simulations for the dynamic response and stability boundary of flexible hydrofoils in incompressible and viscous flow. A related study by *Akcabay et al.* (2015) has shown that subtracting potential flow estimate of the added mass term on both side of the equation is critical to expanding the numerical stability boundary by avoiding the virtual added mass instability for incompressible flows (*Young*, 2007, 2008; *Xiao and Batra*, 2012). However, the importance of also subtracting the fluid damping and fluid disturbing force terms from both sides of the equation of motion is not clear as their effects on the numerical stability should be small, and they will increase the computational costs due to the need to iterate to determine the reduced

frequency (k). Hence, in Fig. 6.1, we compare the LHC method and the added mass (AM) method, where the later only subtracted the potential flow estimate of the fluid added mass terms, $\mathbf{M}^T$, from both the sides of the equations of motion.

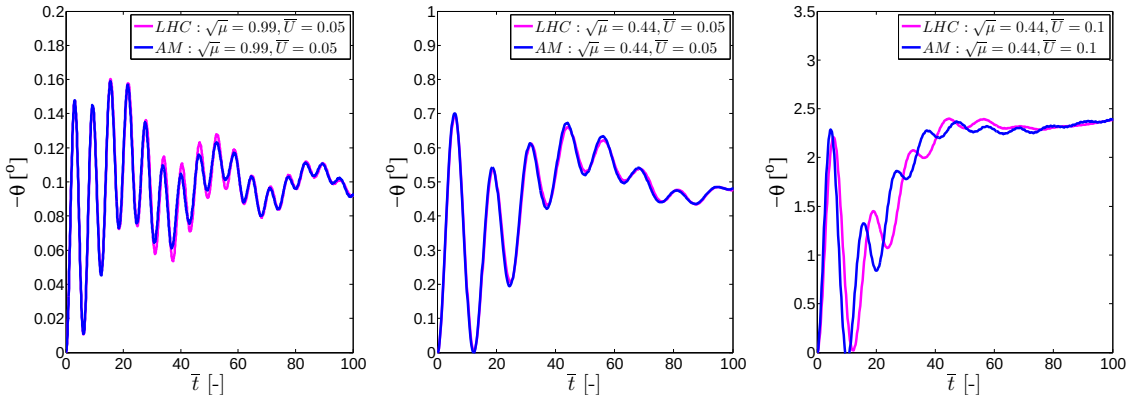

(a) θ at $\sqrt{\mu} = 0.99$ & $\overline{U} = 0.05$ (b) θ at $\sqrt{\mu} = 0.44$ & $\overline{U} = 0.05$ (c) θ at $\sqrt{\mu} = 0.44$ & $\overline{U} = 0.1$

Figure 6.1: Comparison of the time-histories of twisting deformations (θ) with different viscous FSI methods on the NACA0015 stainless steel and POM hydrofoils at $\alpha_o = 8^o$ with (a) $\sqrt{\mu} = 0.99$ & $\overline{U} = 0.05$, (b) $\sqrt{\mu} = 0.44$ & $\overline{U} = 0.05$, and (c) $\sqrt{\mu} = 0.44$ & $\overline{U} = 0.1$. Note that $\overline{t} = t\omega_\theta$ is the non-dimensional time.

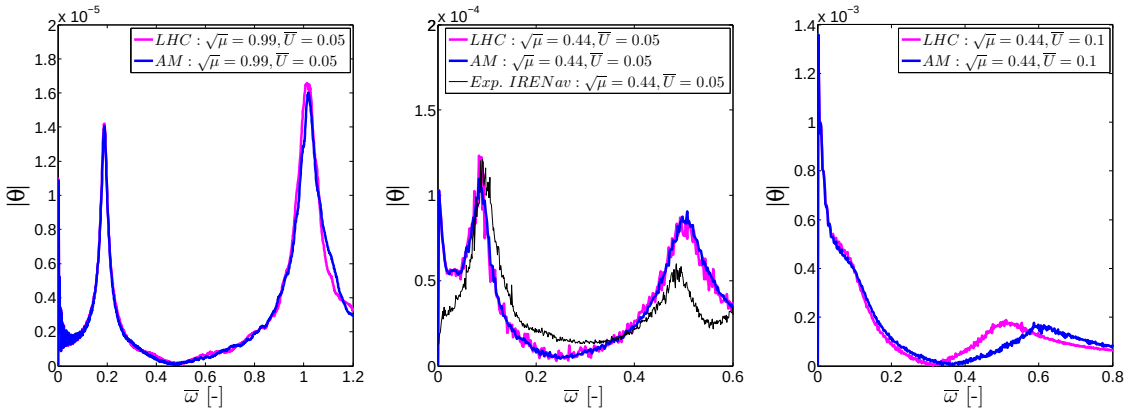

(a) θ at $\sqrt{\mu} = 0.99$ & $\overline{U} = 0.05$ (b) θ at $\sqrt{\mu} = 0.44$ & $\overline{U} = 0.05$ (c) θ at $\sqrt{\mu} = 0.44$ & $\overline{U} = 0.1$

Figure 6.2: Comparison of the frequency spectra ($\overline{\omega} = \omega/\omega_\theta$) of twisting deformations with different viscous FSI methods on the NACA0015 stainless steel and POM hydrofoils at $\alpha_o = 8^o$ with (a) $\sqrt{\mu} = 0.99$ & $\overline{U} = 0.05$, (b) $\sqrt{\mu} = 0.44$ & $\overline{U} = 0.05$, and (c) $\sqrt{\mu} = 0.44$ & $\overline{U} = 0.1$. Note that the FFT window size is $\overline{t} = 0 - 2500$.

Figures 6.1 - 6.2 show the predicted time-histories and frequency spectra, respec-

tively, of twisting deformations for the LHC and AM methods on the NACA0015 stainless steel and POM hydrofoils ($\sqrt{\mu}$=0.44 & 0.99) at $\alpha_o = 8^o$ with $\overline{U}$=0.05 & 0.1. The results show that there are no significant differences between the LHC and AM methods at the low reduced velocity ($\overline{U} = 0.05$) and high mass ratio ($\sqrt{\mu} = 0.99$) as shown in Figs. 6.1 (a), (b) - 6.2 (a), (b). However, for the case with $\sqrt{\mu} = 0.44$ and $\overline{U} = 0.1$ shown in Figs. 6.1 (c) and 6.2 (c), there is a phase shift of the twisting deformations between LHC and AM methods, which lead to slightly high first in-water natural twisting frequency predicted by the AM method than the LHC method. This implies that the fluid damping and fluid disturbing force terms may be important for cases with low μ and high $\overline{U}$ (i.e., $\sqrt{\mu} \leq 0.5$ & $\overline{U} \geq 0.05$) because these are propositional to the $\overline{U}$ and $\overline{U}^2$, respectively, as shown in Eqs. (2.7) and (2.8).

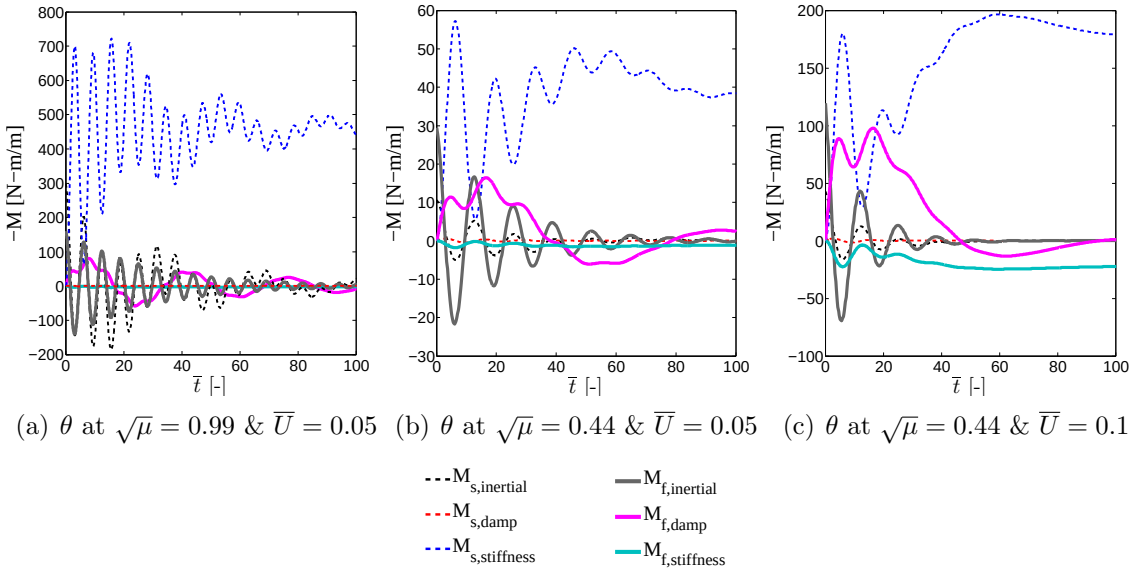

(a) θ at $\sqrt{\mu} = 0.99$ & $\overline{U} = 0.05$ (b) θ at $\sqrt{\mu} = 0.44$ & $\overline{U} = 0.05$ (c) θ at $\sqrt{\mu} = 0.44$ & $\overline{U} = 0.1$

Figure 6.3: Comparison of the time-histories of moment (M) of the inviscid fully coupled (FC) method on the NACA0015 stainless steel and POM hydrofoils at $\alpha_o = 8^o$ with (a) $\sqrt{\mu} = 0.99$ & $\overline{U} = 0.05$, (b) $\sqrt{\mu} = 0.44$ & $\overline{U} = 0.05$ (c) $\sqrt{\mu} = 0.99$ & $\overline{U} = 0.05$, (b) $\sqrt{\mu} = 0.44$ & $\overline{U} = 0.05$, and (c) $\sqrt{\mu} = 0.44$ & $\overline{U} = 0.1$. Note that $\overline{t} = t\omega_\theta$ is the non-dimensional time.

To better understand the influence of the fluid damping and fluid disturbing force terms, Fig. 6.3 shows the time-histories of the dimensional solid and fluid inertial, damping, and stiffness moments obtained via the inviscid fully coupled (FC) method.

The results show that the sold stiffness moment is dominant in general due to the higher torsional spring coefficient, which corresponded to a NACA0015 POM hydrofoil with $c = 0.1\ m$ and $s = 0.192\ m$. Notice that as μ decreases, ω_θ^* decreases so the response period increases. The magnitude of the fluid inertial and damping terms become larger than the solid inertial and damping terms, respectively, when $\sqrt{\mu} < 1$. In addition, the fluid damping terms increase in proportion to $\overline{U}$, and the fluid disturbing terms increase in proportion to $\overline{U}^2$. Hence, as μ decreases and/or $\overline{U}$ increases, the vibration damps out faster, which will make it more difficult to capture the frequency peaks as the system becomes over-damped and non-harmonic, as shown in Fig. 6.1. In particular, for the $\sqrt{\mu} = 0.44$ and $\overline{U} = 0.1$ case, the fluid damping terms become larger than the fluid inertial terms, which lead to differences in solution between the LHC and AM, as shown in Fig. 6.2 (c), as the fluid forces are no longer dominated by the fluid inertial terms. Therefore, additional experimental studies are needed to validate the accuracy of the LHC and AM solutions for such low μ and high $\overline{U}$ case.

In the future, the authors will extend the viscous LHC or AM method to simulate the transient FSI response and stability boundary of 3D flexible hydrofoils and propulsors, as the current CFD model is 2D, and the foil is assumed to be rigid in the chordwise direction. In particular, more studies are needed to investigate 3D effects, dynamics near the foil tip. High fidelity 3D LES or DNS simulations coupled with 3D solid model are also needed to better quantify the dynamic FSI response in flows dominated by transient large-scale vortices. Moreover, the authors will investigate the effects of free surface, cavitation, material anisotropy, and scaling laws on the dynamic viscous FSI response and stability boundary of flexible hydrofoils.

Furthermore, more numerical simulations and experiments with different flexible materials are needed to improve our understanding of flow-induced vibrations and the resulting impact on foil performance and stability. Additional research is also needed

to investigate the susceptibility of flexible hydrofoils to buffeting and galloping.

APPENDICES

APPENDIX A

Non-dimensional Equation

A.1 Inviscid Fully Coupled (FC) Method

The dimensional inviscid FSI coupling model (i.e., fully coupled method) can be written:

$$(\widetilde{\mathbf{M}}_{\mathrm{s}} + \widetilde{\mathbf{M}}^{T})\ddot{\widetilde{\mathbf{X}}}_n + (\widetilde{\mathbf{C}}_{\mathrm{s}} + \widetilde{\mathbf{C}}^{T})\dot{\widetilde{\mathbf{X}}}_n + (\widetilde{\mathbf{K}}_{\mathrm{s}} + \widetilde{\mathbf{K}}^{T})\widetilde{\mathbf{X}}_n = \widetilde{\mathbf{F}}_{\mathrm{static}}, \tag{A.1}$$

where the subscript n is index for the each time-step level and $\widetilde{\mathbf{X}} = [h/b, \theta]^T$, $\dot{\widetilde{\mathbf{X}}}$, and $\ddot{\widetilde{\mathbf{X}}}$ are the dimensional displacement, velocity, and acceleration vectors. $\widetilde{\mathbf{M}}_{\mathrm{s}}$, $\widetilde{\mathbf{C}}_{\mathrm{s}}$, and $\widetilde{\mathbf{K}}_{\mathrm{s}}$ are, respectively, dimensional solid inertial, damping, and stiffness terms, which could be written as:

$$\widetilde{\mathbf{M}}_{\mathrm{s}} = \begin{bmatrix} m & S_\theta \\ S_\theta & I_\theta \end{bmatrix}, \widetilde{\mathbf{C}}_{\mathrm{s}} = \begin{bmatrix} C_{s,h} & 0 \\ 0 & C_{s,\theta} \end{bmatrix}, \widetilde{\mathbf{K}}_{\mathrm{s}} = \begin{bmatrix} K_{s,h} & 0 \\ 0 & K_{s,\theta} \end{bmatrix}, \tag{A.2}$$

where m, $S_\theta (= m x_\theta b)$, and $I_\theta (= m r_\theta^2 b^2)$ are respectively the solid mass per unit span, the static imbalance per unit span, and the solid mass moment of inertia per unit span defined about the elastic axis (EA), while r_θ is the nondimensional radius of gyration.

b is the semi-chord length ($c/2$). If $\omega_h = 2\pi f_h$ and $\omega_\theta = 2\pi f_\theta$ are the first in-air natural bending and twisting frequencies, then $C_{s,h} = 2m\omega_h\zeta_h$ and $C_{s,\theta} = 2I_\theta\omega_\theta\zeta_\theta$ are the solid damping values per unit span for the bending and twisting motions, respectively; ζ_h and ζ_θ are the solid bending and twisting damping coefficients. Similarly, $K_{s,h} = m\omega_h^2$ and $K_{s,\theta} = I_\theta\omega_\theta^2$ are the solid bending and torsional stiffness values per unit span.

$\widetilde{\mathbf{M}}^T$, $\widetilde{\mathbf{C}}^T$ and $\widetilde{\mathbf{K}}^T$ are, respectively, dimensional fluid inertial, damping, and stiffness terms per unit span, which are expressed by *Theodorsen* (1935) approach in terms of inviscid fluid lift and moment acting on the foil and could be written as:

$$\widetilde{\mathbf{M}_\mathrm{f}}^T = \begin{bmatrix} \pi\rho_f b^2 & -\pi\rho_f b^3 a \\ -\pi\rho_f b^3 a & \pi\rho_f b^4(\frac{1}{8} + a^2) \end{bmatrix}, \tag{A.3}$$

$$\widetilde{\mathbf{C}_\mathrm{f}}^T = -\pi\rho_f U b^2 \begin{bmatrix} -\frac{2}{b}C(k) & -(1 + (1-2a)C(k)) \\ (2a+1)C(k) & b(\frac{1}{2} - a)(-1 + (2a+1)C(k)) \end{bmatrix}, \tag{A.4}$$

$$\widetilde{\mathbf{K}_\mathrm{f}}^T = \begin{bmatrix} 0 & 2\pi\rho_f U^2 b C(k) \\ 0 & -\pi\rho_f U^2 b^2 (2a+1)C(k) \end{bmatrix}, \tag{A.5}$$

where U is the inflow velocity, ρ_f is the fluid density. a is non-dimensional distance from mid-chord to EA, positive for EA aft mid-chord. $k = \omega b/U$ is the reduced frequency. $C(k)$ is the Theodorsen's circulation function, which can be considered as a measure to quantify the wake induced loss of the lift, which could be written as Eq. (A.6).

$$C(k) = F(k) + iG(k) = \frac{H_1^2(k)}{H_1^2(k) + iH_0^2(k)}, \tag{A.6}$$

where $H_1^2(k)$ and $H_0^2(k)$ are the Hänkel functions.(i.e., 3^{rd} kind Bessel functions).

$\widetilde{\mathbf{F}}_{\text{static}}$ is the dimensional static force vector as presented in Eq. (A.7)

$$\widetilde{\mathbf{F}}^{T}_{\text{static}} = \begin{bmatrix} 2qb(\alpha_o - \alpha_{Lo})\frac{dC_L}{d\alpha} \\ qc^2 C_{Mo,AC} - 2qb^2 e(\alpha_o - \alpha_{Lo})\frac{dC_L}{d\alpha} \end{bmatrix}, \tag{A.7}$$

where $dC_L/d\alpha = 2\pi$ is the theoretical slope of the lift coefficient vs. angle of attack curve, and $q = \frac{1}{2}\rho_f U^2$ is the dynamic fluid pressure. α_o and α_{Lo} are, respectively, the initial angle of attack and the angle of attack at which the lift force is zero. $C_{Mo,AC}$ is the moment coefficient at the aerodynamic center (AC), which is assumed to be at $c/4$ away from the foil leading edge. $e = a + \frac{1}{2}$ is the non-dimensional distance (as a fraction of b) from the EA to the AC. Note that for a symmetric foil with no camber, α_{Lo} and $C_{Mo,AC}$ are both zero.

The discretized EOM of the inviscid FC method in a time domain (TD) is re-written in Eq.(A.8).

$$\begin{aligned} &\left(\begin{bmatrix} m & S_\theta \\ S_\theta & I_\theta \end{bmatrix} + \begin{bmatrix} \pi\rho_f b^2 & -\pi\rho_f b^3 a \\ -\pi\rho_f b^3 a & \pi\rho_f b^4(\frac{1}{8} + a^2) \end{bmatrix} \right) \begin{bmatrix} \ddot{h} \\ \ddot{\theta} \end{bmatrix} \\ &+ \left(\begin{bmatrix} C_h & 0 \\ 0 & C_\theta \end{bmatrix} - \pi\rho_f U b^2 \begin{bmatrix} -\frac{2}{b}C(k) & -(1 + (1-2a)C(k)) \\ (2a+1)C(k) & b(\frac{1}{2} - a)(-1 + (2a+1)C(k)) \end{bmatrix} \right) \begin{bmatrix} \dot{h} \\ \dot{\theta} \end{bmatrix} \\ &+ \left(\begin{bmatrix} K_h & 0 \\ 0 & K_\theta \end{bmatrix} + \begin{bmatrix} 0 & 2\pi\rho_f U^2 b C(k) \\ 0 & -\pi\rho_f U^2 b^2 (2a+1)C(k) \end{bmatrix} \right) \begin{bmatrix} h \\ \theta \end{bmatrix} \\ &= \begin{bmatrix} 2\pi\rho_f U^2 b(\alpha_o - \alpha_{Lo}) \\ 2\rho_f U^2 b^2 C_{Mo,AC} - 2\pi\rho_f U^2 b^2 e(\alpha_o - \alpha_{Lo}) \end{bmatrix}. \end{aligned} \tag{A.8}$$

The EOM of the inviscid FC method is non-dimensionalized by using b for length, $\pi\rho_f b^2$ for mass per unit span, $1/\omega_\theta$ for time, and $\pi\rho_f b^3\omega_\theta^2$ and $\pi\rho_f b^4\omega_\theta^2$ for static lift and moment per unit span, respectively. Therefore, the non-dimensional inviscid FC method in a time domain can be expressed in Eq.(A.9).

$$\left(\mu\begin{bmatrix}1 & x_\theta\\ x_\theta & r_\theta^2\end{bmatrix}+\begin{bmatrix}1 & -a\\ -a & \frac{1}{8}+a^2\end{bmatrix}\right)\begin{bmatrix}\frac{\ddot{h}}{b}\\ \ddot{\theta}\end{bmatrix} \tag{A.9}$$

$$+\left(\mu\begin{bmatrix}2\Omega\zeta_{s,h} & 0\\ 0 & 2r_\theta^2\zeta_{s,\theta}\end{bmatrix}+\overline{U}\begin{bmatrix}2C(k) & 1+C(k)(1-2a)\\ -C(k)(2a+1) & \left(\frac{1}{2}-a\right)[1-C(k)(2a+1)]\end{bmatrix}\right)\begin{bmatrix}\frac{\dot{h}}{b}\\ \dot{\theta}\end{bmatrix}$$

$$+\left(\mu\begin{bmatrix}\Omega^2 & 0\\ 0 & r_\theta^2\end{bmatrix}+\overline{U}^2\begin{bmatrix}0 & 2C(k)\\ 0 & -C(k)(2a+1)\end{bmatrix}\right)\begin{bmatrix}\frac{h}{b}\\ \theta\end{bmatrix}$$

$$=\overline{U}^2\begin{bmatrix}2(\alpha_o-\alpha_{Lo})\\ 2C_{Mo,AC}/\pi-2e(\alpha_o-\alpha_{Lo})\end{bmatrix}.$$

The discretized non-dimensional inviscid solver of the fully coupled equation of motion (EOM) is shown below:

$$(\mathbf{M}_\mathrm{s}+\mathbf{M}^T)\ddot{\mathbf{X}}_n+(\mathbf{C}_\mathrm{s}+\mathbf{C}^T)\dot{\mathbf{X}}_n+(\mathbf{K}_\mathrm{s}+\mathbf{K}^T)\mathbf{X}_n=\mathbf{F}_\mathrm{static}. \tag{A.10}$$

In Eq. (A.10), $\mathbf{X}=[h/b,\theta]^T$, $\dot{\mathbf{X}}$, and $\ddot{\mathbf{X}}$ are the non-dimensional displacement, velocity, and acceleration vectors. $\mathbf{M}_\mathrm{s}$, $\mathbf{C}_\mathrm{s}$, and $\mathbf{K}_\mathrm{s}$ are, respectively, the non-dimensional solid inertial, damping, and stiffness matrices $\mathbf{M}^T$, $\mathbf{C}^T$, and $\mathbf{K}^T$ are, respectively, the non-dimensional inviscid fluid inertial, damping, and stiffness matrices. $\mathbf{F}_\mathrm{static}$ is the non-dimensional static force vector.

A.2 Viscous Loose Hybrid Coupled (LHC) Method

The dimensional viscous FSI coupling model (i.e., Loose hybrid coupled method (*Young et al.*, 2012; *Chae et al.*, 2013)) is solved using a semi-implicit Crank-Nicholson

method in order to maintain the second-order accuracy in time, which can be written:

$$(\widetilde{\mathbf{M}}_{\mathrm{s}} + \widetilde{\mathbf{M}}^{T})\ddot{\widetilde{\mathbf{X}}}_{n+1} + (\widetilde{\mathbf{C}}_{\mathrm{s}} + \widetilde{\mathbf{C}}^{T})\dot{\widetilde{\mathbf{X}}}_{n+1} + (\widetilde{\mathbf{K}}_{\mathrm{s}} + \widetilde{\mathbf{K}}^{T})\widetilde{\mathbf{X}}_{n+1} = (\widetilde{\mathbf{F}}_{\mathrm{CFD}})_{n} - (\widetilde{\mathbf{F}}^{T}_{\mathrm{FSI}})_{n}, \tag{A.11}$$

where the dimensional inviscid fluid force vector, $\widetilde{\mathbf{F}}^{T}_{\mathrm{FSI}}$ as presented in Eq. (A.12), is expressed by *Theodorsen* (1935) approach.

$$\widetilde{\mathbf{F}}^{T}_{\mathrm{FSI}} = -\widetilde{\mathbf{M}}^{T}\ddot{\widetilde{\mathbf{X}}} - \widetilde{\mathbf{C}}^{T}\dot{\widetilde{\mathbf{X}}} - \widetilde{\mathbf{K}}^{T}\widetilde{\mathbf{X}}. \tag{A.12}$$

The dimensional viscous fluid force vector for the lift and moment acting on the hydrofoil, $\widetilde{\mathbf{F}}_{\mathrm{CFD}}$ from *ANSYS-CFX* (2011), is computed as follows in Eq. (A.13).

$$\widetilde{\mathbf{F}}_{\mathrm{CFD}} = \begin{bmatrix} \oint_{A}(\mathbf{j}\cdot\boldsymbol{\sigma}_{f}\mathbf{n})\mathrm{d}A \\ \\ \oint_{A}(\mathbf{r}\times\boldsymbol{\sigma}_{f}\mathbf{n})\mathrm{d}A \end{bmatrix}, \tag{A.13}$$

where $\mathbf{n}$ is a unit normal vector on the foil surface, $\mathbf{j}$ is a unit vector along the Y direction, and $\mathbf{r}$ is a vector from the EA to a point on the closed foil surface (A). $\boldsymbol{\sigma}_{f}$ is the total stress tensor for a Newtonian fluid for a Newtonian fluid as shown in Eq. (A.14).

$$\boldsymbol{\sigma}_{f} = -P\mathbf{I} + \mu_{\mathrm{eff}}(\nabla\mathbf{u}_{f} + \nabla\mathbf{u}_{f}^{T}), \tag{A.14}$$

where $\mathbf{I}$ is the identity matrix, P is the total pressure, and $\mathbf{u}_{f}$ is the local fluid velocity. μ_{eff} is the fluid effective dynamic viscosity.

Similar to the inviscid FC method, the EOM of the viscous LHC method is non-dimensionalized by using b for length, $\pi\rho_{f}b^{2}$ for mass per unit span, and $1/\omega_{\theta}$ for time, P_{o} (the static pressure) for reference pressure, and $\omega_{\theta}b$ for velocity. Therefore, the discretized EOM of the non-dimensional viscous LHC method in a time domain

is given in Eq.(A.15).

$$(\mathbf{M}_{\mathrm{s}} + \mathbf{M}^T)\ddot{\mathbf{X}}_{n+1} + (\mathbf{C}_{\mathrm{s}} + \mathbf{C}^T)\dot{\mathbf{X}}_{n+1} + (\mathbf{K}_{\mathrm{s}} + \mathbf{K}^T)\mathbf{X}_{n+1} = (\mathbf{F}_{\mathrm{CFD}})_n - (\mathbf{F}^T_{\mathrm{FSI}})_n. \quad \text{(A.15)}$$

In Eq. (A.15), $\mathbf{F}_{\mathrm{CFD}}$ is the non-dimensional viscous fluid lift and moment acting on the hydrofoil as shown in Eq. (A.16).

$$\mathbf{F}_{\mathrm{CFD}} = \begin{bmatrix} \oint_A (\mathbf{j} \cdot \overline{\boldsymbol{\sigma}}_f \mathbf{n}) \mathrm{d}A \\ \\ \oint_A (\mathbf{r} \times \overline{\boldsymbol{\sigma}}_f \mathbf{n}) \mathrm{d}A \end{bmatrix}, \quad \text{(A.16)}$$

$$\overline{\boldsymbol{\sigma}}_f = -\frac{Eu}{2}\overline{P}\mathbf{I} + \frac{2}{Re_{\mathrm{eff}}\overline{U}}(\overline{\nabla}\overline{\mathbf{u}}_f + \overline{\nabla}\overline{\mathbf{u}}_f^T), \quad \text{(A.17)}$$

where $\overline{\boldsymbol{\sigma}}_f$ is the non-dimensional total stress tensor for a Newtonian fluid, $\overline{P}$ is the non-dimensional total pressure, $\overline{\mathbf{u}}_f$ is the non-dimensional local fluid velocity, $\overline{U}$ is the reduced velocity, $Eu = \frac{2P_o}{\rho_f U^2}$ is the Euler number, and $Re_{\mathrm{eff}} = \frac{Uc}{\nu_{\mathrm{eff}}}$ is the effective Reynolds number. ν_{eff} is the fluid effective kinematic viscosity.

BIBLIOGRAPHY

BIBLIOGRAPHY

Abramson, H. N., and G. E. Ransleben (1965), An experimental investigation of flutter of a fully submerged subcavitating hydrofoil, *Journal of Aircraft*, *2(5)*, 439–442.

Akcabay, D. T., and Y. L. Young (2012), Hydroelastic response and energy harvesting potential and flexible piezoelectric beams in viscous flow, *Physics of Fluids*, *24(5)*, 054,106.

Akcabay, D. T., and Y. L. Young (2014), Cavity-induced vibration of flexible hydrofoils and their susceptibility to lock-in and parametric excitations, *2014 Symposium on Naval Hydrodynamics, Hobart, Tasmania, Australia, 2-7 November*.

Akcabay, D. T., E. J. Chae, Y. L. Young, A. Ducoin, and A. Astolfi (2014), Cavity induced vibration of flexible hydrofoils, *Journal of Fluids and Structures*, *49*, 463–484.

Akcabay, D. T., J. Xiao, and Y. L. Young (2015), Numerical stabilities of loosely coupled method for robust modeling of lightweight and flexible structures in dense incompressible and viscous flows, *in preparation for Journal of Computational Physics*.

Anderson, J. M., K. Streitlien, D. S.Barrett, and M. S. Triantafyllou (1998), Oscillating foils of high propulsive efficiency, *Journal of Fluid Mechanics*, *360*, 41–72.

ANSYS-CFX (2011), *User's guide 14.0.*, ANSYS, Inc.

Ausoni, P. (2009), Turbulent vortex shedding from a blunt trailing edge hydrofoil, Phd thesis, Ecole Polytechnique fédérale de Lausanne.

Ausoni, P., M. Farhat, X. Escaler, E. Egusquiza, and F. Avellan (2007), Cavitation influence on von karman vortex shedding and induced hydrofoil vibrations, *Journal of Fluids Engineering*, *129*, 966–973.

Bachynski, E. E., Y. L. Young, and R. W. Yeung (2012), Analysis and optimization of tethered wave energy converter in irregular waves, *Renewable Energy*, *48*, 133–145.

Belanger, F., M. P. Paidoussis, and E. de. Langre (1995), Time-marching analysis of fluid-coupled systems with large added mass, *AIAA Journal*, *33*, 752–757.

Bendiksen, O. O. (1992), Role of shock dynamics in transonic flutter, *AIAA paper*, *2121*, 401–414.

Bendiksen, O. O. (2002), Multibranch and period tripling flutter, *in Proceedings of IMECE2002 ASME International Mechanical Engineering Congress and Exposition, New Orleans, Louisiana, USA*, *33050*.

Bernitsas, M. M., K. Raghavan, Y. Ben-Simon, and E. M. H. Garcia (2008), Vivace(vortex induced vibration aquatic clean energy): a new concept in generation of clean and renewable energy from fluid flow, *Journal of Offshore Mechanics and Arctic Engineering*, *130(4)*, 041,101–1 – 041,101–15.

Besch, P. K., and Y. Liu (1971), Flutter and divergence characteristics of four low mass ratio hydrofoils, *Tech. Rep. 3410*, Naval Ship Research and Development Center.

Blake, W., L. J. . Maga, and G. Finkelstein (1977), Hydroelastic variables influencing propeller and hydrofoil singing, *Nose and Fluid Engineering*, *1*, 191–199.

Blake, W. K., and L. J. Maga (1975), On the flow-excited vibrations of cantilever struts in water. i. flow-induced damping and vibration, *Journal of the Acoustical Society of America*, *57(3)*, 610–625.

Brennen, C., K. T. Oey, and C. D. Badcock (1980), Leading-edge flutter of supercavitating hydrofoils, *Journal of Ship Research*, *24(3)*, 135–146.

Caporali, R. L., and E. J. Brunelle (1964), Hydrofoil instability at low mass density ratios, *Tech. rep.*, Aerospace and Mechanical Sciences Report 670.

Causin, P., J. F. Gerbeau, and F. Nobile (2005), Added-mass effect in the design of partitioned algorithms for fluid-structure problems, *Computational Methods in Applied Mechanical Engineering*, *194(42–44)*, 4506–4527.

Chae, E. J., D. T. Akcabay, and Y. L. Young (2013), Dynamic response and stability of a flapping foil in a dense viscous fluid, *Physics of Fluids*, *25*, 104–106.

Chae, E. J., D. T. Akcabay, A. Lelong, J. Astolfi, and Y. L. Young (2015a), Numerical and experimental studies on flow-induced vibrations of flexible hydrofoils, *in preparation for Journal of Fluid and Structure*.

Chae, E. J., D. T. Akcabay, and Y. L. Young (2015b), Influence of flow-induced bend-twist coupling on the dynamic response, wake structure, and stability of flexible hydrofoils, *in preparation for Journal of Fluid and Structure*.

Chen, S., and M. W. Wambsganss (1972), Parallel flow induced vibration of fuel rods, *Nuclear Engineering and Design*, *18(2)*, 253–278.

Cieslowski, D. S., and P. K. Besch (1970), Flutter of a two degree of freedom hydrofoil in two dimensional subcavitating flow, *Tech. Rep. 3183*, Naval Ship Research and Development Center.

Connell, B. S. H., and D. K. P. Yue (2007), Flapping dynamics of a flag in a uniform stream, *Journal of Fluid Mechanics*, *581*, 33–67.

Cremer, L., M. Heckl, and B. Petersson (2005), *Structure-Borne Sound: Structural Vibrations and Sound Radiation at Audio Frequencies*, Springer.

de Langre, E. (2006), Frequency lock-in is caused by coupled-mode flutter, *Journal of Fluids and Structures*, *22*, 783–791.

Ducoin, A., and Y. L. Young (2013), Hydroelastic response and stability of a hydrofoil in viscous flow, *Journal of Fluids and Structures*, *38*, 40–57.

Forster, C., W. A. Wall, and E. Ramm (2007), Artificial added mass instabilities in sequential staggered coupling of nonlinear structures and incompressible viscous flows, *Computational Methods in Applied Mechanical Engineering*, *196(7)*, 1278–1293.

Garrick, I. E. (1946), Bending-torsion flutter calculations modified by subsonic compressibility corrections, *Tech. Rep. 836*, National Advisory Committee for Aeronautics.

Huang, R. F., and C. L. Lin (1995), Vortex shedding and shear-layer instability of wing at low-reynolds numbers, *AIAA Journal*, *3(8)*, 1398–1403.

Jacobs, E., and A. Sherman (1937), Airfoil section characteristics as affected by variations of the reynolds number, *Tech. Rep. 586*, National Advisory Committee for Aeronautics.

Jung, Y. W., and S. O. Park (2005), Vortex-shedding characteristics in the wake of an oscillating airfoil at low reynolds number, *Journal of Fluid and Structures*, *20*, 451–464.

Klamo, J. T. (2007), Effect of damping and reynolds number on vortex-induced vibrations, Phd thesis, California Institute of Technology.

Kousen, K. A., and O. O. Bendiksen (1988), Nonlinear aspects of the transonic aeroelastic stability problem, *AIAA paper*, *88-2306*, 760–769.

Leibowitz, R. C., and D. J. Belz (1962), Comparison of theory and experiment for marine control-surface flutter, *Tech. rep.*, Department of the Navy David Tayler Model Basin.

Leissa, A. W. (1969), Vibration of plates, *Tech. rep.*, NASA Sp-160.

Lian, Y., and W. Shyy (2007), Laminar-turbulent transition of a low reynolds number rigid or flexible airfoil, *AIAA Journal*, *45(7)*, 1501–1513.

Lindholm, U. S., D. D. Kana, W. H. Chu, and H. N. Abramson (1965), Elastic vibration characteristics of cantilever plates in water, *Journal of Ship Research*, *9*, 11–22.

McCormick, M. E., and L. Caracoglia (2004), Hydroelastic instability of low aspect ratio control surfaces, *Journal of Offshore Mechanics and Arctic Engineering*, *126(1)*, 84–89.

Mok, D., and W. Wall (2001), Partitioned analysis schemes for the transient interaction of incompressible flows and nonlinear flexible structures, *Trends in Computational Structural Mechanics*, *49*, 689–698.

Motley, M., and Y. L. Young (2011), Performance-based design and analysis of flexible composite propulsors, *Journal of Fluid and Structures*, *27(8)*, 1310–1325.

Munch, C., P. Ausoni, and O. Braun (2010), Fluid-structure coupling for an oscillating hydrofoil, *Journal of Fluids and Structures*, *26*, 1018–1033.

Olofsson, N. (1966), Force and flow characteristics of a partially submerged propeller, Phd thesis, Chalmers University of Technology.

Paidoussis, M. P. (1973), Dynamics of cylindrical structures subjected to axial flow, *Journal of Sound and Vibration*, *29(3)*, 365–385.

Poirel, D., and W. Yuan (2010), Aerodynamics of laminar separation flutter at a transitional reynolds number, *Journal of Fluids and Structures*, *26(7–8)*, 1174–1194.

Poirel, D., Y. Harris, and A. Benaissa (2008), Self-sustained aeroelastic oscillations of a naca0012 airfoil at low-to-moderate reynolds numbers, *Journal of Fluids and Structures*, *24(5)*, 700–719.

Reese, M. C. (2010), Vibration and damping of hydrofoils in uniform flow, Phd thesis, Pennsylvania State University.

Schnipper, T., A. Andersen, and T. Bohr (2009), Vortex wakes of a flapping foil, *Journal of Fluid Mechanics*, *633*, 411–423.

Sears, W. R. (1941), Some aspects of non-stationary airfoil theory and its practical application, *Journal of the Aeronautical Sciences(Institute of the Aeronautical Sciences)*, *8(3)*, 104–108.

Song, C. S. (1972), Flutter of supercavitating hydrofoils - comparisons of theory and experiment, *Journal of Ship Research*, *16(3)*, 153–166.

Tang, L., M. P. Paidoussis, and J. Jiang (2009), Cantilevered flexible plates in axial flow: Energy transfer and the concept of flutter-mill, *Journal of Sound and Vibration*, *326(1-2)*, 263–276.

Theodorsen, T. (1935), General theory of aerodynamic instability and the mechanism of flutter, *Tech. Rep. 496*, National Advisory Committee for Aeronautics.

Visbal, M. R., R. E. Gordnier, and M. C. Galbraith (2009), High-fidelity simulations of moving and flexible airfoils at low reynolds numbers, *Experiments in Fluids*, *46(5)*, 903–922.

Weissinger, J. (1947), The lift distribution of swept-back wings, *Tech. Rep. 1120*, National Advisory Committee for Aeronautics.

Williamson, C. H. K., and A. Roshko (1988), Vortex formation in the wake of an oscillating cyliner, *Journal of Fluids and Structures*, *2*, 355–381.

Woolston, D. S., and G. E. Castile (1951), Some effects of variations in several parameters including fluid density on the flutter speed of light uniform cantilever wings, *Tech. Rep. 2558*, National Advisory Committee for Aeronautics.

Xiao, J., and R. C. Batra (2012), Local water slamming of curved rigid hulls, *The International Journal of Multiphysics*, *6(3)*, 305–339.

Young, Y. L. (2007), Time-dependent hydroelastic analysis of cavitating propulsors, *Journal of Fluids and Structures*, *23(2)*, 269–295.

Young, Y. L. (2008), Fluid-structure interaction analysis of flexible composite marine propellers, *Journal of Fluids and Structures*, *24(6)*, 799–818.

Young, Y. L., and B. R. Savander (2011), Numerical analysis of large-scale surface-piercing propellers, *Ocean Engineering*, *38(13)*, 1368–1381.

Young, Y. L., E. J. Chae, and D. T. Akcabay (2012), Hybrid algorithm for modeling of fluid-structure interaction in incompressible, viscous flows, *Acta Mech. Sin*, *28(4)*, 1030–1041.